2012

Simulations of a miniaturized scanning electron microscope

Stephanie Karen Medley

SIMULATIONS OF A MINIATURIZED SCANNING ELECTRON MICROSCOPE

by

Stephanie Karen Medley

A THESIS

Submitted in partial fulfillment of the requirements
for the degree of Master of Science
in
The Department of Physics
to
The School of Graduate Studies
of
The University of Alabama in Huntsville

Huntsville, Alabama

2012

In presenting this thesis in partial fulfillment of the requirements for a master's degree from The University of Alabama in Huntsville, I agree that the Library of this University shall make it freely available for inspection. I further agree that permission for extensive copying for scholarly purposes may be granted by my advisor or, in his/her absence, by the Chair of the Department or the Dean of the School of Graduate Studies. It is also understood that due recognition shall be given to me and to The University of Alabama in Huntsville in any scholarly use which may be made of any material in this thesis.

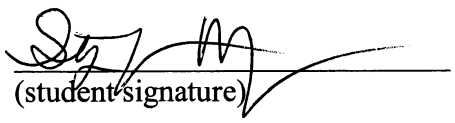

(student signature)

3/29/12

(date)

THESIS APPROVAL FORM

Submitted by Stephanie Medley in partial fulfillment of the requirements for the degree of Master of Science in Physics and accepted on behalf of the Faculty of the School of Graduate Studies by the thesis committee.

We, the undersigned members of the Graduate Faculty of The University of Alabama in Huntsville, certify that we have advised and/or supervised the candidate on the work described in this thesis. We further certify that we have reviewed the thesis manuscript and approve it in partial fulfillment of the requirements for the degree of Master of Science in Physics.

Committee Chair

(Date)

Department Chair

College Dean

Graduate Dean

ABSTRACT
The School of Graduate Studies
The University of Alabama in Huntsville

Degree: Master of Science College/Dept. Science/Physics
Name of Candidate: Stephanie Medley
Title: Simulations of a Miniaturized Scanning Electron Microscope

This research was in support of the development of a miniaturized scanning electron microscope (mini-SEM). Commercially available electron microscopes are large which requires scientist to transport materials for investigation back to the lab. The objective of this investigation was to determine the conditions for optimal performance of the mini-SEM; therefore, the significant results were those related to the current and resolution of the resulting electron beam at the sample plane. The current incident on the sample plane depends on the amount of current produced by the electron gun and then transmitted through various apertures in the electron focusing column of the mini-SEM. Two electron gum types and the electron focusing column were simulated and comparisons were made to experimental results to provide optimized working conditions.

Abstract Approval: Committee Chair Don A. Gregory 3/13/12
Department Chair
Graduate Dean Rhonda Kay Hoede 3/28/12

ACKNOWLEDGMENTS

The work described in this thesis would not have been possible without the assistance of a number of people who deserve special mention: Dr. Don A. Gregory, Dr. Jessica Gaskin and Dr. Lingze Duan for all their advice and support, NASA Marshal Space Flight Center for the financial support and use of their equipment and my family, for all their love and support.

TABLE OF CONTENTS

Page

LIST OF FIGURES

LIST OF TABLES

LIST OF SYMBOLS

α	Emission angle for an axial object point
a	Acceptable focus disk diameter
A	Richardson's constant
B	Magnetic field
C_C	Chromatic aberration coefficient
CD	Cathode tip Diameter
C_S	Spherical aberration coefficient
ΔE	Energy spread of electron
ΔV	Extraction voltage
ΔV_w	Voltage difference between the Wehnelt cylinder and the cathode (Bias Voltage)
d	Distance between extractor (or Wehnelt cylinder) and the cathode
D	Distance between extractor (or Wehnelt cylinder) and the grounded anode
DA	Aperture diameter of the grounded anode
d_c	Spot size as a result of the chromatic aberration
DF	Depth of focus
d_g	Spot size as a result of the geometry of the electron gun,
d_p	Probe size, resulting from all variables
d_s	Spot size as a result of the spherical aberration
d_T	Diameter of the tip of the cathode in the electron gun
d_{VS}	Virtual source broadening
e	Charge on the electron
E	Electric field at the emission region

E_0	Initial energy, energy of emitted electrons
ED	Emission region diameter
φ	Protrusion on the surface of the cathode orientation angle
F	Force on the electron from the electric field
I_a	Simulated current through the grounded anode
I_c	Simulated emission current
I em	Emission current
I_f	Current at the focal plane
I fc	Current detected in the Faraday Cup
I fil	Filament current
k	Boltzman's constant
M	Linear magnification
MV_f	Focusing voltage modulation
PD	Diameter of base of protrusion
PH	Height of protrusion
R	Resistance of resistor in the circuit with the cathode and Wehnelt cylinder
θ	Divergence angle
T	Temperature of the cathode
v	velocity of the electron
V_{acc}	Accelerating voltage
V_f	Focusing voltage
V_w	Voltage on the Wehnelt cylinder
W	Working function of the material of the cathode
WD	Working distance

CHAPTER I

INTRODUCTION

This research defines, through simulation and testing, the optimal operating parameters for the miniaturized scanning electron microscope (mini-SEM) being developed at NASA Marshall Space Flight Center (MSFC) [1, 2]. Specifically, this investigation focused on the electron gun and focusing column performance of the mini-SEM as predicted by the simulations. The most significant parameters, and the core of this thesis, are the electron beam current at the sample (sample current) and the imaging resolution (mainly determined by the size of the electron beam incident on the sample).

The resolution of light microscopes is limited by the wavelength of the light used to measure the sample. Since electrons produced by electron guns have much shorter wavelengths, electron microscopes can achieve a much higher resolution (10 nm is typical for an SEM) [4, 5]. Because of this fine resolution and the SEM's ability to provide chemical information, they are mainstay instruments for many laboratories, from archeology to botany to geology [1, 2].

The MSFC mini-SEM will be used to make in-situ measurements on the Moon (and other airless planetary bodies) [1, 2] and therefore, must be small, compact and lightweight and low power without compromising performance. In-situ operation on the

Moon and at other remote locations will allow for real-time examination of samples. Currently, the size and power requirements of commercial SEMs require samples to be collected and returned to the lab for analysis. The mini-SEM under investigation will offer a much wider range of use by allowing the SEM to be operated *in situ*, thus greatly reducing the need to transport samples to the lab.

1.1 SEM Operation

The primary components of a Scanning Electron Microscope are the electron gun, the electron column and the scanning system (Figure 1.1). The electron gun produces electrons at a given accelerating voltage (10 kV maximum for the mini-SEM) which are focused by the electron focusing column to a spot on the surface of the sample. The interaction between this beam of electrons and the sample results in the emission of secondary electrons, backscatter electrons and X-rays (among other emission types). The scanning system rasters this spot across the surface of the sample and an imaging system combines the electron signal received at each point into an image [3, 4, 5]. Similarly, a compositional map can be generated by compiling the X-ray signal at each of these points [3].

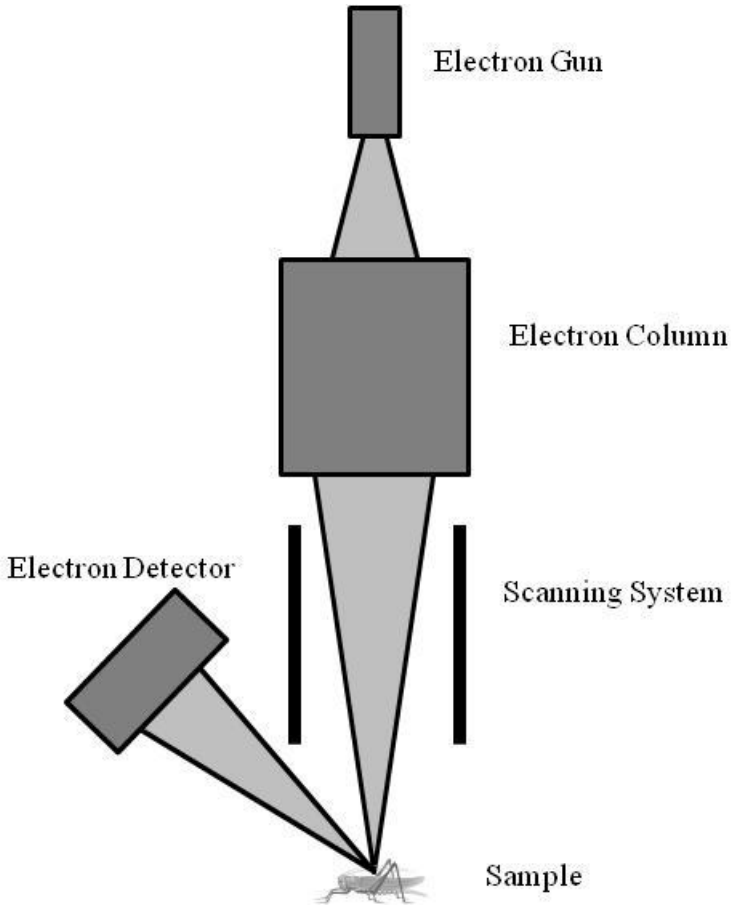

Figure 1.1 Scanning electron microscope

As the electron beam is scanned across a sample, a negative charge is deposited on the surface. For conductive samples, this charge dissipates through its contact to the grounded sample chamber and is not a concern. Non-conductive samples must be coated with a conductive material, such as gold, to allow the charge to be dissipated or a variable pressure SEM must be used.

Brightness, visibility, resolution, magnification, depth of focus, working distance, noise, and composition determine the quality of the image achievable by the electron microscope [3, 4]. These factors depend on the accelerating voltage, the focusing voltage, the type and amount of emission, and the size and shape of the emitter. For instance, the

minimum electron current incident on the sample needed for best image quality and visibility is 1 pA for a 10 nm diameter spot [3].

1.2 Electron Gun Type

Two basic types of electron guns were studied: the cold field emission electron gun (CFEG), which requires operation in ultra-high vacuum, such as on the Moon and a thermionic emission electron gun (TEG) which requires a high-vacuum for operation (Table 1.1). A CFEG utilizes a large potential difference to stimulate emission while a TEG utilizes heat to excite the electrons for emission [3, 4, 5].

The two electron guns have significantly different properties (Table 1.1). The mini-SEM is designed for minimal demagnification, and therefore was designed for use with a CFEG. However, the TEG is attractive, despite its larger virtual source size, in that it is highly robust (can operate under less stringent vacuum conditions), is comparatively inexpensive, and can be operated with readily available, off-the-shelf power supplies and control system. Further, the TEG that was chosen for testing the mini-SEM column was a pointed filament (PF) TEG [6]. A PF-TEG has a much smaller virtual source size than a traditional hairpin filament (PF-TEG filament is 1000 Å in diameter), though still much larger than that of a Cold Field Emitter [6]. The TEG was an inexpensive means to independently test the mini-SEM electron focusing column and scanning system. In both the CFEG and TEG, tungsten was the primary emitter.

Table 1.1 Comparison between cold field emission and thermionic emission [3, 4]

	Thermionic emission	Cold field emission
Temperature (K)	2800	300
Brightness (A/cm^2sr)	10^6	10^9
Operating vacuum (Torr)	10^{-7}	10^{-10}
Virtual source diameter (nm)	$>10^4$	3-5nm
Lifetime (h)	40-100	>1000
Energy dispersion (eV)	1-3	0.3

The CFEG is made up of a cathode, an extractor and a grounded anode. The potential difference between the cathode and the extractor (the extraction voltage) allows the electrons to overcome the work function of the single crystal tungsten and tunnel out. The difference in potential between the cathode and the anode defines the accelerating voltage [3, 4, 5].

The TEG consists of a cathode, a Wehnelt cylinder and a grounded anode [3, 4, 5]. In this case, a high current is applied to the filament. This current heats the emitter producing free electrons which are accelerated towards the grounded anode. The Wehnelt Cylinder suppresses or allows the flow of electrons via an applied bias.

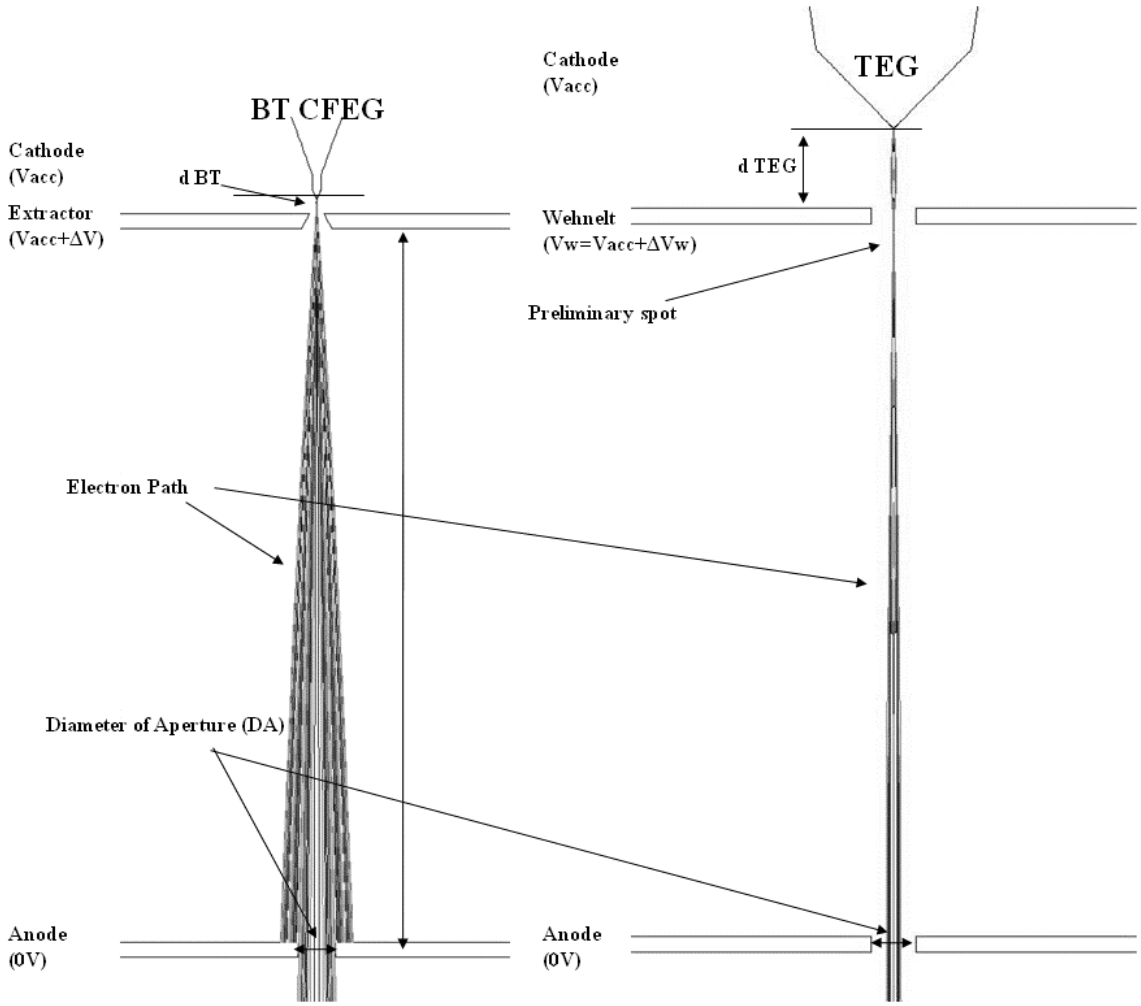

Figure 1.2 Comparison between a cold field emission gun (CFEG) and a thermionic electron gun (TEG) [7]. The electron beam in the TEG has a much tighter beam than the CFEG. The electron paths, also, represent multiple electrons.

Three different methods were used to determine the emission current, and to increase the understanding of how changes in the gun's configuration affect the current produced. These three methods included 1) an investigation of the theory of electron emission and 2) creation and analysis of a simulation to form a better understanding of the variables that affect the current and produce aberrations and 3) the formation and experimental testing of a prototype. These tests increased the understanding of the variables that affect the current and the configuration of the prototype and will help to

make informed changes to the next generation. A focus of this thesis is on simulations done using the commercially available software CPO2DS (sold by Charged Particle Optics Ltd.) and the results of these simulations [7].

1.3 Electron Focusing Column

The purpose of the electron focusing column is to limit and focus the electron beam in order to achieve high resolution without reducing the current at the sample to a level that is lower than the minimum required for imaging [3, 4]. To accomplish this, the electron focusing column consists of apertures of varying sizes and lenses. A block diagram of a standard electron column is given in Figure 1.3 [8]. Following a new design to achieve the small size and high resolution that the mini-SEM requires, the electron focusing column used in this investigation is proprietary.

The simulations of the electron focusing column were used to characterize the resolution and current at the sample plane produced by the mini-SEM. The simulations were also used to evaluate possible improvements that could be made to the design of the electron focusing column.

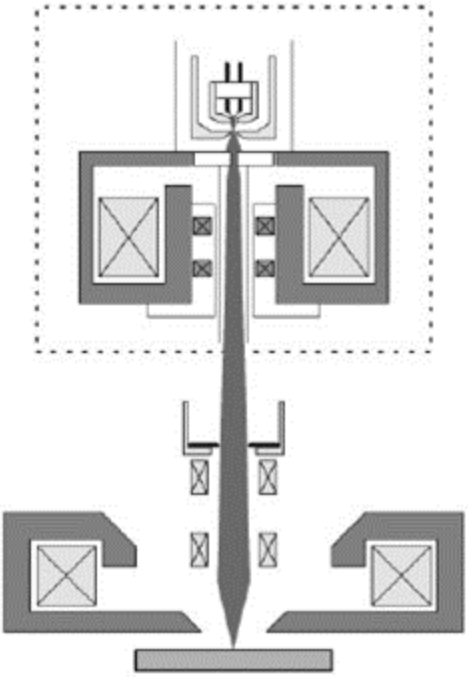

Figure 1.3 Electron focusing column with electron gun [8]

1.4 Simulation Software

"Charged Particle Optics in Two Dimensions with Sources" (CPO2DS) is the commercially available charged particle optics simulation software used in this investigation [6].

The boundary element method (BEM) used by CPO2DS to determine the electric field or potential at a particular location is more accurate than the more commonly used finite difference method which determines the electric potential on a user defined grid [5,6]. BEM discretizes the boundary into boundary elements, then calculates the electric potential, Φ_i, at a particular location based on the element's surface charge, $\widetilde{\sigma_k}$ (Equation (1.1)) [5].

$$\sum_{k=1}^{N} H_{ik}\widetilde{\sigma_k} = \Phi_i \qquad \text{Equation (1.1)}$$

where $\widetilde{\sigma_k} = \sigma(\overline{s_k})$ is the surface charge of the single boundary element evaluated at the center of the element, $\Phi_i = \Phi(\overline{s_i})$ is the electric potential at a given location, $\overline{s_i}$ and $\overline{s_k}$ are the midpoints of the element and H_{ik} is a function of the elliptical integral of the first kind. (A derivation of this equation can be found in Hawkes and Kasper [5].)

The electric potential at the location of an emitted electron is calculated as a sum of the electric potentials from each of the boundary elements [5, 6]. The electron is then stepped forward (the increment of the step is set by the user) in the system based on the energy of the electron and the potential just calculated. At the new location, the electric potential is calculated again and the electron stepped forward. This is continued until the electron has passed through the system.

CHAPTER II

ELECTRON GUN TYPES: THEORY & OPERATION

2.1. Cold Field Emission Gun

The electron gun to be used with the lunar mini-SEM is the cold field emission gun (CFEG). This gun will be used in a Butler-like triode configuration consisting of a tungsten cathode, extractor and grounded anode [1] (Figure 2.1). A large potential difference applied between the cathode and the extractor (sometimes referred to as the first anode) causes electrons to overcome the work function of the cathode's material and tunnel through to the surface (Figure 2.2). This potential (typical values between 3 and 5 kV) is called the extraction voltage (ΔV) [2]. These electrons are then accelerated forward to the grounded anode (otherwise known as the second anode) [2, 3, 4]. The maximum accelerating voltage (the voltage difference between the cathode and the anode) for the lunar mini-SEM CFEG is 10 kV.

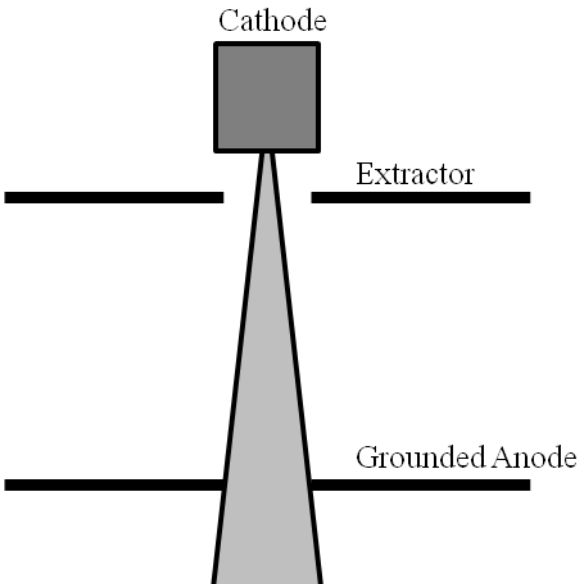

Figure 2.1 Sketch of a cold field emission gun

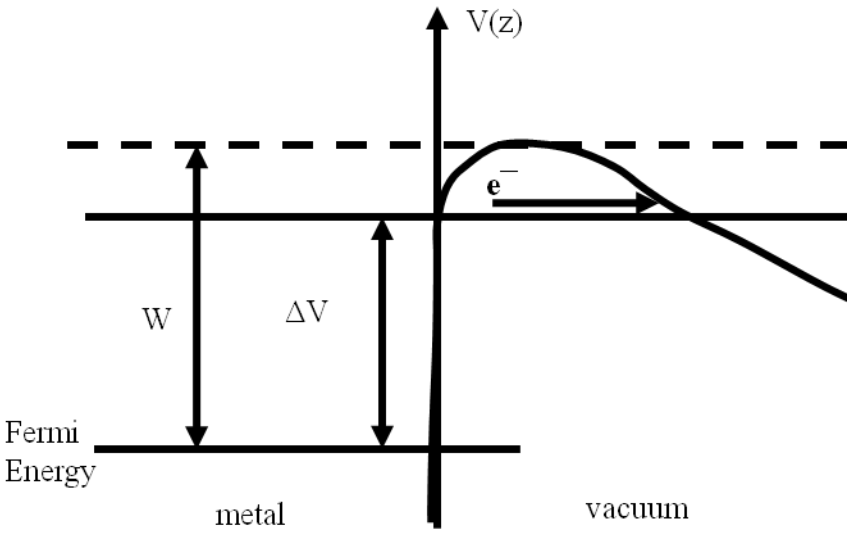

Figure 2.2 Electric potential, V(z), near the cathode surface for cold field emission. The slight slope along the electric potential is a result of the weak electric field. The work function, W, is the barrier to the emission. The potential difference (or extraction voltage), ΔV, is used to stimulate tunneling by increasing the energy of the electron (figure modified from Hawkes and Kasper (1989) [4]).

Cold field emission is modeled using the Fowler-Nordheim equation as follows [2, 3, 4, 5, 6, 7]:

$$\mathbf{j} = \frac{\mathbf{4\pi m e}}{\mathbf{h^3}} \frac{\mathbf{E^2}}{\mathbf{W}} \mathbf{e}^{\frac{\mathbf{b W^{3/2}}}{\mathbf{E}}} \tag{2.1}$$

where j is the current density emitted by the cathode, W is the work function of the cathode (for tungsten, the work function is 4.5 eV), E is the electric field magnitude in the emission region (where the emission occurs which is in the vicinity of the apex of the cathode), b is a constant, e and m are the charge and mass of an electron, respectively, and h is Planck's constant. The minimum electric field at the cathode tip which will produce emission is a few volts per nanometer (~3 V/nm) [2, 8]. For a Butler triode configuration, the electric field (which depends on the gradient of the voltage) on the surface of the cathode is [9, 10]

$$\mathbf{E} = \frac{\mathbf{\Delta V * \beta}}{\mathbf{d}}, \tag{2.2}$$

where ΔV is the extraction voltage, β is a localized geometric field enhancement factor, and d is the distance between the extractor and the cathode. The localized geometric field enhancement factor, as its name implies, depends on the geometric shape of the tip and has a linear dependence to the magnitude of the field. As such, the shape of the tip must be carefully controlled for stable emission to occur.

2.1.1. Cathode Shaping

Shaping, necessary to achieve stable emission, is performed by "flashing" the tip, by periodically sending pulses of current through the filament. One reason for flashing is to burn off

contaminants on the surface of the tip. The tip is most stable when there is a monolayer of gas molecules covering the surface (Figure 2.3) [8, 11, 12, 13, 14]. The tip must be periodically reflashed, as additional layers of gas molecules will build up over time. The second reason for flashing is to physically shape the tip into a rough sphere, which also contributes to the emission stability (Figure 2.4) [8, 14]. Depending on the method used for shaping, typical values for the diameter of a shaped tip can be between 0.2µm and 2µm [8,13].

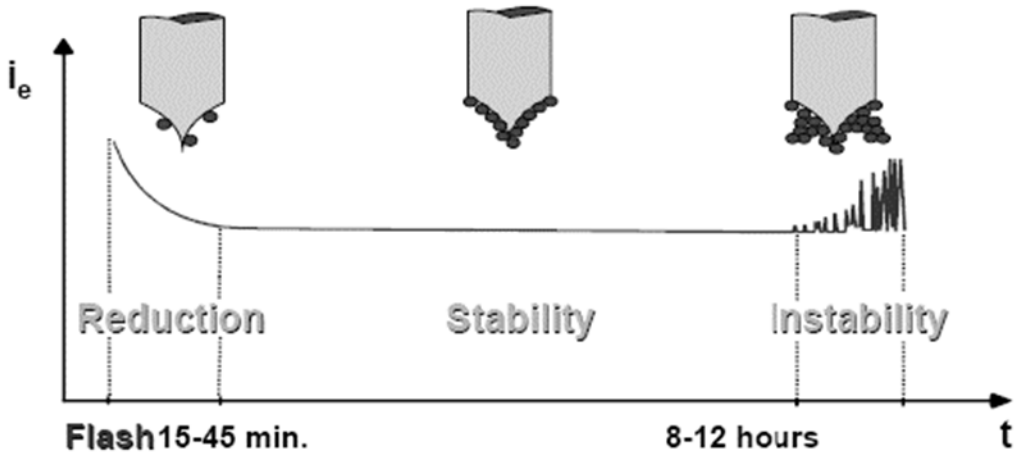

Figure 2.3 Effect of shaping by 'flashing' the tip (figure modified from Williams and Carter [11])

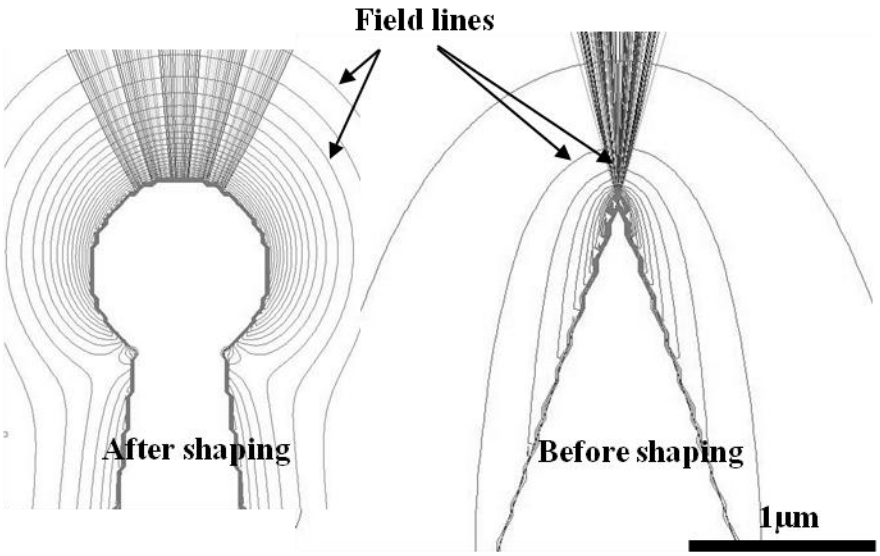

Figure 2.4 Simulation of tip before and after shaping with the electric field lines shown [8, 12].

2.1.2. Virtual Source

The emission region is the area on the surface of the cathode that produces the electrons. This emission region is different from the virtual source (Figure 2.5) [2, 4]. The virtual source is the location where the emitted electron paths (or trajectories) appear to originate. In general, when the source size is discussed in the literature (for instance ~5 nm for cold field emission), this is most likely the virtual source size, not the size of the emission region [2, 3, 4].

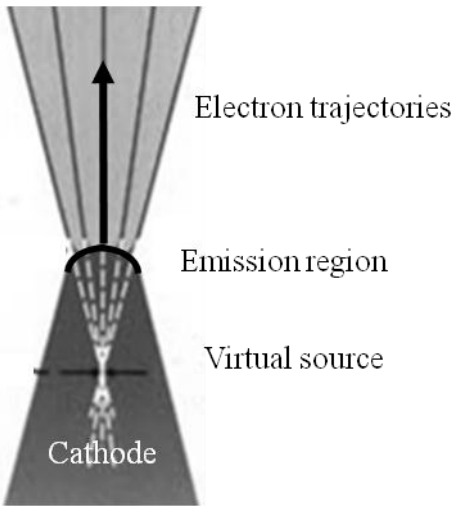

Figure 2.5 Diagram showing the virtual source and the emission region on the cathode [2,4].

2.1.3. Prototype

A prototype of the CFEG was built and tested (Figure 2.6). The prototype electron gun consists of a cold field emitter (available off-the-shelf from Hitachi High America), an extractor and a grounded anode. The maximum accelerating voltage is 10 kV and the maximum allowable extraction voltage for this prototype is 6 kV. Current emitted from the cathode was measured, as was the current which made it through the grounded anode (using a custom Faraday cup). Current *on* the grounded anode was also measured using a picoammeter. The entire gun assembly is roughly 2.5" long and 1" in diameter. Custom electronics control the emission current at an adjustable accelerating voltage.

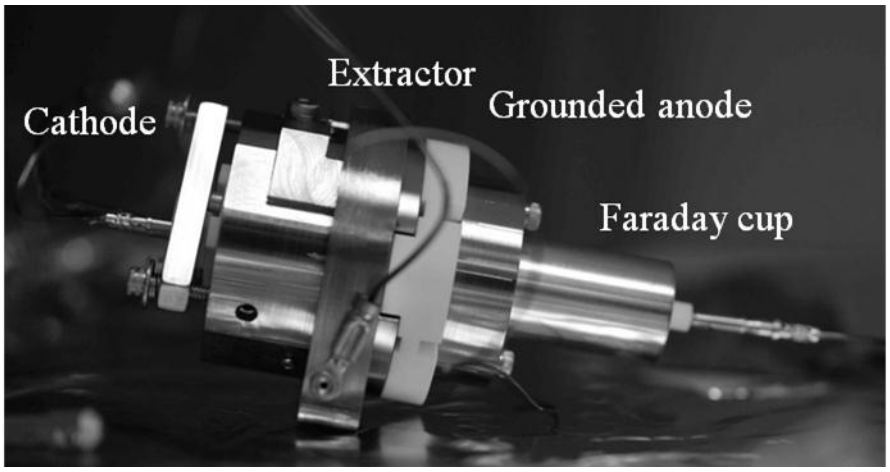

Figure 2.6 Picture of the cold field emission gun [6]. A Faraday cup was attached to the end of the prototype to measure the electrons produced by the electron gun. In this configuration, the emitter produces the electrons that are then accelerated towards the grounded anode. The current through the grounded anode was measured using the Faraday cup, and a picoammeter was used to measure current on the grounded anode.

In order to test the control electronics, a damaged, highly blunted, Cold Field Emission cathode was installed into the gun assembly. This blunted tip (BT) is robust and can operate under less stringent vacuum conditions than a newly Etched Tip (ET) should. As these tips are quite expensive (~$750 per tip), the BT allow the gun and electronics to be characterized with low risk. Figure 2.7 and Figure 2.8 show an SEM image of the ET and BT, respectively. These figures also show the respective differences in the diameters of the tips.

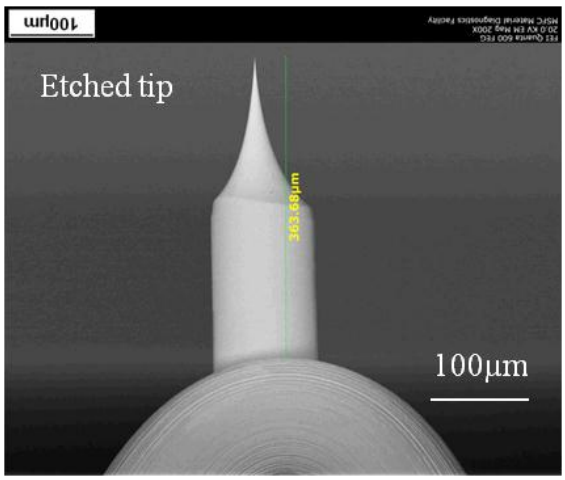

Figure 2.7 SEM image of the etched tip in the CFEG prototype. Image was taken using beam voltage of -15 kV, magnification 200 x, and obtained using an Hitachi S-3700N#1 SEM. (G. Jerman, NASA MSFC) [6, 14].

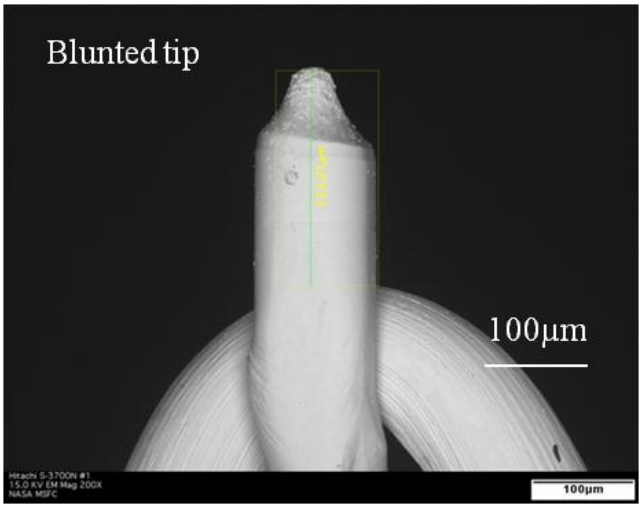

Figure 2.8 SEM image of the blunted CFE tip. Image was taken using beam voltage of -15 kV, magnification 200 x, and obtained using an Hitachi S-3700N#1 SEM. Image was taken after the etched tip had been damaged (G. Jerman, NASA MSFC) [6, 14]

It was expected that the geometric field enhancement factor for the ET should be greater than that of the BT [9, 10]. This causes the electric field at the tip of the ET to be much greater than that of the BT for the same cathode-to-extractor distance and extraction voltage (Equation (2.2)). Equation (2.1) implies that an increase in electric field should produce substantially more emission current for the same extraction voltage.

2.2. Thermionic Emission Gun

The second type of electron gun that was used to characterize the lunar mini-SEM focusing column was the thermionic electron gun (TEG). TEGs consist of a cathode, Wehnelt cylinder and grounded anode (Figure 2.9). When the cathode reaches a high enough temperature for the electrons to overcome the work function of the tungsten, electrons are emitted (Figure 2.12). The electrons are then accelerated through the anode by the voltage difference between the cathode and grounded anode. Unlike the extractor for a cold field emission gun, which is more positive than the cathode, the Wehnelt cylinder is only a few volts more negative than the cathode (typically between 5 and 10 V more negative). This, and the shape of the Wehnelt cylinder allows it to act as a weak lens and focus the electron beam to a preliminary spot to reduce the number of electrons that hit the surface of the anode (and are lost), thereby increasing the useable electron current produced by the gun (Figure 2.9) [4].

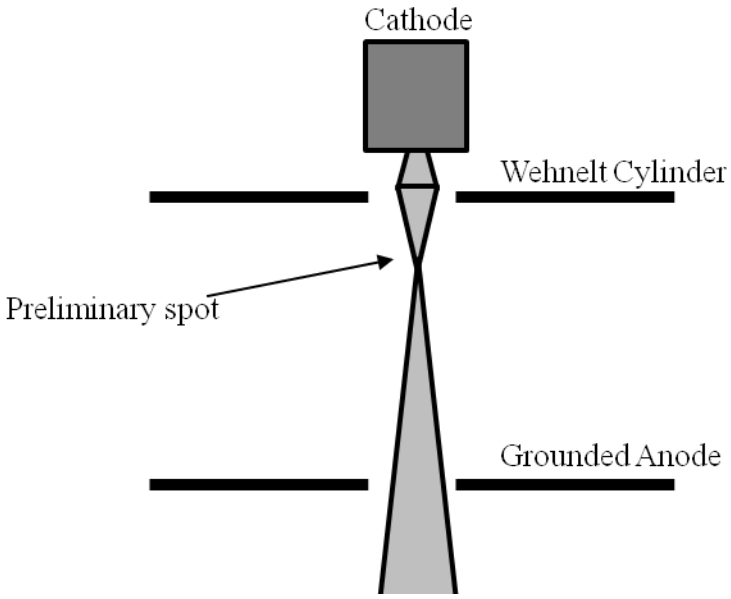

Figure 2.9 Diagram of the thermionic electron gun. The Wehnelt cylinder focuses the electron beam emitted by the cathode to increase the amount of the current that passes through the anode.

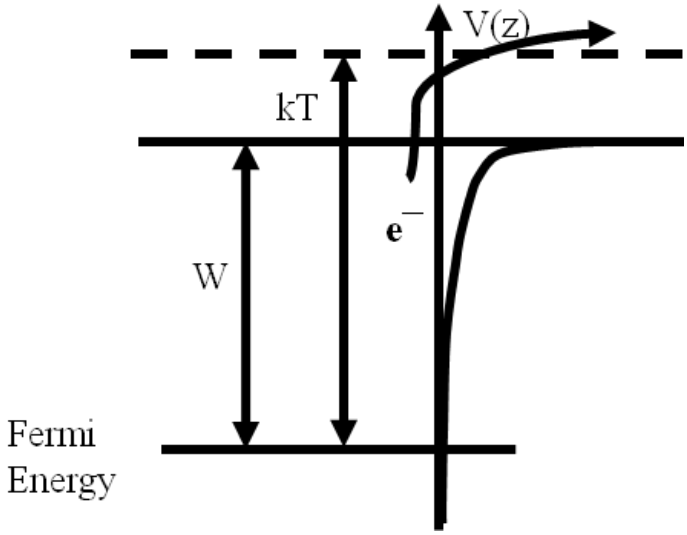

Figure 2.10 Electric potential, V(z), near the cathode surface for thermionic emission Thermionic emission is achieved by high temperatures assisting the electrons in overcoming the work function, W (figure modified from Hawkes and Kasper (1989) [4])

The governing equation for thermionic emission is the Richard-Dushman equation, written as [2, 3, 4, 11, 17]

$$\mathbf{j = AT^2 e^{-\frac{W}{kT}}} \quad , \tag{2.3}$$

where j is the current density, A is Richardson's constant which depends on the cathode material ($60 A/cm^2/K^2$ for Tungsten), T is the temperature of the cathode, W is the work function of the cathode material (4.5eV for Tungsten), and k is the Boltzmann constant. This equation suggests that the thermionic emission strongly depends on the temperature of the cathode and, unlike the CFEG, does not depend directly on the electric field at the cathode. Other fundamental differences between the CFE and the TE are listed in Table 1.1.

2.2.1. Wehnelt Cylinder

The Wehnelt cylinder controls the current by focusing the electron beam from the cathode. Moving the virtual source towards and away from the Wehnelt cylinder allows the emission current to be varied without changing the temperature of the cathode.

Shown in Figure 2.11, with the Wehnelt cylinder 'off' most electrons terminate on the surface of the grounded anode and are no longer available to the focusing column. With the Wehnelt cylinder 'on' or at voltage, the same amount of emission current is produced; however, the emission current through the anode is greater because the electron beam is focused and will pass through the anode.

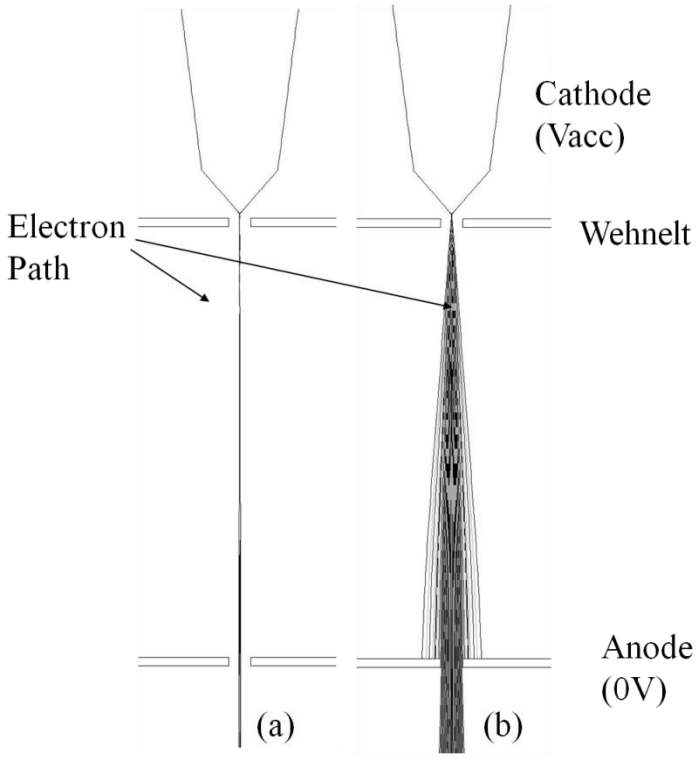

Figure 2.11 Simulation of TEG with the Wehnelt cylinder at potential, Vw, ('on') (a) and not at potential ('off') (b) [2, 3, 4, 15]. With the Wehnelt 'off' or at ground, many electrons terminate on the surface of the anode and therefore are lost. With the Wehnelt cylinder 'on', the same number of electrons is produced; however, the current through the anode is greater because the electron beam is focused into a much tighter beam; thereby, less of it will terminate on the surface of the anode.

The Wehnelt cylinder is connected to the cathode filament by a variable resistor (Figure 2.12) [2, 3, 4, 11]. As current is emitted from the cathode, it is replaced by an equal current through the resistor, generating a negative potential difference (bias) between the cathode and the Wehnelt cylinder. Since this configuration is self-biasing, as the filament current (the current that controls the temperature of the cathode) increases, the emission current follows an exponential curve until it reaches saturation. The saturation location is dependent on the resistance, R_w, of the autobias resistor. As a result, the emission current can then be controlled using the Wehnelt cylinder voltage.

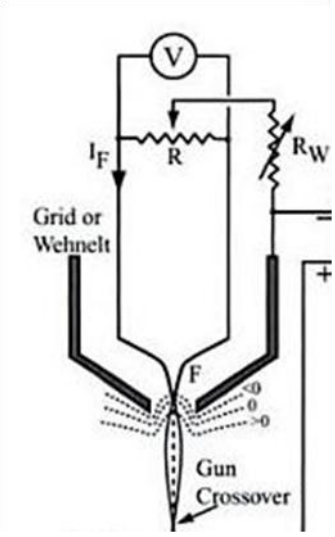

Figure 2.12 Schematic of the cathode filament (F) with Wehnelt cylinder. Rw is the variable resistor. V is the accelerating voltage, and I_F is the filament current. This configuration of cathode, resistor and Wehnelt cylinder is known as self biasing [2, 4, 11]

2.2.2. Prototype

Figure 2.13 shows the TEG prototype with the electron column and Faraday cup attached. The electron column focuses the electrons produced by the TEG while the Faraday cup detects the current at the end of the electron gun and column.

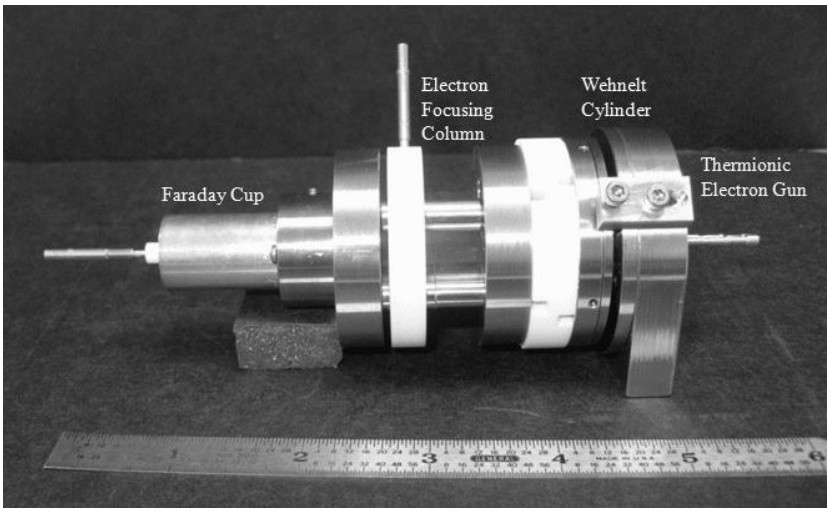

Figure 2.13 Thermionic electron gun prototype with focusing column and Faraday cup attached [6, 14]. The thermionic electron gun produces electrons that are focused by the electron focusing column. The Faraday cup measures the current that is emitted by the electron column.

The pointed filament used in this research (Type PF, AMRAY, from Energy Beam Sciences) contains a fine tungsten tip welded onto the end of the hairpin filament (Figure 2.14) [4, 18]. These tips were etched to achieve a 0.1 μm diameter. This reduction in the size of the tip reduces the focusing power necessary to achieve a small spot size; which is needed for high resolution imaging of a sample.

Figure 2.14 Image of thermionic hairpin filament without the fine tungsten tip welded on [18]

CHAPTER III

ETCHED TIP COLD FIELD EMISSION GUN

3.1 Simulation Definition

Simulations of a cold field emission gun with a shaped-etched tip cathode (ET CFEG) were performed to determine the expected emission current produced by different geometric configurations of the electron gun. (Cold field emission needs and requirements are discussed in Section 2.1.) Commercial CFEGs require a finely etched tungsten tip for operation. This tip is typically shaped, via thermal annealing, for added stability (Section 2.1.1) [1].

In order to simulate this tip and electron gun, the commercially available software, CPO2DS was used (Section 1.4) [2]. A model of the shaped etched tip (ET) is shown in Figure 3.1. In this simulation, the emission diameter (ED) is defined as the diameter of the area on the cathode where the emission is occurring, and the cathode tip diameter (CD) is defined as the diameter of the cathode shaped tip. Figure 3.2 shows the CFEG geometry, and includes the cathode, extractor, and the distance between the two.

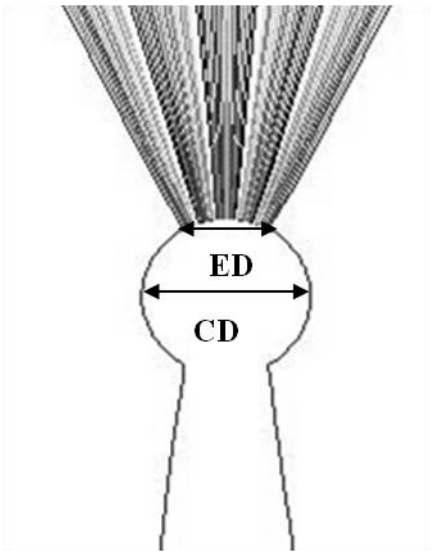

Figure 3.1 Simulation model of shaped etched tip (ET) with emission region diameter (ED) and cathode tip diameter (CD) labeled [2].

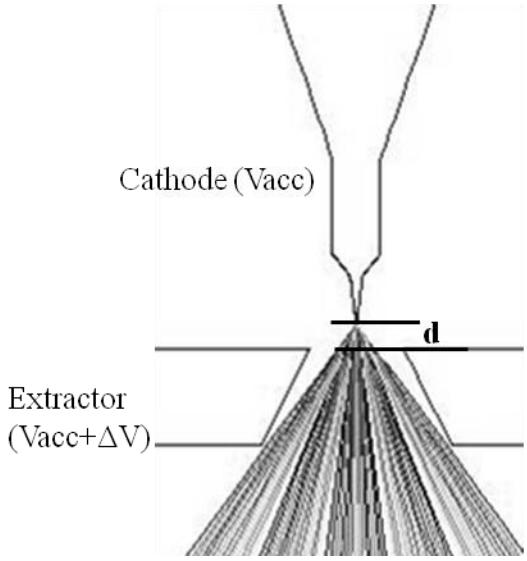

Figure 3.2 Diagram of the cathode and extractor showing the distance, d, between these two components as well as the paths of the electrons being emitted from the tip of the cathode. The cathode is at the accelerating voltage, Vacc, and the extraction voltage, ΔV, is the voltage difference between the cathode and the extractor.

The goal in the design of the electron gun is to maximize the emission current while minimizing the divergence angle associated with its emission. A small divergence angle (i.e., a smaller emission spot) is desired as this requires less demagnification

(optical power) and results in minimal aberrations. Figure 3.3 shows the emission current as a function of angle from the optical axis. The Full Width at Half Maximum (FWHM) was determined for the resulting emission profile on the cathode surface. This resulted in a 2.06 rad divergence angle. A cathode diameter of 1.5 μm was also considered, and the resulting divergence angle was 1.84 rad.

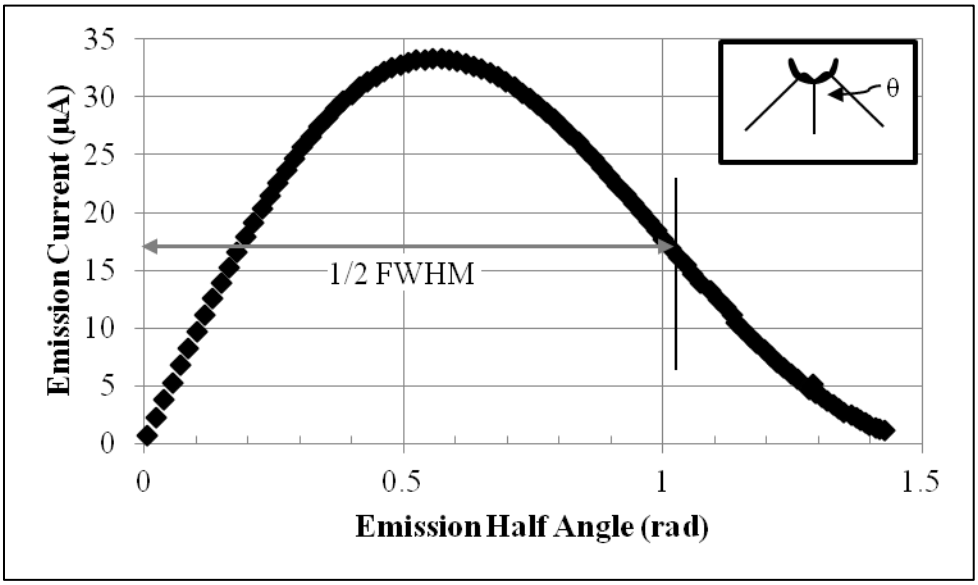

Figure 3.3 Emission current as a function of emission half angle. The divergence emission angle was determined from the full width half max (FWHM).

Figure 3.3 indicates a dip in the emission current at the center of the cathode. This is a result of the electric field being greatest near the edges of the extractor's aperture (Figure 3.4). Figure 3.5 shows the different divergence angles for different size tips. These angles were calculated from the distance between the locations (full width) of the half of the peak (half maximum) of the emission current as a function of distance from the center of the cathode.

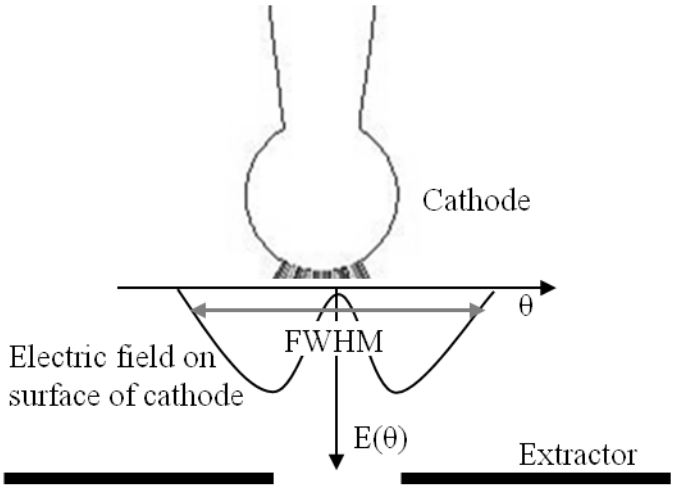

Figure 3.4 The electric field on the surface of the cathode is greatest at the edges of extractor's aperture

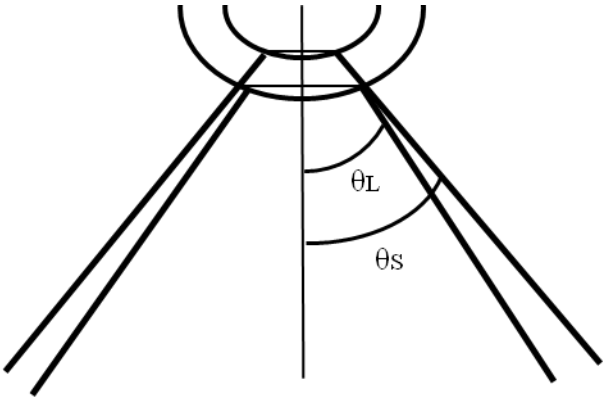

Figure 3.5 Diagram showing that for a spherical tip, the smaller the diameter of the tip, the larger the divergence angle. θ_L is the half angle for the larger diameter, and θ_S is the half angle for the smaller diameter. Changes in sizes exaggerated for clarity.

Divergence angle is also critical to the amount of emission current that makes it through the grounded anode and into the electron focusing column, and then onto the sample. To quantify this, the percentage of emission current through the grounded anode was plotted as a function of divergence angle for a distance between the extractor and the grounded anode of 5 mm and 10 mm (Figure 3.6).

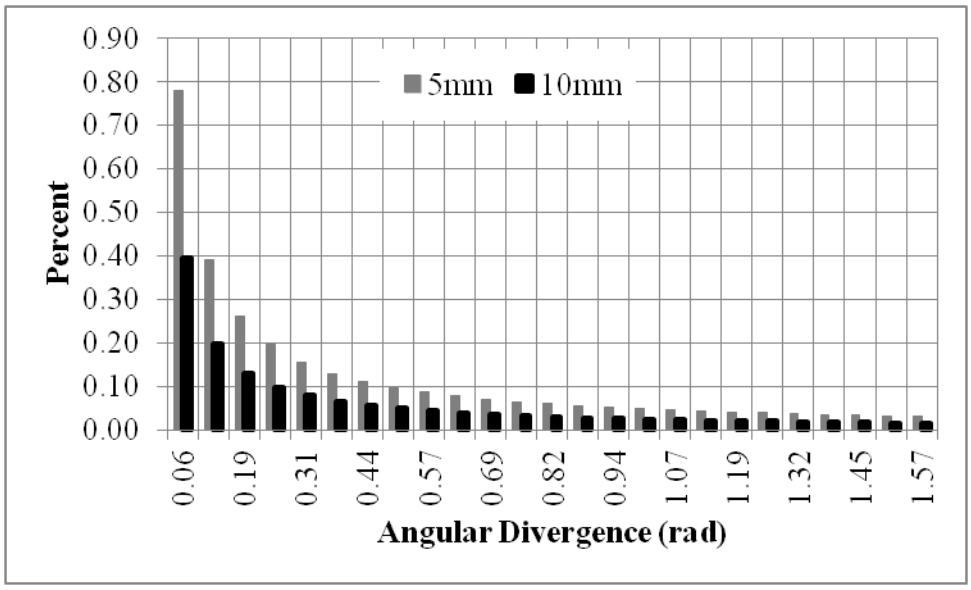

Figure 3.6 Percentage of emission current through the grounded anode as a function of angular divergence for a distance between the extractor and the anode, D, of 5 mm and 10 mm.

The percentage of current through the grounded anode decreases for large divergence angles (Figure 3.6). This particular CFEG was designed to limit electrons which have a large divergence from the paraxial. By doing so, one limits the amount of spherical aberration in the system. Simulations included the grounded anode at 5 mm and 10 mm from the extractor (Figure 3.8). Figure 3.8 shows the simulated model for the ET CFEG, and includes the grounded anode. Rays displayed in the simulation are paths of bundled electrons, which is determined from the average over a predetermined segment on the cathode (Figure 3.7) [2]. Table 3.1 compares the values used for the ET CFEG simulation to the resulting emission current and current through the grounded anode.

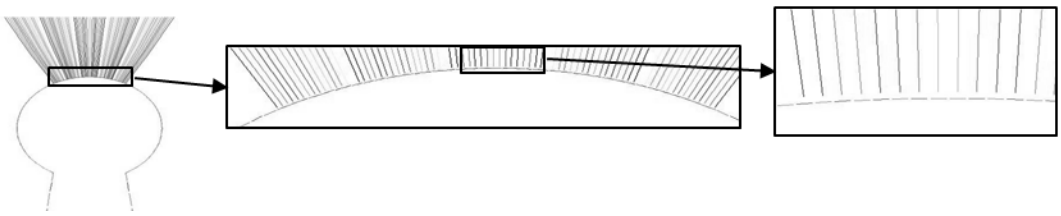

Figure 3.7 Shaped-etched tip with segments displayed on the surface of the CFE. The current associated with the 'rays' (i.e. bundle of electrons) are determined from the average over these predetermined segments on the cathode

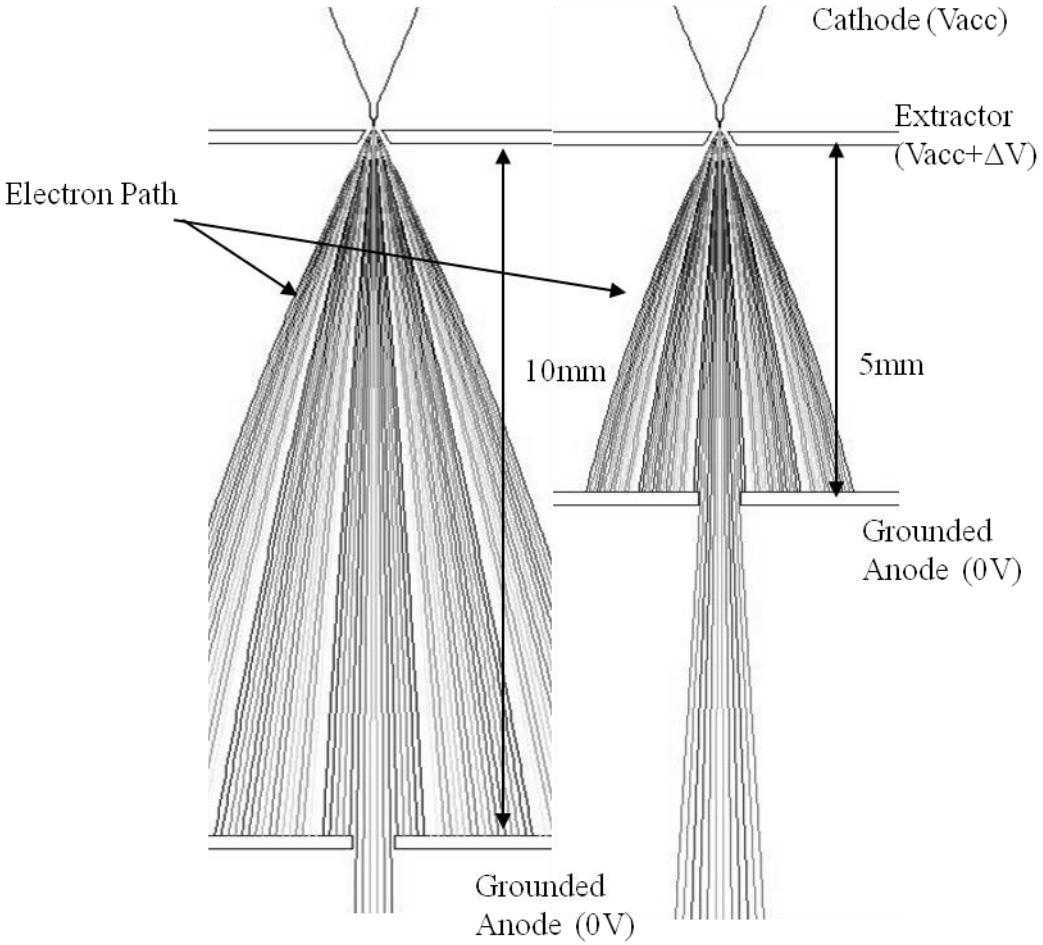

Figure 3.8 Cold field emission gun simulations with the Etched tip (ET), with a distance of 5 mm and 10 mm between the extractor and the grounded anode, are shown [2]. In this configuration, the cathode produces the electrons that are then accelerated towards the grounded anode. Rays displayed in the simulation are paths of bundles of electrons and is determined from the average over a predetermined segment on the cathode.

Table 3.1 Values used to simulate the CFEG with the shaped etched tip (ET) and the resulting emission current and current through the grounded anode [2].

	ET
Cathode tip diameter (μm)	0.9
Distance from cathode to extractor (μm)	50
Emission region diameter (μm)	0.45
Extractor aperture diameter (μm)	200
Grounded anode aperture diameter (μm)	500
Distance from extractor to grounded anode (mm)	10
Emission current (μA)	3.06
Current through the grounded anode (nA)	21.8

For comparison, the resulting divergence angle through the anode was calculated for distances between the extractor and anode of 5 mm and 10 mm (Figure 3.6, Figure 3.8 and Table 3.2).

Table 3.2 Maximum divergence angle (θ) sufficient for current through the grounded anode, calculated for distances between extractor and anode (D) of 5 mm and 10 mm.

D(mm)	**θ(rad)**
5	0.38
10	0.00045

Though the emission through the grounded anode seems small in comparison to the emission current, imaging in a typical SEM can be carried out with picoamps of current [5]. By decreasing the distance between the extractor and the grounded anode, a high percentage of the emitted current will make it through the grounded anode, at the cost of accepting higher divergence angles (Figure 3.6 and Table 3.2), which as previously stated increases the spherical aberration in the system.

3.2 Electric Field Dependencies

From the Fowler-Nordheim equation (Equation (2.1)), it is clear that the emission current has a strong dependence on the magnitude of the electric field [5, 6, 7]. To understand this dependence, the magnitude of the electric field at the emission region and the emission current was determined as a function of distance between the cathode and the extractor, d, (Figure 3.2, Figure 3.9 and Figure 3.10). Figure 3.9 shows the electric field as a function of distance between cathode and the extractor, and Figure 3.10 shows the emission current as a function of the same distance.

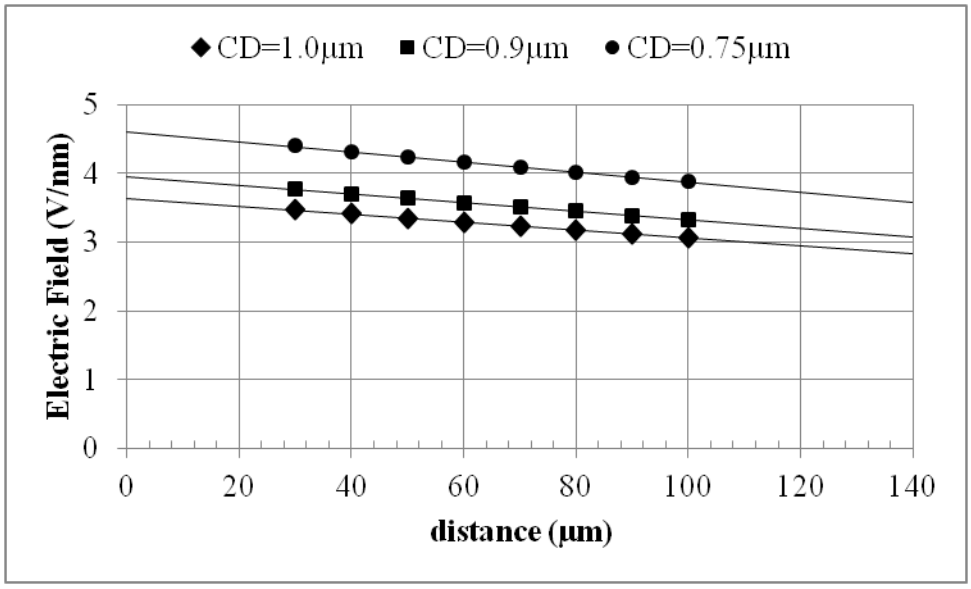

Figure 3.9 Electric field magnitude (E) at the emission region as a function of distance between the cathode and the extractor (with linear fit) for cathode tip diameters (CD) of 0.75 μm, 0.9 μm and 1.0 μm. The emission diameter (ED) was set to be half of the tip diameter.

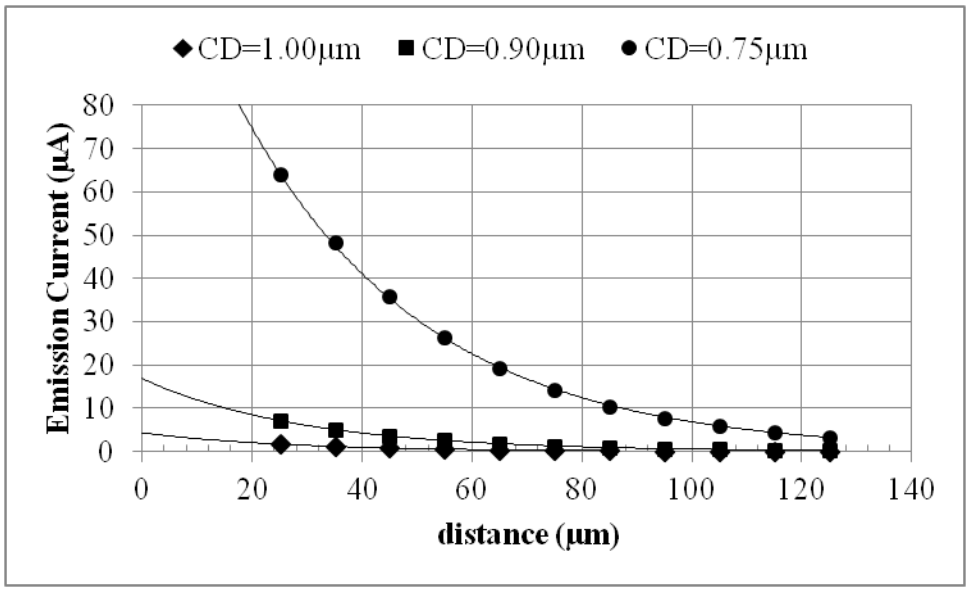

Figure 3.10 Emission current as a function of the distance between the cathode and the extractor (with exponential fit) using an emission diameter set to half the cathode tip diameter. Cathode tip diameters were 0.75 µm, 0.9 µm and 1.0 µm.

The electric field in the emission region decreases as the cathode tip diameter increases, which suggests that the emission current is inversely proportional to the cathode tip diameter (Figure 3.9) (discussed in Section 3.4). In addition, the electric field at the emission region also decreases as the distance between the cathode and the extractor increases (Figure 3.9), as expected.

It is evident from these figures that very small changes in the electric field can correspond to very large changes in the emission current (Figure 3.9 and Figure 3.10). For the instance of the cathode tip diameter being 0.75 µm, the electric field decreases by 1 V/nm while the emission current decreases by 60 µA. A significant difference is predicted by the Fowler-Nordheim equation (Equation (2.1)) which shows that the emission current is exponential with electric field.

In Figure 3.10, the emission current is shown to be inversely proportional to the distance between the cathode and the extractor, which was predicted by a combination of

the Fowler-Nordheim equation (Equation (2.1)) and Equation (2.2). Figure 3.10 also shows the emission current is less sensitive to the cathode tip diameter for larger distances between the cathode and the extractor. As the distance between the extractor and cathode increases, the less the emission current depends on the shape of the tip of the cathode.

The current through the grounded anode was simulated, and it was determined that the percentage of current that made it through was fairly insensitive to cathode tip diameters of 0.75 μm and 1.0 μm, for distances of 20 μm through 120 μm (for a change of distance by 100 μm, the percentage ,only changed by 0.03%). This is due to the fact that, for this geometrical configuration and voltage settings, even though the diameter of the cathode changed, the relative virtual source size did not appreciably change. If conditions were such that the emitter current density increased, one would expect a broadening, $d_{vs,}$ of the virtual source diameter. This broadening is defined as [1, 8]:

$$d_{vs} \propto \frac{CD^2 * j^{2/3}}{4 * Vacc^{7/6}}, \tag{3.1}$$

where j is the emission current density, CD is the cathode tip diameter, and Vacc is the accelerating voltage.

Geometrically, the current through the anode is predicted to be relatively independent to the distance between the extractor and the anode as well. In order for the vignetting to be affected by changes in this distance, the extractor needs to be moved by large amounts (Figure 3.11) (which would reduce the emission current because of the electric field dependence).

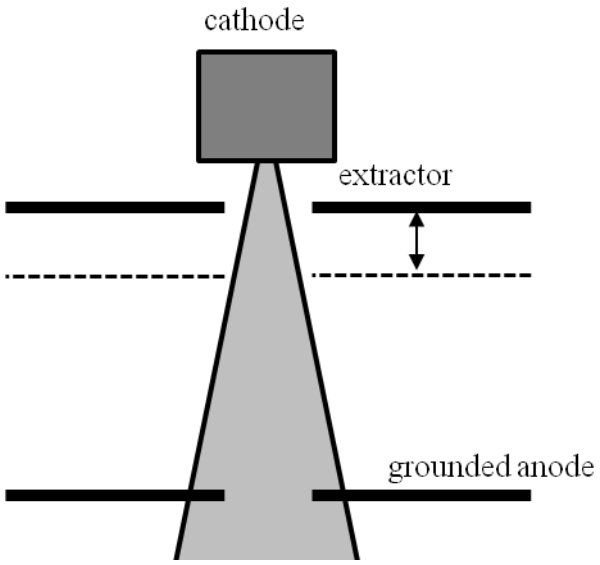

Figure 3.11 Image of the translation of the extractor

Figure 3.11 also shows that if the grounded anode is moved with respect to the extractor, the vignetting would be affected. Once again, another disadvantage of moving the grounded anode closer to the extractor (which would increase the amount of current through the grounded anode) would allow for higher divergence angles to pass through to the focusing column; potentially increasing the amount of spherical aberration in the system, which would need to be corrected for.

3.3 Extraction Voltage Dependencies

The Fowler-Nordheim equation (Equation (2.1)) quantifies the dependence of the emission current density on the electric field at the cathode [5, 6, 7]. This electric field is, in-turn, dependent on the extraction voltage, ΔV, and the geometry in the vicinity of the cathode, such as the size and shape of the cathode tip and the distance between the cathode and extractor (Equation (2.2)) [9, 10]. The extraction voltage is the voltage difference between the cathode and the extractor (Section 2.1). Equation (2.2) predicts

that the electric field has a linear dependence on the extraction voltage. The electric field was simulated for a non-shaped ET and a shaped ET as a function of the extraction voltage (Figure 3.12).

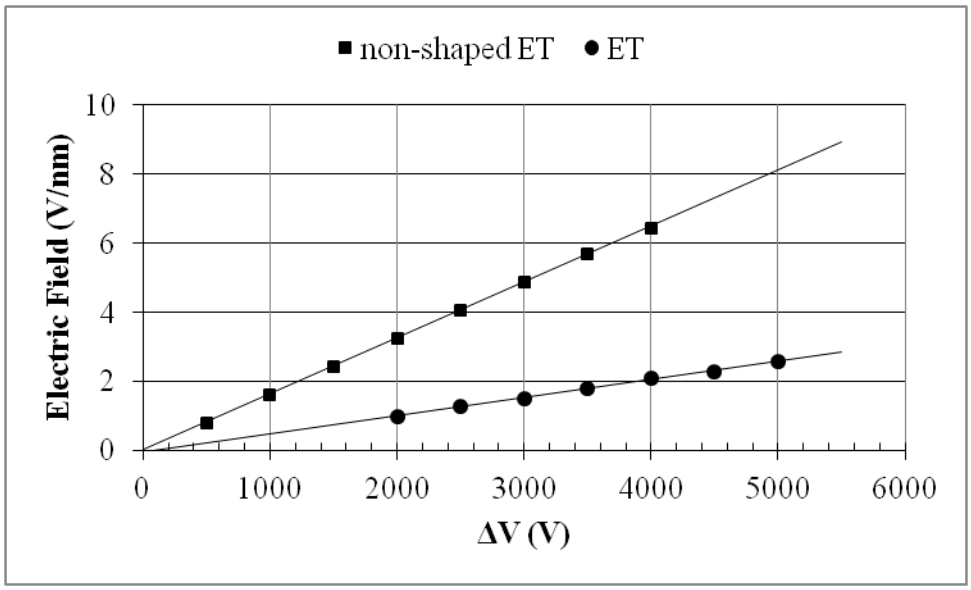

Figure 3.12 Electric field as a function of the extraction voltage for the CFEG with the non-shaped etched tip (ET), and the shaped ET with a linear fit. The geometric enhancement factor can be determined from the linear slope (below).

Figure 3.12 shows the linear dependence on electric field on the extraction voltage that was predicted by Equation (2.2) [9, 10]. For the non-shaped ET, the geometric field enhancement factor was approximated to be 326 and for the shaped ET, approximated to be 152. As predicted, the ET without shaping has a much higher electric field and increases rapidly with the extraction voltage [1, 8, 11]. The shaped ET, on the other hand, shows a less steep slope than the non-shaped ET, indicating smaller changes to the electric field with increased extraction voltage, and allowing for more stable operation [5, 11].

3.4 Emission Region Dependencies

The emission diameter (ED) is different from the virtual source diameter as discussed in Section 2.1.2 and is defined in Figure 3.1. In Section 3.2, the electric field and emission current were described as roughly inversely proportional to the emission diameter. To substantiate this, the emission current was simulated as a function of the emission diameter (Figure 3.13).

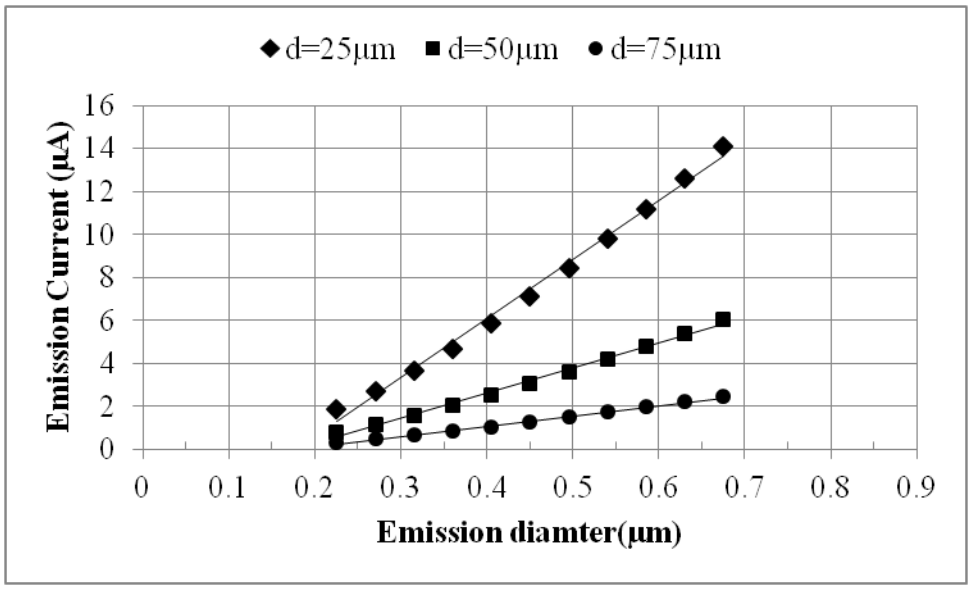

Figure 3.13 Emission current as a function of the emission diameter (with linear fit) for the following distances between the extractor and cathode: 25 μm, 50 μm and 75 μm. The diameter of the cathode tip was set to 0.9 μm.

The emission current is linearly proportional to the emission diameter (Figure 3.13). Figure 3.13 also shows that the emission current is inversely proportional to the distance between the cathode and the extractor, as predicted by Equation (2.2) (Section 3.2).

Changing the emission diameter (which changes the geometry) will influence how much current will be transmitted through the grounded anode. To isolate the effects from

vignetting from changes in the electric field, the percentage of the emission current that was transmitted through the grounded anode was calculated as a function of the emission diameter (Figure 3.14).

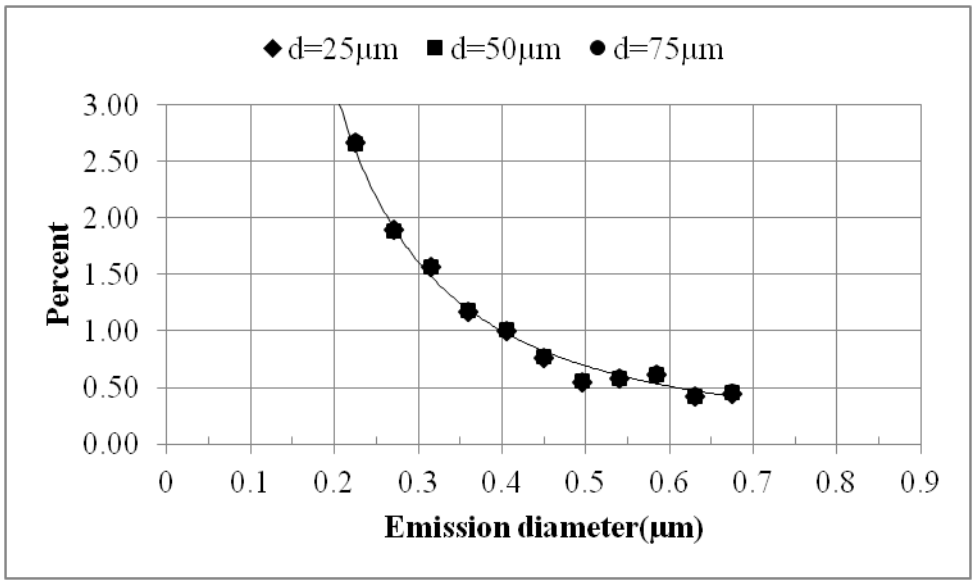

Figure 3.14 Percentage of emission current transmitted through the grounded anode as a function of the emission diameter (with exponential fit) for the following distances between the extractor and cathode: 25 µm, 50 µm, and 75 µm. The diameter of the cathode tip was set at 0.9 µm. The percentage of emission current transmitted through the grounded anode is dependent on the distance between the cathode and the extractor (discussed in Section 3.2). The percentage of emission current was insensitive to the distance, d.

The percentage of the emission current transmitted through the grounded anode is inversely proportional to the emission diameter (Figure 3.14). Figure 3.14 also show that the distance between the cathode and the extractor only slightly affects the percentage of the emission current transmitted through the grounded anode, for the values simulated (Section 3.2).

Smaller emission regions reduce the angle into which the electrons are emitted, thereby, increasing the number of electrons moving through the grounded anode (Figure

3.15). However, the result of the two trends on the emission region (increasing emission current and decreasing percentage with emission diameter) is that the current through the grounded anode is roughly independent of the emission region diameter due to the simulated geometric configuration (Figure 3.15 and Figure 3.16).

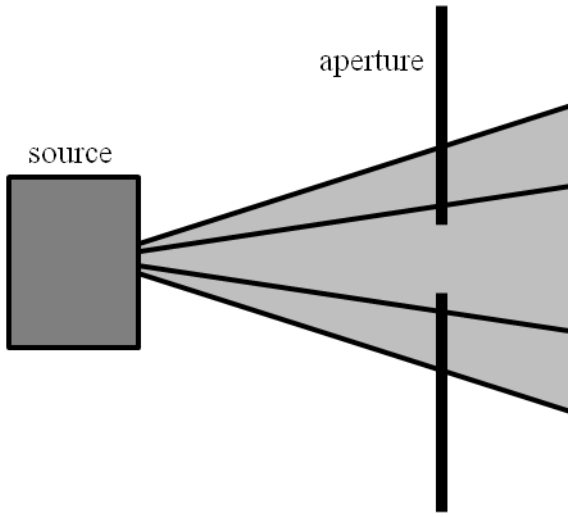

Figure 3.15 Vignetting for different sized emission regions. The emitter, designated source in this figure, produces electrons. The grounded anode, designated aperture, stops a significant percentage of the electrons produced by the source. Smaller emission regions produce narrower beams, and for narrower beam widths, the amount of electrons stopped by the aperture will be less.

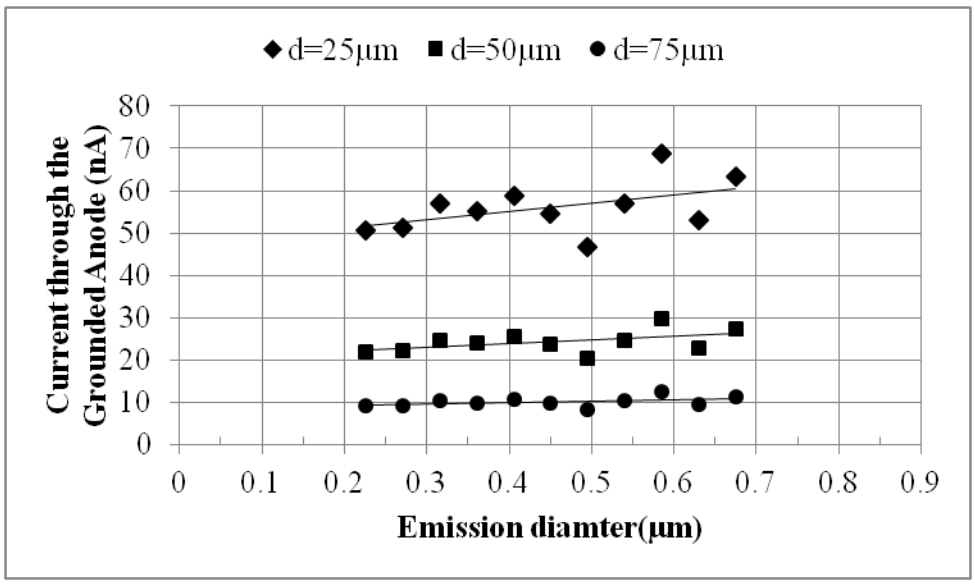

Figure 3.16 Current through the grounded anode as a function of emission diameter (with a linear trend) for the following distances between the extractor and cathode: 25 µm, 50 µm, and 75 µm. The diameter of the cathode tip was set to 0.9 µm.

3.5 Cathode Diameter Dependencies

The cathode tip diameter (CD), as defined in Figure 3.1, is the full diameter of the shaped cathode tip. This parameter is dependent on how much shaping has been performed and on the method of shaping. The emission current and current transmitted through the grounded anode was simulated as a function of the cathode tip diameter (Figure 3.17).

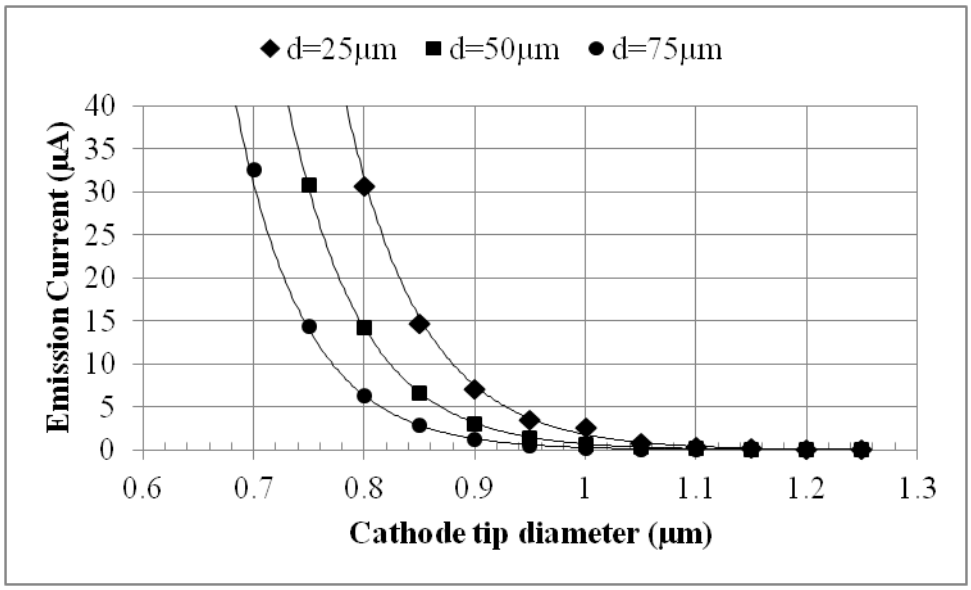

Figure 3.17 Emission current as a function of the cathode tip diameter (with exponential fit) using a simulated emission diameter of half the cathode tip and the cathode-to-extractor distances of 25 µm, 50 µm and 75 µm.

As expected, the emission current decreases inversely with the cathode tip diameter (Figure 3.17). The decrease in emission current as the tip becomes larger over time (due to repeated flashing) is not expected to significantly impact imaging of the sample, as a minimum of ~1 pA of current is needed for quality imaging [5]. To understand the effect of vignetting, the percentage of emission current transmitted through the grounded anode was calculated as a function of the cathode diameter (Figure 3.18).

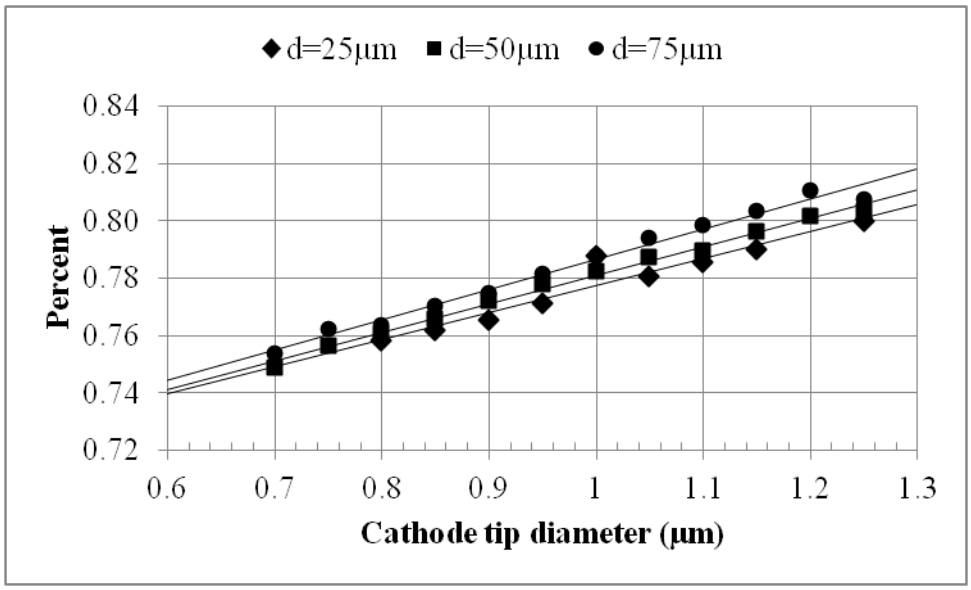

Figure 3.18 Percentage of emission current transmitted through the grounded anode as a function of the cathode tip diameter (with linear fit) for an emission diameter of half the cathode tip diameter and cathode-to-extractor distances of 25 µm, 50 µm and 75 µm.

The two trends (emission current and percentage of current with cathode tip diameter) (shown in Figure 3.17 and Figure 3.18) implies that there is an optimal cathode diameter tip size range and an optimal emitter to cathode distance range necessary to maximize the emission through the grounded anode and the produce stable emission.

The emission current transmitted through the grounded anode increases as the cathode tip diameter increases is a result of changes in geometric configuration of the electron gun and changes in the divergence angle associated with the emission (Figure 3.5).

3.6 Conclusions

Due to its high current density, small source size and long lifetime the CFEG with a shaped-etched tip is the ideal electron gun for use in the lunar miniaturized SEM. Expected emission current, current through the grounded anode, and current terminating

on the surface of the grounded anode are listed as a function of emitter to extractor distance, for a extractor to grounded anode distance of 10 mm (Table 3.3). Listed in Table 3.4 are the same currents with a distance between extractor and anode of 5 mm. These were calculated using geometrical principles and the Fowler-Nordheim equation (Equation (2.1)). In both cases, the acceleration voltage was set to -10 kV, the extraction voltage was 3.5 kV, the emission cone half angle was set to 45 degrees and the emission region diameter was set to 0.9 μm.

Table 3.3 Idealized emission current, current through the grounded anode and current on the grounded anode for different distances between the cathode and extractor, d, for the CFEG with etched tip. The distance between the extractor and the grounded anode was 10 mm.

d(μm)	Emission current (μA)	Current through grounded anode (μA)	Expected current on grounded anode (μA)
50	39.87	0.50	39.37
100	19.94	0.25	19.68
150	13.29	0.17	11.07
200	9.97	0.12	6.20

Table 3.4 Idealized emission current, current through the grounded anode and current on the grounded anode for different distances between cathode and extractor (d) for the CFEG with etched tip. The distance between the extractor and the grounded anode was 5 mm.

d(μm)	Emission current (μA)	Current through grounded anode (μA)	Current on grounded anode (μA)
50	39.87	1.00	38.87
100	19.94	0.50	19.44
150	13.29	0.33	10.9
200	9.97	0.24	6.08

Comparing Table 3.3 to Table 3.4 shows that by reducing the distance between the extractor and the grounded anode, more current passes through the grounded anode

(and therefore is available to the following components in the electron microscope). However, the advantage of increased current must be weighted against the disadvantage of the increased dispersion angle of the electron beam (which increases the amount of aberration). Though this aberration can be corrected for in the column, it would require additional design elements.

Through this research the following was determined:

- The electric field was shown to be inversely dependent on the distance between the cathode and the extractor, and directly dependent on the extraction voltage as predicted by Equation (2.2).
- The electric field was shown to be inversely dependent on the cathode tip diameter, and therefore, also inversely dependent on the emission region diameter.
- As expected the shaped ET had a much lower electric field at the emission region than the non-shaped ET, for the same conditions.
- The emission current was shown to increase with emission region diameter, and to decrease exponentially with cathode tip diameter, and distance.
- The percentage of the emission current transmitted through the grounded anode decreases exponentially with emission region diameter, increases with cathode tip diameter, and is approximately independent of the distance between the cathode and the extractor.

From these results optimal values for the various parameters investigated were determined (Table 3.5). These values are based on simulation results and on the

geometric restrictions of the lunar mini-SEM mechanical design and the requirement that the current at the sample be no less than 1 nA (more than sufficient for imaging and x-ray analysis) [5].

Table 3.5 Settings for optimal cathode diameter, extractor to cathode distance, and extractor to anode distance and the predicted emission current and current through the grounded anode for the cold field emission gun with the shaped etched tip (ET). These values were chosen to achieve 1 nA of current at the sample.

	ET
Cathode tip Diameter (μm)	0.7-0.8
Extraction Voltage (kV)	3-4
Cathode to Extractor Distance (μm)	75-100
Extractor to Grounded Anode Distance (mm)	8-10
Minimum Emission Current (μA)	30
Minimum Current through Grounded Anode (nA)	5

To maximize the current at the sample, a small cathode tip diameter must be used. This allows for a moderate cathode to extractor distance to be employed; allowing for stable emission and fairly high emission currents. The extractor to grounded anode distance has been chosen to minimize the dispersion angle, which results in minimal spherical aberration, while maintaining reasonable current through the grounded anode.

CHAPTER IV

BLUNTED TIP COLD FIELD EMISSION GUN

4.1 Simulation Definition

Laboratory testing of the prototype cold field emission gun (CFEG) was carried out using a blunted Cold Field Emission cathode. As these Cold Field Emission tips are relatively expensive and under improper vacuum and control conditions, can be subject to damage, the majority of testing was carried out using a previously damaged (highly blunted) tip. To understand the results from the lab tests and to optimize the mechanical configuration of the CFEG, simulations were performed (Cold field emission and the operational requirements for a CFEG are discussed in Section 2.1.). At the cost of beam stability, and small emission region, the blunted tip cathode (BT) is considerably more robust than a newly etched tip (ET), and can operate under less stringent vacuum conditions (Figures 2.7 and 2.8 shows SEM images of the ET and BT, respectively).

The BT CFEG prototype was extensively tested in an Ultra-High Vacuum chamber with a custom control system [1]. Emission current, current after the extractor and current on the grounded anode were measured, using a custom Faraday cup, for various accelerating voltages and for a fixed cathode to extractor spacing. This spacing is smaller than that of the ET CFEG, so that a manageable (3-4 kV) extraction voltage could

be applied to incite emission. Additionally, the resulting emission was imaged using a phosphor screen, followed by a glass viewport and CCD camera.

Prior to testing, the cathode used for these tests was imaged using a commercial SEM located in the Materials and Processing Laboratory at MSFC (Figure 4.1). This particular cathode was badly damaged during previous testing and as a result, has multiple small protrusions on its surface.

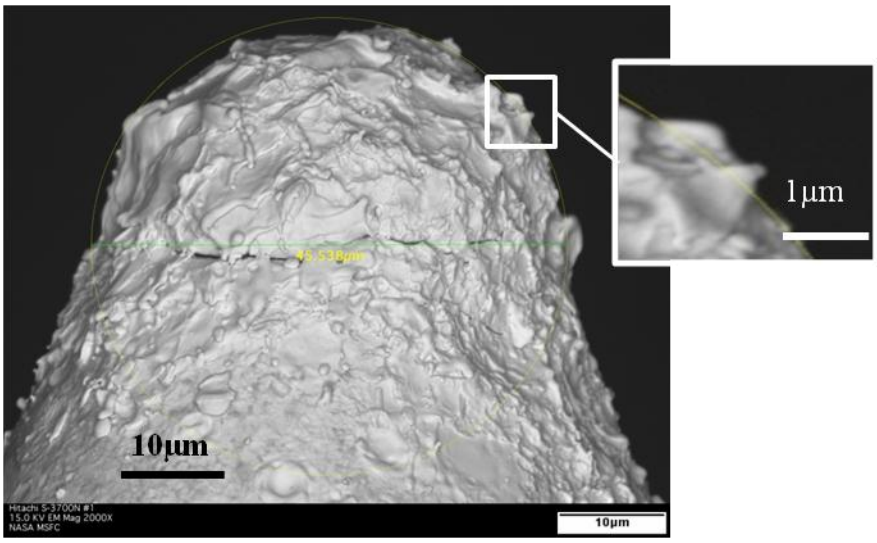

Figure 4.1 SEM image of the blunted tip used for testing the CFEG prototype [1]. Image was taken using beam voltage of -15 kV, magnification 2000 x, and obtained using a Hitachi S-3700N#1 SEM (G. Jerman (NASA MSFC)). Inset is a magnification of a typical protrusion (height approximately 0.5 µm and base diameter just less than 1 µm).

Figure 4.2 shows an image of the simulation of the BT with multiple protrusions on the surface and with the emission region diameter and cathode tip diameter labeled. Charge Particle Optics in Two Dimensions with Sources (CPO2DS), commercially available software, was used to perform the simulations [2].

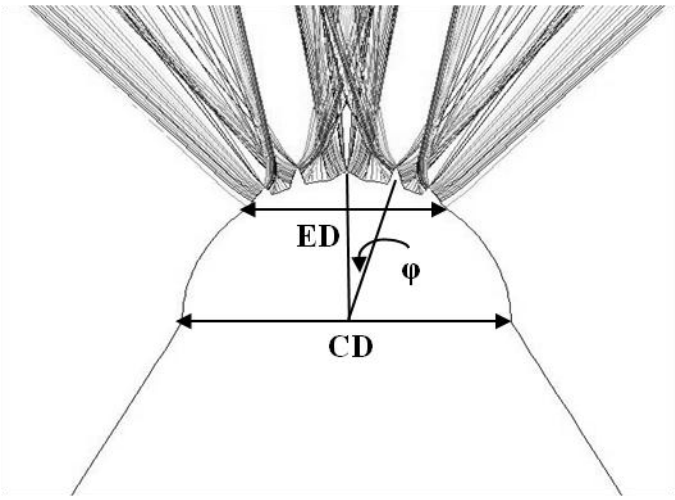

Figure 4.2 Image of simulation of blunted tip (BT) with emission region diameter (ED) and cathode tip diameter (CD) labeled [2]. The multiple protrusions were simulated to approximate the protrusions in Figure 4.1. The orientation angle of an off-axis protrusion is designated 'φ.'

Figure 4.3 shows the cathode, the extractor and the distance between them. Table 3.1 lists typical values for the simulation of the BT CFEG. The BT CFEG geometry is based on estimations of the prototype BT CFEG. Figure 4.4 shows the simulation of the CFEG with the blunted tip.

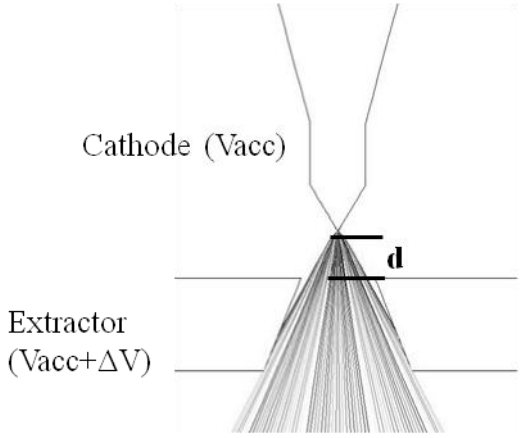

Figure 4.3 Blunted tip cathode and extractor with distance between them is shown [2]. Rays displayed in the simulation are paths of bundles of electrons, which is determined from the average over a predetermined segment on the cathode.

Table 4.1 Values used to simulate the CFEG with the blunted tip (BT) and the resulting emission current and current through the grounded anode [2].

	BT
Cathode tip diameter (μm)	40
Distance from cathode to extractor (μm)	50
Emission region diameter (μm)	20
Extractor aperture diameter (μm)	200
Grounded anode aperture diameter (μm)	500
Distance from extractor to anode (mm)	10
Emission current (μA)	1.25
Current through the grounded anode (nA)	0.397

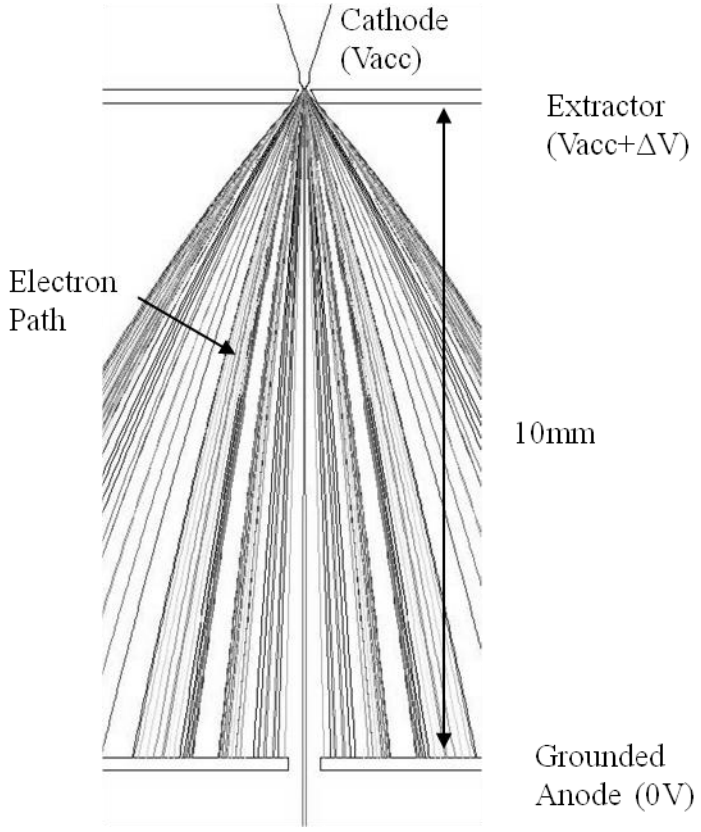

Figure 4.4 Simulation of the cold field emission gun with the blunted tip [2]. In this configuration, the cathode-extractor geometry and extraction voltage produce the electrons that are accelerated forward towards the grounded anode. Rays displayed in the simulation are paths of a bundle of electrons. Each ray originates at the center of a predetermined segment used to define the surface of the cathode

4.1.1 Surface Protrusions

In comparing the aforementioned simulated emission current to that produced during testing, results did not coincide. This section and the following investigate the factors that may have led to this discrepancy. Specifically, the presence of multiple protrusions on the surface of the cathode can result in multiple emission sites (Figure 4.1 and Figure 4.2). Multiple emission sites cause unstable emission, which makes imaging difficult, if not impossible, to carry out (Section 4.1.2).

The shape and location of each of the protrusions dictates the field at that point. The strength of this field directly relates to the potential emission from that protrusion. From Figure 4.1, it is observed that typical protrusions are roughly cone-like; though, many did have irregular sides. To approximate these protrusions, a flat-topped cone was generated. Though this is not realistic depiction of a protrusion, it allows for a relative comparison to be made between different protrusion geometries. For a first approximation, a single protrusion was placed in the center (on the optical axis) of the BT (Figure 4.5).

The size and shape of this protrusion was varied and results were compared. Figure 4.6 shows the simulation of a flat-topped protrusion on the surface of the cathode tip with the diameter, PD, and height, PH, and emission region, ED_p. The measured values of the BT CFEG prototype were used to set parameters for the simulated results.

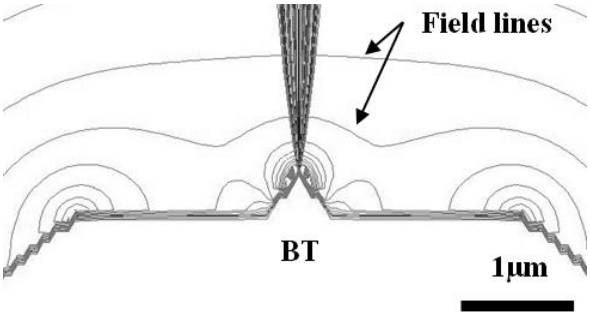

Figure 4.5 Blunted tip with a single on-axis protrusion, with the electric field lines surrounding the tip shown [2].

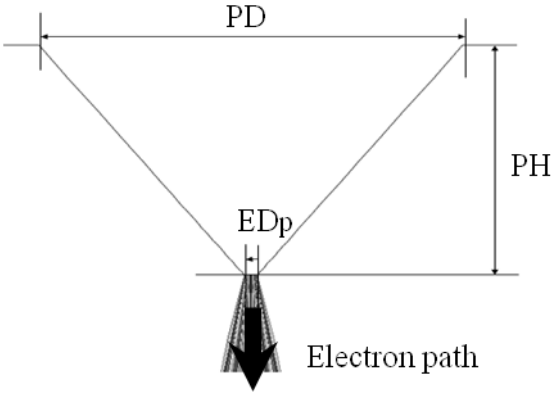

.

Figure 4.6 A flat-topped protrusion on the surface of the cathode tip with the diameter of the base (PD), height (PH) of the protrusion labeled and the protrusion emission diameter (ED_p) [2].

Figure 4.7 shows the emission current as a function of the protrusion diameter for different emission diameters, while Figure 4.8 shows the emission current as a function of the protrusion height for different protrusion diameters. The emission was confined to the flat-top (which was set to a 14 nm diameter) of the single on-axis protrusion, protrusion emission region (Figure 4.5 and Figure 4.6).

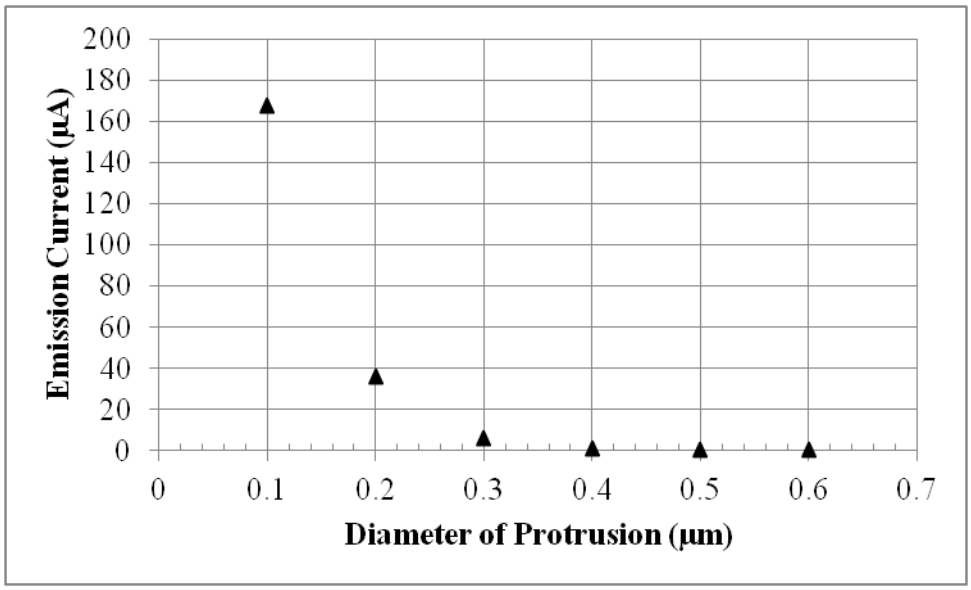

Figure 4.7 Emission current as a function of the protrusion diameter for protrusion emission diameters, ED_p, of 14 nm. This was for a protrusion height of 0.3 µm and a distance between cathode and extractor of 100 µm.

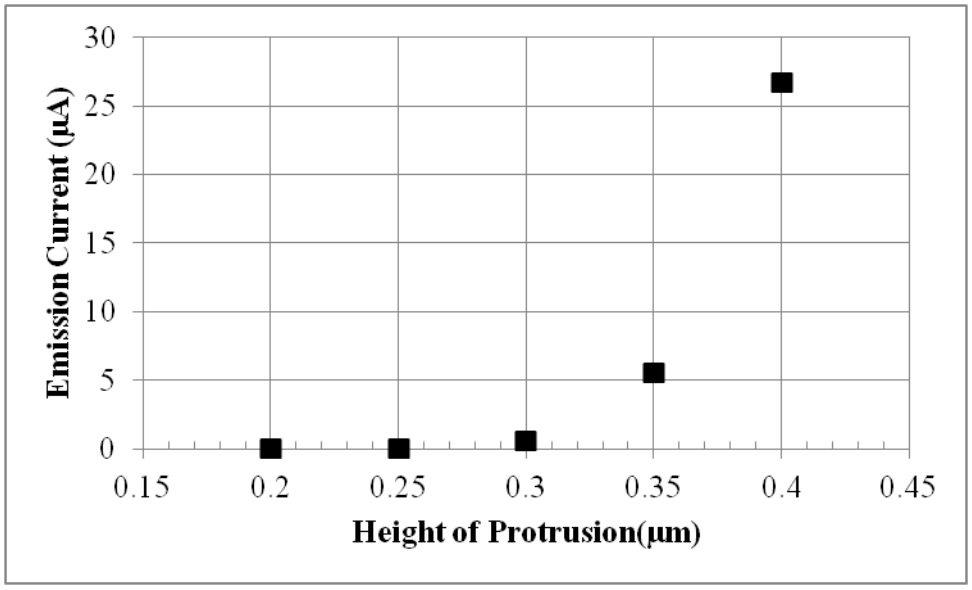

Figure 4.8 Emission current as a function of the protrusion height, for protrusion diameter of 0.4 µm. This was for a protrusion emission diameter of 14 nm and distance between cathode and extractor of 100 µm.

Figure 4.7 shows that the emission current decreases with the diameter of the protrusion while Figure 4.8 shows that the emission current increases with the height of

the protrusion, consistent with results for the ET (Ch 3). A small change in the protrusion diameter, 100 nm, makes a large difference to the emission current. Likewise, a 50 nm difference in protrusion height for a given protrusion diameter makes a large difference to the emission current.

Comparing these results to the experimental results, three general cases were chosen to determine an approximate size of the protrusion (Figure 4.9). CASE 1 had a protrusion with a diameter of 0.4 µm and a height of 0.3 µm. CASE 2 had a protrusion with a diameter of 0.4 µm and a height of 0.4 µm, and CASE 3 had a protrusion with a diameter of 0.6 µm and a height of 0.4 µm. Table 4.2 compares the some of the results from each of these different cases. For these simulations, the accelerating voltage was set to -10 kV, the extraction voltage was set to 3.5 kV, and the cathode tip diameter (CD) was set to 40 µm. The emission region was confined to the flat-top of the cone-like protrusion, (protrusion emission region diameter set to 14 nm), and the electric field was measured near the center.

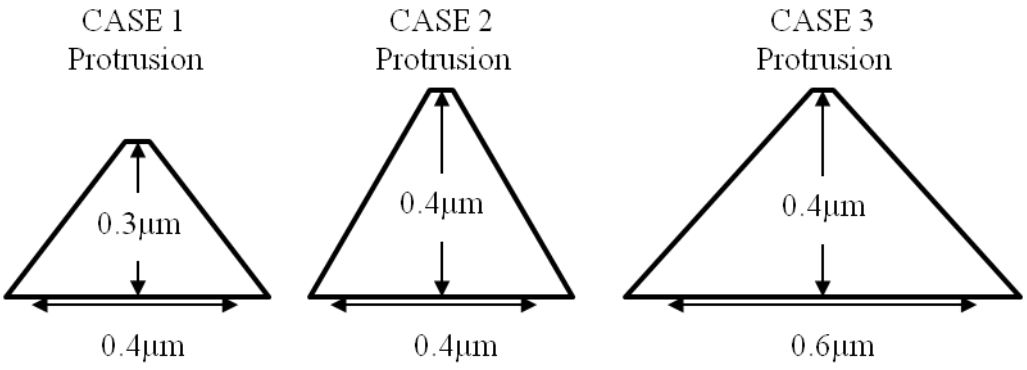

Figure 4.9 Protrusion sizes for the three different cases. These values were chosen based on information from the previous two figures.

Table 4.2 The magnitude of the electric field (E) at the emission region, the emission current (Ic) and the amount of the emission current transmitted through the grounded anode (Ia/Ic) for CASE 1, 2, and 3.

CASE	E(V/nm)	Ic (μA)	Ia/Ic
1	1.28	0.63	8.38E-05
2	1.75	27.2	4.68E-05
3	1.41	1.20	1.40E-04

Table 4.2 shows that the electric field (and thereby the emission current) was greater for both a taller and narrower protrusion which was previously observed in Figure 4.7 and Figure 4.8. Table 4.2, also, shows that, for shorter protrusions, the amount of current through the grounded anode compared to the emission current was lower, while for taller protrusions, it was higher.

4.1.2 Multiple protrusions

Laboratory testing of the CFEG with a phosphor screen, followed by a CCD camera has shown the presence of multiple emission sites from the cathode. The majority of the current emitted was measured to fall on the second anode. This was probably due to misalignment of the cathode to the second anode and to the irregular shape (irregular surface protrusions) of the BT (Figure 4.1). Figure 4.10 shows images of a phosphor screen aligned with the geometric optical axis of the CFEG during testing.

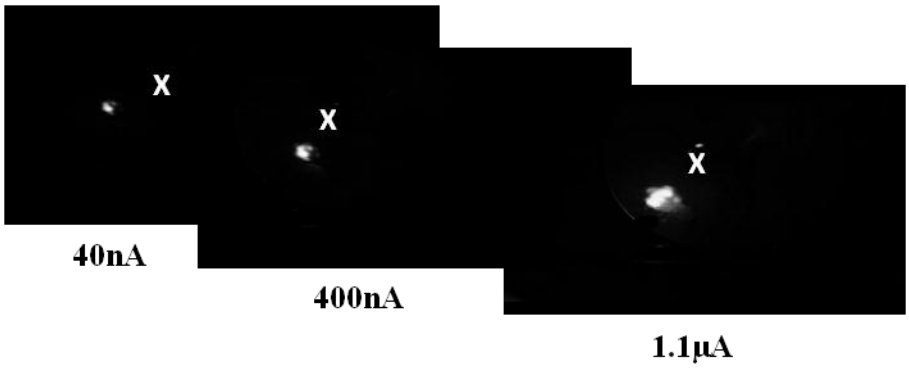

Figure 4.10 Images of a phosphor screen aligned with the optical axis of the BT CFEG for various emission currents during emission. "X" denotes the experimentally determined center axis of the CFEG. The emission is most likely occuring from multiple off-axis locations. The result of this emission is that the majority of the emitted current falls onto the surface second anode, rather than going through the grounded anode aperture.

The "X" in the images of Figure 4.10 denotes the optical axis of the CFEG. The figure shows that emission is most likely occurring from multiple off-axis locations. The number of emission sites increased as the emission current was increased. During testing, the emission sites changed, real-time; evidence of a dynamically emitting system. Future research would entail a more thorough investigation of the effect of multiple off-axis protrusions emitting. The following sections pertain to simulations that were performed assuming a single protrusion. Even though, 4 protrusions could be defined (Figure 4.2 and Table 4.3) the results from the simulation of multiple protrusions were inaccurate, so the final simulation used a single on-axis protrusion. The total emission current can be calculated by integrating the single protrusion emission current across the entire emission region of the cathode.

Table 4.3 Approximated emission current (**Ic**) for a protrusion of height 3 μm and base diameter of 2 μm for different orientation angles (**φ**). This is for an accelerating voltage of -10 kV, an extraction voltage of -4 kV, a distance between the extractor and the cathode of 25 μm and a cathode tip diameter of 40 μm.

φ (degrees)	Ic (nA)
0	2500
9	0.0315
27	0.146
45	4E-12

The emission current falls off rapidly as the protrusion moves away from the optical axis (Table 4.3). For a protrusion current greater than a hundredth of the current produced by that protrusion on-axis, it has to be within 22 degrees of the optical axis. This gives a maximum emission region diameter of 14.5 μm. For within a thousandth, the maximum emission region diameter is 33.5 μm. This implies a good approximation of the maximum emission region diameter is half of the cathode tip diameter. Within this emission diameter, protrusions are emitting.

Another observation from changing the orientation of the protrusion was that protrusions of orientation angle (Figure 4.2) greater than five degrees do not significantly contribute to the current transmitted through the grounded anode. Also if two protrusions were too close to one another, the protrusions would negatively affect one another (Table 4.3) indicated by the results from a protrusion oriented at 9 degrees from the optical axis (since the on-axis protrusion was only ~1.5 μm away).

4.2 Electric Field Dependencies

From the Fowler-Nordhiem equation (Equation (2.1)), it is clear that the emission current has a strong dependence on the magnitude of the electric field [3, 4, 5]. Therefore,

the electric field at the area of emission, the protrusion emission region, and the emission current at that point was simulated as a function of distance between the cathode and the extractor, d, (Figure 4.3, Figure 4.11 and Figure 4.12). Figure 4.11 shows the electric field in the protrusion emission region as a function of the distance between the cathode and the extractor. Figure 4.12 shows the emission current at that point as a function of distance.

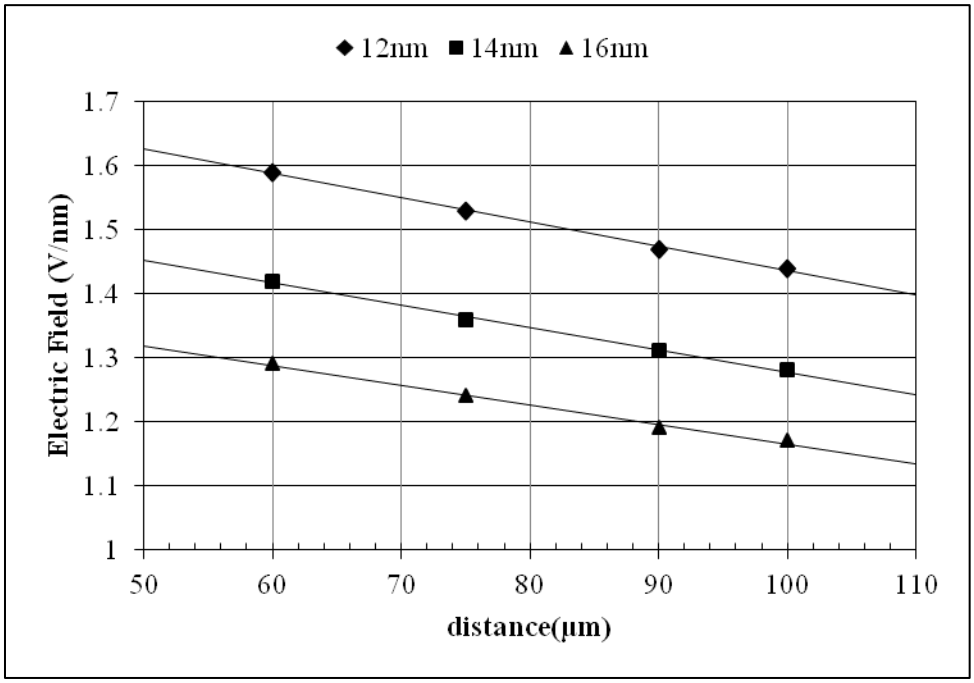

Figure 4.11 The electric field at the protrusion emission region as a function of distance between the cathode and the extractor (with linear fit) with protrusion emission region diameter, ED_p, of 12 nm, 14 nm and 16 nm. The protrusion diameter and height were 0.6 μm and 0.4 μm, respectively, and the cathode tip diameter was 4.0 μm.

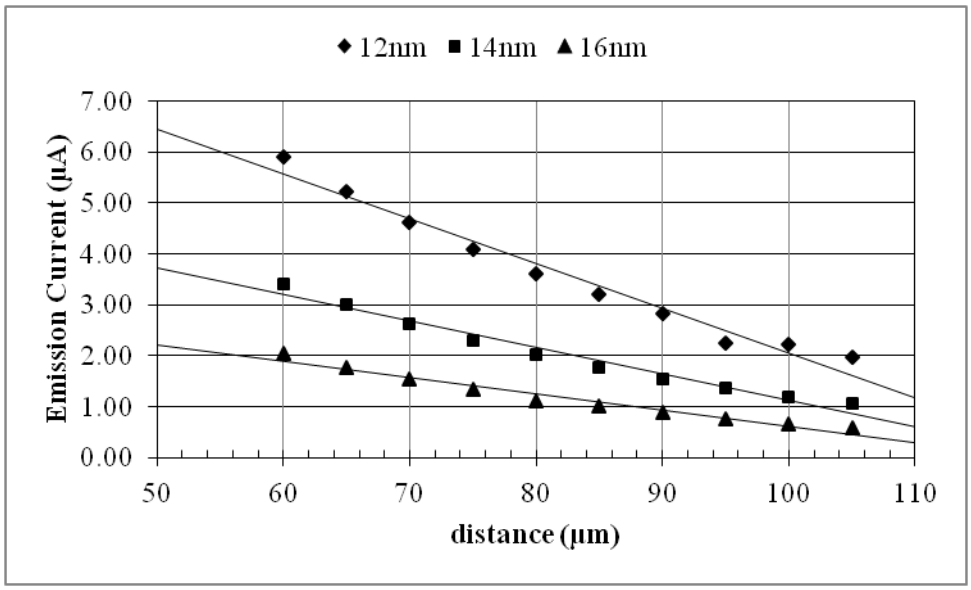

Figure 4.12 Emission current as a function of the distance from the cathode to extractor (with linear fit) for different protrusion emission region diameter, ED_p: 12 nm, 14 nm and 16 nm. The diameter of the simulated protrusion was 0.6 µm, the height of the protrusion was 0.4 µm and the tip diameter was set at 4.0 µm.

The electric field at the region of emission decreases as the protrusion emission region diameter increases (Figure 4.11), which suggested that the emission current at that point would be inversely proportional to the protrusion emission region diameter (discussed in Section 4.4). In addition, Figure 4.11 shows that the electric field at the protrusion emission region also decreased as the distance between the cathode and the extractor increases, confirming Equation (2.2), which stated that the electric field is inversely proportional to the distance between the cathode and the extractor. The emission current is also inversely proportional to the distance between the cathode and the extractor (Figure 4.12). Similar to the CFEG with the shaped-etched tip (ET CFEG), the emission current depends less on the shape of the tip of the cathode as the distance between the cathode and extractor increases. However, unlike the ET CFEG (which had an exponential fit with distance), the emission current seems to be linear with distance.

The current through the grounded anode was also simulated for the BT CFEG, showing a similar trend to that produced by the ET CFEG; the percentage was fairly insensitive to these distances. As was established in Chapter 3, this is due to two distinct reasons. 1.) The relative virtual source size is approximately the same for both tips, despite the protrusion emission region changing. (The equation for change in virtual size is given in Equation (3.1)), and 2.) The vignetting (as a result of geometry) is not affected by small changes in the cathode to extractor distances (Figure 3.8).

4.3 Extraction Voltage Dependencies

The Fowler-Nordhiem (Equation (2.1)) shows that the emission current depends on the electric field at the cathode [3, 4, 5]. This electric field is, in-turn, dependent on the extraction voltage, ΔV, and the geometry in the vicinity of the cathode, such as the size and shape of the cathode tip and the distance between the cathode and extractor (Equation (2.2)) [6, 7]. The extraction voltage is the voltage difference between the cathode and the extractor (Section 2.1). Equation (2.2) predicts that the electric field has a linear dependence on the extraction voltage. To confirm this, the electric field was simulated as a function of the extraction voltage (Figure 4.13). Since the electric field is linearly dependent on the extraction voltage, the emission current should also be dependent on the extraction voltage. The emission current was also simulated as a function of extraction voltages (Figure 4.14).

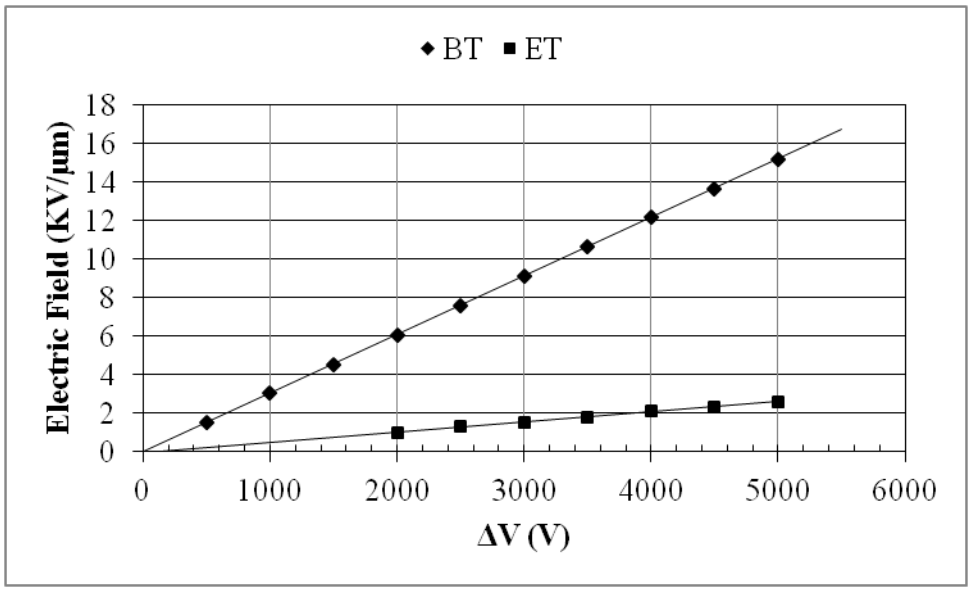

Figure 4.13 Electric field magnitude as a function of extraction voltage (with linear fit) for the cold field emission gun with the blunted tip cathode (BT) and shaped-etched tip (ET).

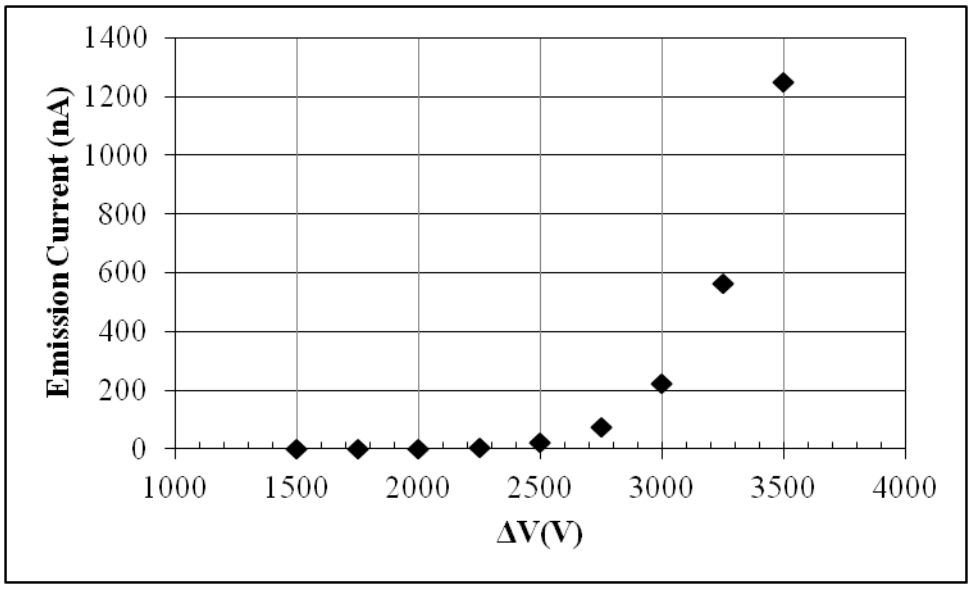

Figure 4.14 Simulated emission current as a function of the extraction voltage, ΔV, for an accelerating voltage, Vacc, of -4 kV.

The electric field is linear with the extraction voltage (Figure 4.13) as it was for the electron gun with the etched tip. In this instance, the local electric field was greater

for the BT than the ET because the BT has a protrusion(s) on the surface. Even though the local field for the BT can be greater than that of the ET, the presence of multiple protrusions results in a larger emission diameter and in unstable emission.

Figure 4.14 shows that the emission current is roughly exponential with extraction voltage. The same simulations were performed for several different accelerating voltages, and it was observed that the emission current was not affected by changes in the accelerating voltage.

The prototype was tested using a blunted tip. Figure 4.15 shows the extraction voltage as a function of the emission current for different accelerating voltages [1]. The prototype allows the user to input the desired emission current, and the voltage on the extractor is automatically adjusted to maintain this current.

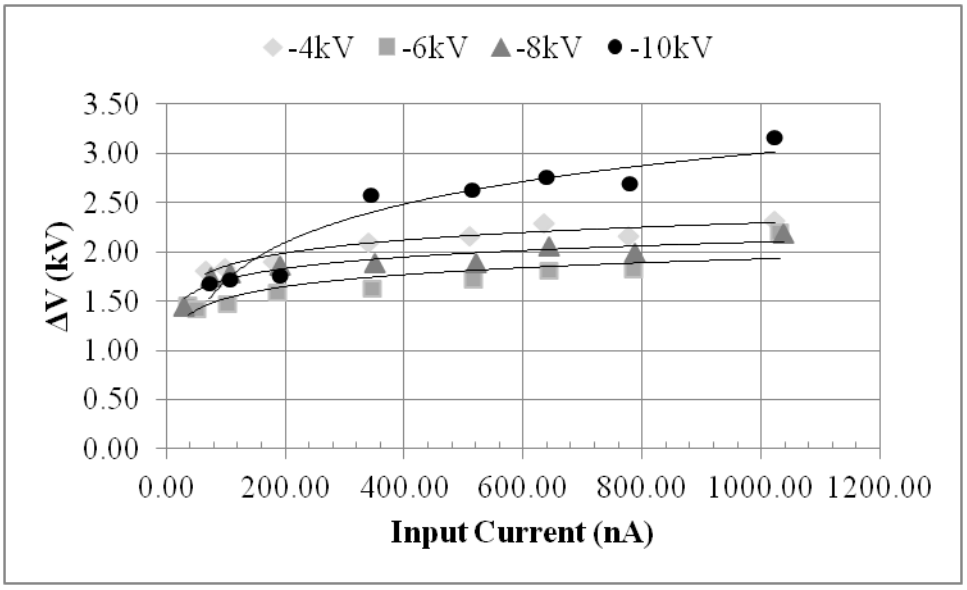

Figure 4.15 Extraction voltage as a function of the emission current for different accelerating voltages, Vacc of -4 kV, -6 kV, -8 kV and -10 kV [1] in the prototype.

Figure 4.15 shows that the emission current depends on the extraction voltage in a way similar to that shown in Figure 4.14. The experimental emission current changed with accelerating voltage where as the simulated emission current did not. Since the effect observed in the experimental data was not consistent over accelerating voltages (i.e., there does not seem to be a dependence between the emission current and accelerating voltage), it was determined to be due in part to the protrusions that were used to achieve emission.

4.4 Protrusion Emission Region Dependencies

The protrusion emission diameter (ED_p) is different from the emission region as defined in Figure 4.2. ED_p is the emission region confined to the flat-top of the protrusion on the surface of the BT and is defined in Figure 4.6. In Section 4.2, the electric field and emission current were described as roughly inversely proportional to this emission diameter. The emission current was simulated as a function of the protrusion emission diameter for different cathode-to-extractor distances and is inversely proportional to the protrusion emission diameter (Figure 4.16).

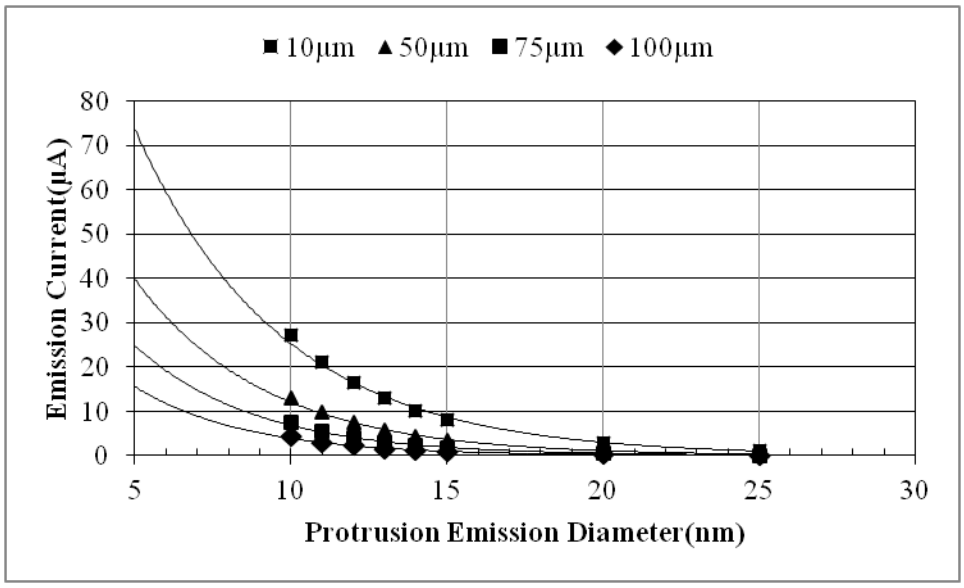

Figure 4.16 Emission current as a function of the diameter of the protrusion emission region (with exponential fit) for distances between extractor and cathode of 10 µm, 50 µm, 75 µm and 100 µm. The diameter of the simulated protrusion was 0.6 µm, the height of the protrusion was 0.4 µm and the diameter of the cathode tip was set at 40 µm.

Varying the protrusion emission diameter (which changes the geometry of the protrusion) will influence the current through the grounded anode. To isolate the effects of the changes in geometry, the percentage of the emission current transmitted through the grounded anode was simulated (Figure 4.17).

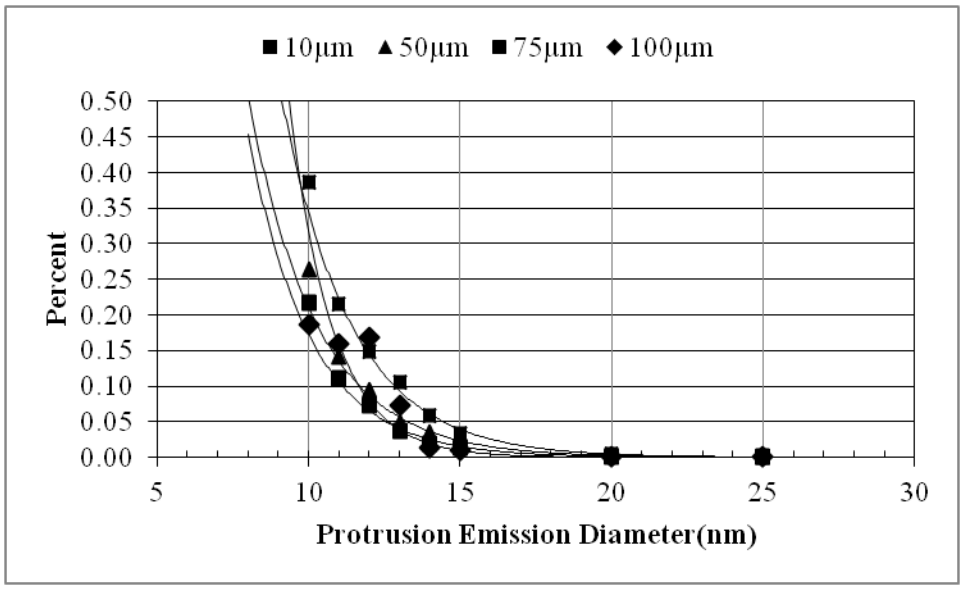

Figure 4.17 Percentage of the emission current through the grounded anode as a function of the diameter of the protrusion emission region (with exponential fit) for the distance of 10 µm, 50 µm, 75 µm and 100 µm between extractor and cathode.

In a very similar trend to that produced by the ET CFEG, the percentage of the emission current through the grounded anode is inversely proportional to the protrusion emission diameter (Figure 4.17). This is a result of smaller protrusion emission regions reducing the angle into which the electrons are emitted (Figure 3.12).

These simulations were done assuming a single protrusion emitting. However, it is predicted that multiple protrusions emit at the same time; which would affect the overall emission current and percentage through the grounded anode.

4.5 Cathode Diameter Dependencies

The cathode tip diameter (CD), defined in Figure 4.2, for the BT is dependent on how much blunting (i.e. breaking and melting) has occurred (Figure 4.1). The emission current was simulated as a function of the cathode tip diameter (Figure 4.18). The

diameter of the simulated protrusion was 0.6 µm, the height of the protrusion was 0.4 µm and the protrusion emission diameter, ED_p, was set at 12 nm.

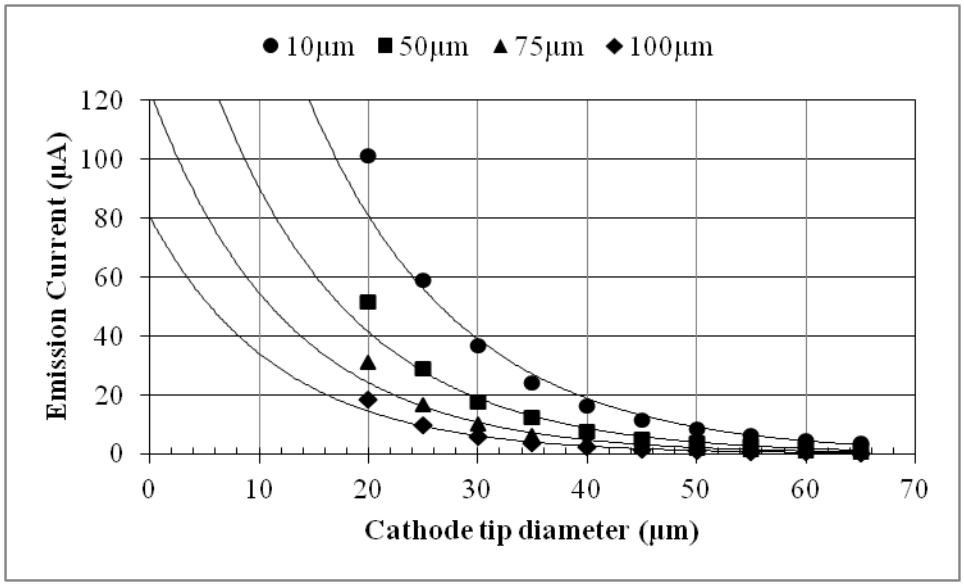

Figure 4.18 Emission current as a function of the cathode tip diameter (with exponential fit) for distances between the cathode and extractor of 10 µm, 50 µm, 75 µm and 100 µm.

The emission current decreases inversely with the cathode diameter (Figure 4.18). This was also observed in the results of the ET CFEG simulation. The decrease in the cathode tip diameter coincides with an increase in the electric field at the tip, which increases the emission current. To observe any vignetting effects, the percentage of emission current through the grounded anode was calculated (Figure 4.19).

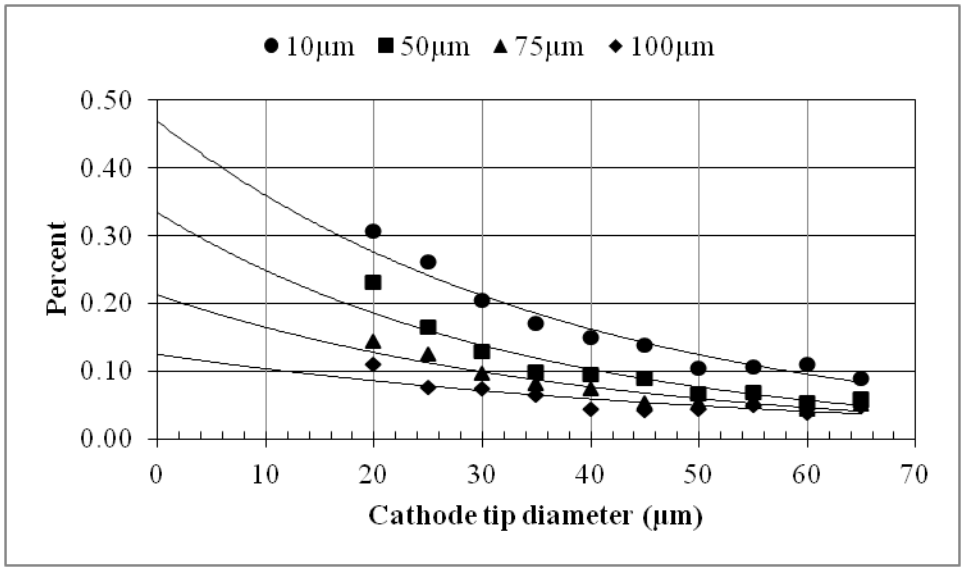

Figure 4.19 Percentage of emission current through the grounded anode as a function of the cathode tip diameter for distances between the cathode and extractor of 10 µm, 50 µm, 75 µm and 100 µm with exponential fits.

Increasing the diameter of the tip causes the percentage of current through the grounded anode to decrease (Figure 4.19) which is somewhat different from the result of the ET CFEG. The percentage of emission current through the anode increased with cathode tip diameter. This is again due to vast differences in shapes of the two cathodes. One has a finely etched tip with a shape situated on the end and the other where the tip had been broken off with multiple protrusions on the surface emitting.

4.6 Conclusions

Unstable emission, sometimes occurring off-axis, limits the blunted tip cathode's use, making it unsuitable for use in the lunar mini-SEM; however, the blunted tip cathode's durability allowed the CFEG's custom control system to be tested without the concern of breaking off of an expensive etched tip and required less stringent vacuum conditions for operation. The idealized current emitted, current through the grounded

anode, and current terminating on the surface of the grounded anode with the distance between the extractor and the grounded anode at 10 mm were calculated using geometrical principles and the Fowler-Nordhiem equation (Equation (2.1)) and are listed in Table 3.3.

Table 4.4 Idealized emission current, current through the grounded anode and current on the grounded anode for different distance between cathode and extractor (d) for the CFEG with blunted tip. The accelerating voltage was -10 kV. The extraction voltage was set at 3.5 kV and the emission cone half angle to 45 degrees. Emission region diameter was assumed to be 0.9 μm.

d(μm)	Emission current (μA)	Current through grounded anode (μA)	Current on grounded anode (μA)
50	10.40	0.13	10.27
100	5.20	0.065	5.14
150	3.47	0.043	2.47
200	2.60	0.032	1.44

Through this research, the following was determined:

- The electric field was shown to be inversely dependent on the distance between the cathode and the extractor, and directly dependent on the extraction voltage as predicted by Equation (2.2).
- Electric field was also shown to be inversely dependent on the protrusion emission diameter.
- The local electric field at a given protrusion may be higher than that of an etched tip, but the emission is highly unstable, and because of the presence of multiple emission sites, the protrusion emission diameter can be very large
- The emission current was shown to decrease with protrusion emission region diameter, cathode tip diameter, and distance.

- The percentage of the emission current transmitted through the grounded anode decreases exponentially with protrusion emission region diameter and cathode tip diameter, and is independent on the distance between the cathode and the extractor.
- The protrusion(s) (which assist the emission by increasing the electric field in the protrusion emission region) was simulated as a single on-axis flat-topped cone. This flat-topped cone was controlled by three variables, the protrusion emission diameter, the height, and the diameter of the base.
- The emission current increased with increased protrusion height and decreased diameter of both the protrusion emission region and the base of the protrusion.

It is interesting to note that only small changes occurred in the emission current through the grounded anode for different protrusion heights, but large changes occurred in the emission current when the protrusion height changed. Also, an increase in the radius of the base of the protrusion caused an increase in the amount of emission current through the grounded anode.

CHAPTER V

THERMIONIC EMISSION GUN

5.1. Simulation Definition

Simulations of the thermionic emission gun (TEG) were performed to determine the expected emission current produced by different geometric configurations of the electron gun. (Thermionic emission needs and requirements are discussed in Section 2.2.) The cathode used for thermionic emission is typically a hairpin filament (Figure 2.14) [1]. The TEG in this research used a hairpin filament with a fine tungsten tip welded on the end (Section 2.2.2) [2]. This fine tip results in decreased optical power (over that of a standard hairpin filament) necessary to achieve a small spot size at the sample [1, 2].

Typically, the cathode is set to a high voltage (up to 10 kV) and high temperature to emit electrons. A Wehnelt cylinder is set at a particular negative potential to control the emission. (The purpose and physics of the Wehnelt cylinder is discussed in Section 2.2.1 [1, 3].) As with the CFEG, the anode was grounded, and the emitted electrons were accelerated by the potential difference between the cathode and the grounded anode, called the accelerating voltage.

The simulations of the TEG were done using the CPO2DS software [4]. Table 5.1 lists the values used in the TEG simulation and the resulting emission current and current through the grounded anode. Figure 5.1 shows the cathode and Wehnelt cylinder with the distance between them labeled. Figure 5.2 shows a sketch corresponding to the thermionic electron gun simulation (including cathode, Wehnelt cylinder and grounded anode).

Table 5.1 Values used to simulate the TEG and the resulting emission currents [4].

	TEG
Cathode tip diameter (μm)	0.1
Distance from cathode to Wehnelt cylinder (μm)	100
Emission region diameter (μm)	0.1
Wehnelt cylinder aperture diameter (μm)	300
Grounded anode aperture diameter (μm)	200
Distance from Wehnelt cylinder to grounded anode (mm)	10
Emission current (μA)	9.9
Current through the grounded anode (μA)	9.9

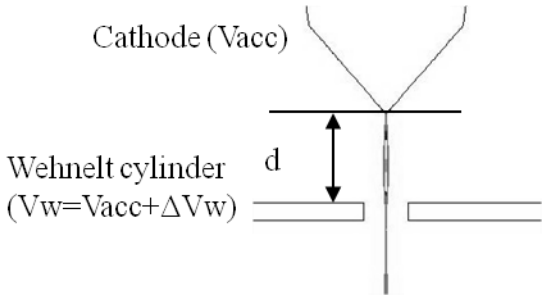

Figure 5.1 Cathode and Wehnelt cylinder of Thermionic electron gun with distance between labeled [4]. The cathode is at the accelerating voltage, Vacc, and the Wehnelt cylinder is a few volts more negative than the accelerating voltage to allow the Wehnelt cylinder to control the electron beam [1, 3]. A result of the negative difference between the cathode and Wehnelt cylinder is that the Wehnelt cylinder focuses the electron beam to increase the amount of current through the grounded anode [1, 3].

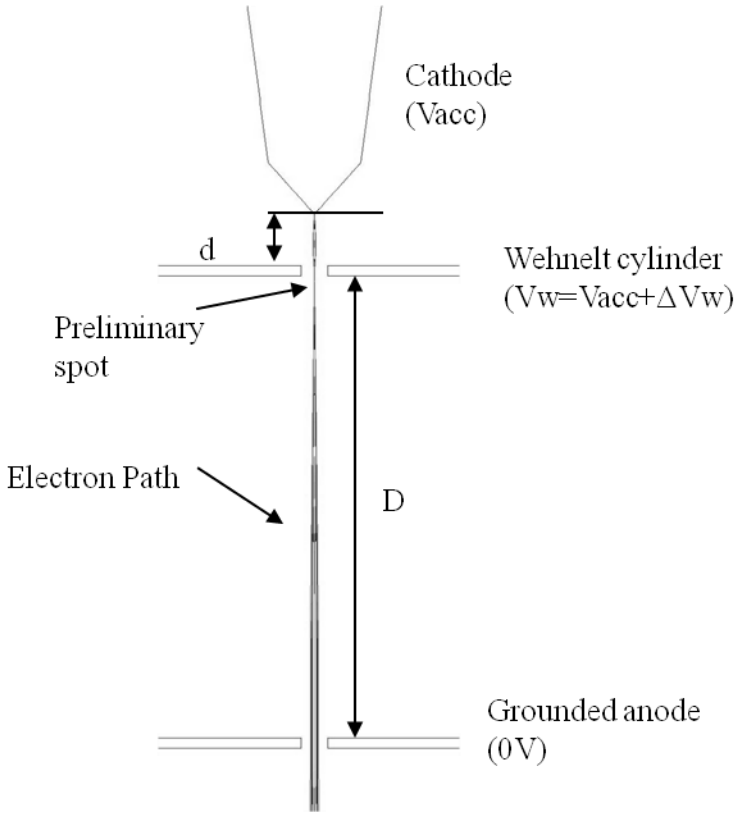

Figure 5.2 Simulation of the thermionic electron gun in CPO2DS [4]. The cathode is at a high enough temperature to assist the electrons in overcoming the work function of the tungsten filament. The Wehnelt cylinder suppresses or passes current depending on its bias referenced to the cathode and focuses the electrons inside the gun. D is the distance between the Wehnelt cylinder and the grounded anode and d is the distance between the cathode and the Wehnelt cylinder.

5.2. Temperature Dependencies

The Richard-Dushman equation (Equation (2.3)) shows that the emission current has a strong dependence on temperature of the cathode [1, 3, 5, 6, 7]. Discussed in Section 2.2, the high temperature of the cathode is achieved by passing a current through the filament. The emission current was determined as a function of temperature using the simulation and compared with the current predicted by the Richard-Dushman equation

(Figure 5.3) [1, 3, 5, 6, 7]. The emission current as a function of temperature of were estimated for the filament with (0.1 μm and 0.2 μm) the fine tip attached and without (30 μm).

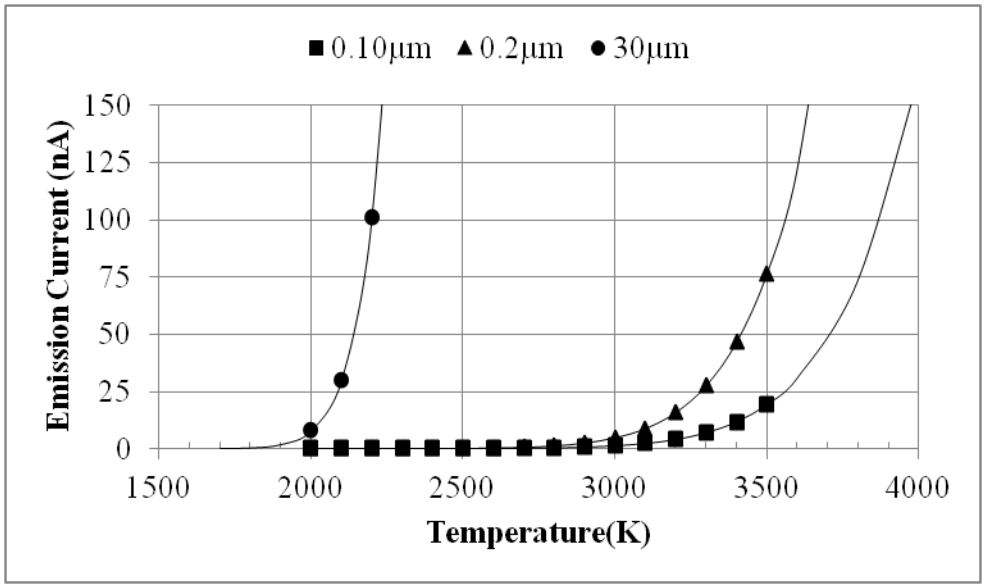

Figure 5.3 Emission current as a function of temperature (fit was Richard-Dushman equation) for emission diameters of 0.10 μm, 0.20 μm and 30 μm. The values of the emission region were estimated for the filament with (~100 nm) and without (~30 μm) the fine tungsten tip. The cathode tip diameter is equal to the emission region diameter.

The simulations showed that the emission current increased as a function of temperature (Figure 5.3) as predicted by the Richard-Dushman equation. The emission current also increased with emission region diameter, as expected. The emission current was much higher for the hairpin filament without the fine tungsten tip welded on (the emission region diameter of 30 μm); however, this much larger spot requires a significantly greater amount of optical power to decrease the size of the spot on the surface of the sample and decreases the achievable resolution.

5.3. Cathode tip Diameter Dependencies

For the TEG, the entire cathode tip emits. The emission current for the TEG increases with emission diameter (the cathode tip diameter). To further investigate this, the emission current was simulated as a function of the cathode tip diameter for different temperatures relevant to tungsten (Figure 5.4).

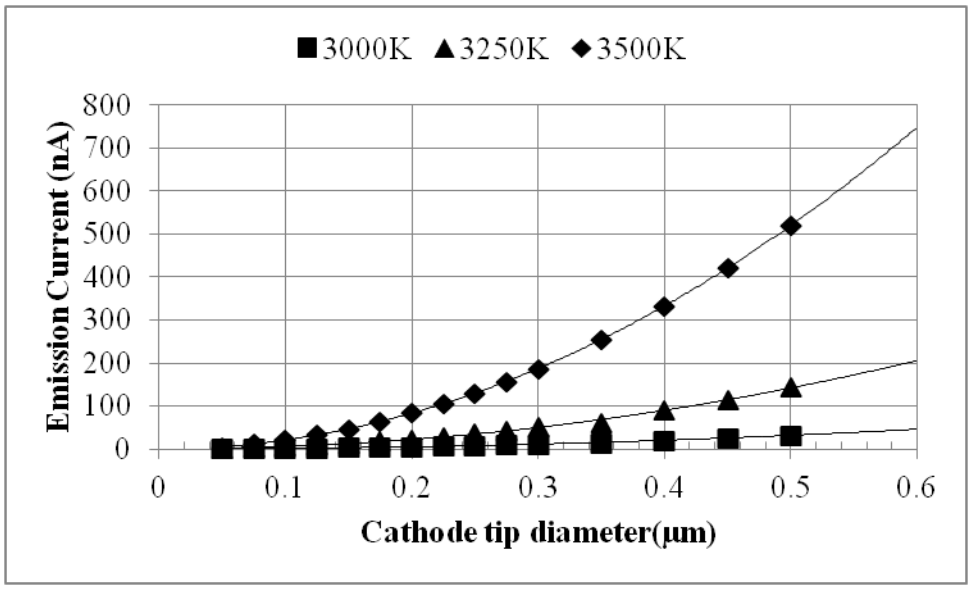

Figure 5.4 Emission current as a function of the cathode tip diameter (quadratic fit) for cathode temperatures of 3000 K, 3250 K and 3500 K.

Figure 5.4 shows that the emission current increases with emission diameter, quadratically. This would indicate that the emission current is directly dependent on the area of the emission, as expected. The same simulations were done for the percentage of current through the grounded anode. Figure 5.5 shows the percentage of emission current through the grounded anode as a function of emission diameter.

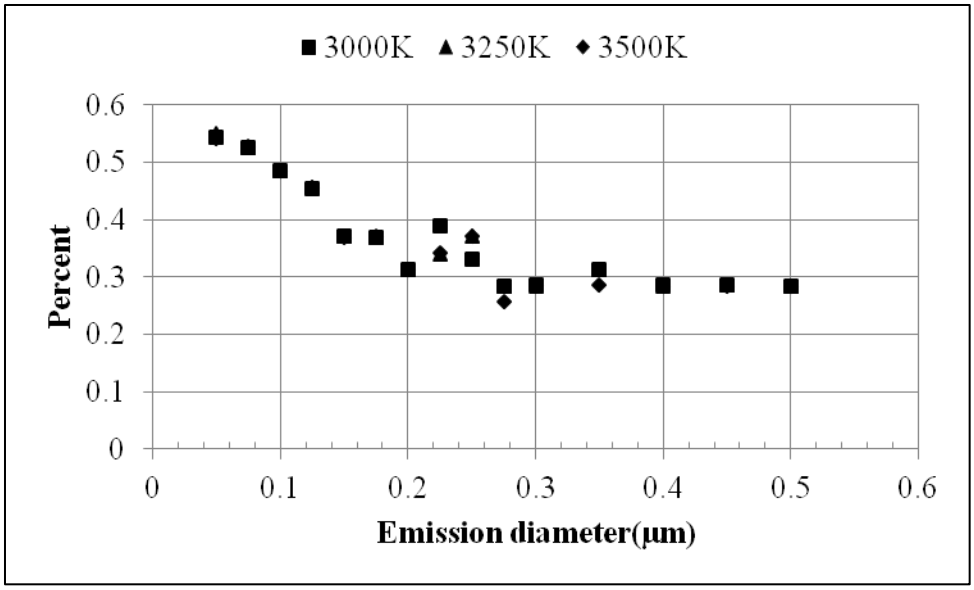

Figure 5.5 Percentage of emission current through the grounded anode as a function of the emission diameter (with a linear fit) for cathode temperatures of 3000 K, 3250 K and 3500 K. The percentage of emission current through the grounded anode was insensitive to the changes in temperatures. These simulations were run with the cathode tip diameter set to 1 μm.

The emission current that is transmitted through the grounded anode changes slowly with the emission diameter for the TEG (Figure 5.5).

5.4. Wehnelt Cylinder

The Wehnelt cylinder controls the current produced by the TEG by focusing the electron beam and affecting the electric field on the surface of the cathode (Section 2.2.1) [1, 3, 5]. When the Wehnelt cylinder is unbiased, a large percentage of the emitted electrons terminate on the surface of the grounded anode and are not available to the electron column (due to spreading of the electron beam). When the Wehnelt cylinder is biased, approximately the same amount of emission current is produced by the cathode; however, the emission current through the grounded anode is greater because the electron beam is focused and passes through the grounded anode. However, if the Wehnelt

cylinder is over-biased, the Wehnelt cylinder will suppress the emission. The emission current was determined as a function of this bias to confirm this assumption (Figure 2.11).

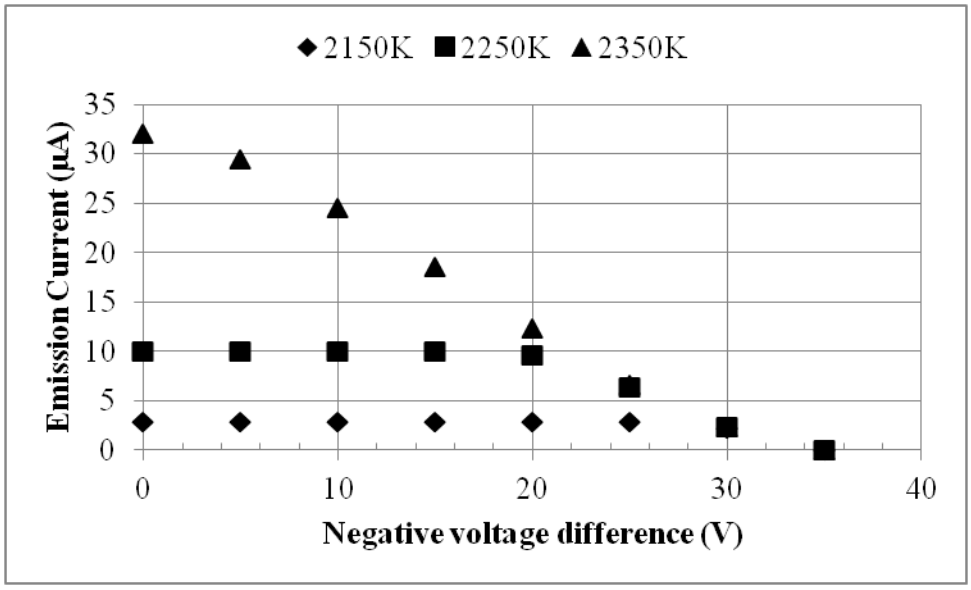

Figure 5.6 Emission current as a function of the voltage difference (ΔVw) between the cathode and Wehnelt cylinder, for a cathode to Wehnelt cylinder distance of 50 μm, for cathode temperatures of 2150 K, 2250 K and 2350 K

As expected, the emission current was higher for smaller voltage differences (Figure 2.11). For lower temperatures, the emission current was less sensitive to the changes in the voltage difference between Wehnelt cylinder and the cathode (Figure 2.11).

The Wehnelt cylinder affects the electric field on the surface of the cathode. Therefore, changes in distance between the cathode and the Wehnelt cylinder (d) should also affect the emission current. To determine the effect of the distance between the cathode and the Wehnelt cylinder, the emission current was simulated as a function of the

voltage difference for different distances between cathode and Wehnelt cylinder (Figure 5.7).

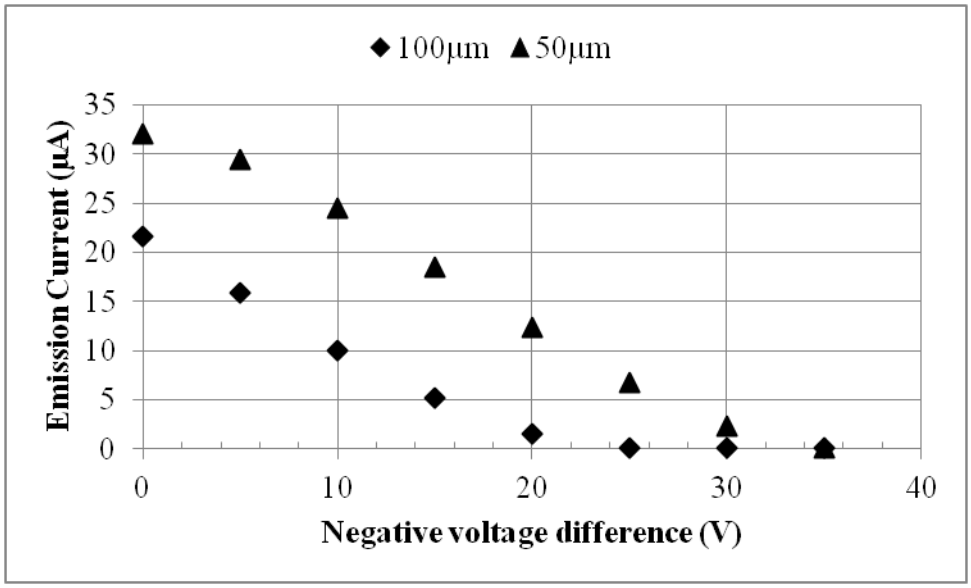

Figure 5.7 Emission current as a function of the voltage difference for cathode-to-Wehnelt cylinder distance of 100 µm and 50 µm for a cathode temperature of 2250 K.

In general, the emission current is inversely proportional to distance between the cathode and the Wehnelt cylinder (Figure 5.7). In both of the cases represented in Figure 5.7, as the voltage difference increased, the emission current decreased. Also observed in Figure 5.7, the greater the distance between the cathode and the Wehnelt cylinder, the more the emission current is suppressed, which verifies the assumption that the Wehnelt cylinder affects the electric field on the surface of the cathode.

5.5. Experimental Results

The figures below show the experimental results from the TEG prototype with a Faraday cup placed just after the grounded anode. The filament current is the current

through the cathode and controls the temperature of the cathode. The current in the Faraday cup was measured as a function of this filament current (Figure 5.8).

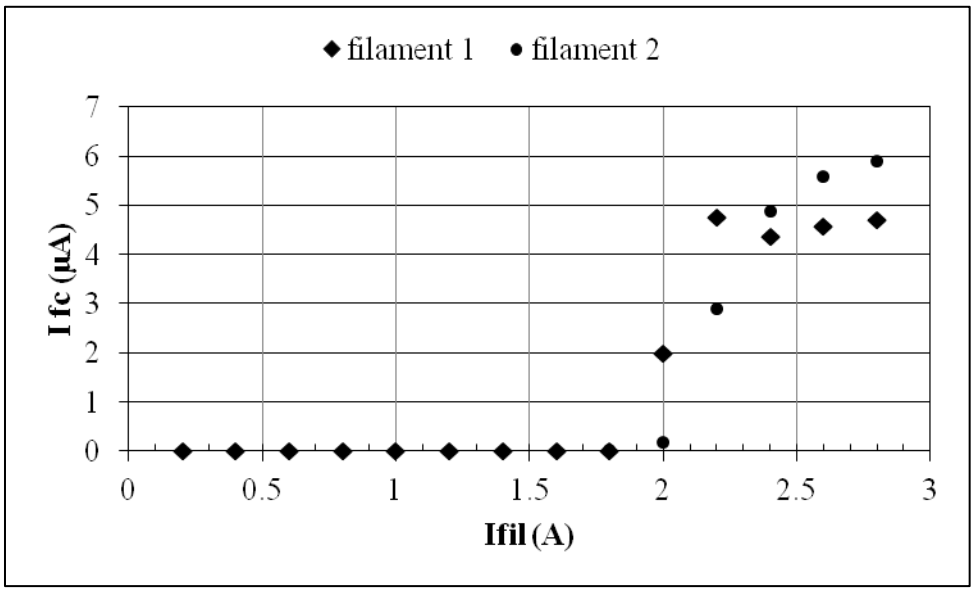

Figure 5.8 Current in the Faraday cup (Ifc) as a function of the filament current (Ifil) for the two different filaments used in the prototype. The filament current controls the temperature of the cathode.

Figure 5.8 shows that there is a minimum filament current (i.e., a minimum temperature on the cathode) needed for emission, also observed in previous research [3, 7]. When the emission current levels off, the current is said to be saturated (Figure 5.8). The location of the saturation point (the desired operating temperature) depends on the bias of the resistor [7]. Figure 5.8 indicates that just before saturation was achieved, the current produced, as measured by the Faraday cup, increased with the filament current and then leveled off as predicted in Section 2.2. If the operator uses a higher temperature than necessary, the lifetime of the filament decreases considerably [1, 3, 7]. An experimental dependency on the filament current, which is observed when the filament current is below the saturation current, was predicted using simulations (Figure 5.3).

An autobias resistor controls the voltage difference between the cathode and the Wehnelt cylinder (Section 2.2.1) [1, 3]. This voltage difference (discussed in Section 5.4 and Section 2.2.1) affects the current emitted by the cathode and the percentage of the emission current through the grounded anode. The emission current was measured as a function of an uncalibrated bias control setting (Figure 5.9). The voltage difference range for the bias control setting was 0 to 8 V.

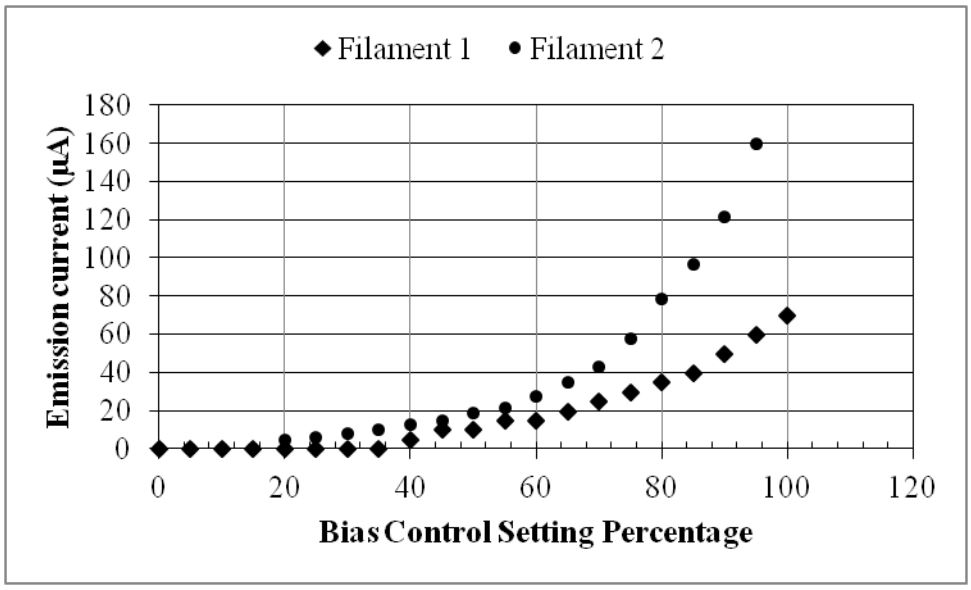

Figure 5.9 The emission current as a function of the percentage of the bias control setting for the two filaments used in the prototype. The bias control controls the variable resistor that controls the voltage difference between the cathode and the Wehnelt cylinder.

The bias control setting changes the bias on the resistor shown in Figure 2.12 (discussed in Section 2.2.1) [1, 3]. The emission current increases with the bias control setting (Figure 5.9). Therefore, this setting affects the voltage difference between the cathode and Wehnelt cylinder. As the voltage difference becomes more negative, the emission current decreases. If the voltage difference continues to increase beyond a few volts, the emission current will be suppressed (Figure 2.11 and Figure 5.7).

The accelerating voltage is the voltage difference between the cathode and the grounded anode and determines the energy of the electrons being emitted. Electrons of greater energy will diverge less from the original path and will more easily overcome the work function. The current detected by the Faraday cup and the emission current was measured as a function of the accelerating voltage (Figure 5.10).

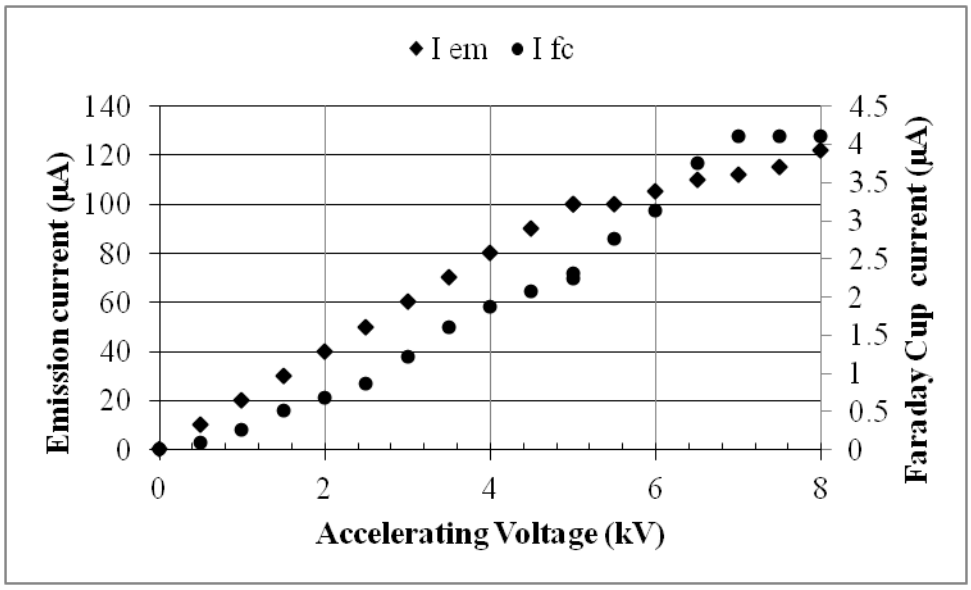

Figure 5.10 The current detected in the Faraday cup (I fc) and the emission current (I em) as a function of the accelerating voltage for constant voltage difference between the cathode and Wehnelt cylinder is shown

The emission current (and brightness) increases with the accelerating voltage (Figure 5.10). This relation can be explained with an examination into the effect of higher accelerating voltages [1, 3, 5]. Electrons with higher accelerating voltages have a higher kinetic energy. Therefore, as in the CFEG, the effective work function is easier to overcome. In a thermionic emitter, the potential barrier is further lowered by heating the filament.

The current detected in the Faraday cup increases with accelerating voltage (Figure 5.10) because the emission current increases (therefore, more current is available to pass into the Faraday cup) and a higher percentage of the electrons are transmitted into the Faraday cup because they scatter (diverge) less at higher accelerating voltages.

5.6. Conclusions

The robust nature, less stringent vacuum conditions, low cost and well-understood operation of the thermionic electron gun make it an ideal tool for testing the lunar mini-SEM electron focusing column, independent of the cold field emission gun.

Through this research the following was determined:

- The emission current was observed to exponentially depend on filament temperature during testing of the prototype and in the simulations.
- The emission current was shown to vary quadratically with respect to the emission region diameter (which was equivalent to the cathode tip diameter). Indicating that the emission current is directly proportional to the emission area.
- The percentage of emission current through the grounded anode was shown to be independent of the filament temperature.
- The percentage of emission current through the grounded anode was shown to decrease with emission region diameter.
- The Wehnelt cylinder control of the emission current and current through the grounded anode was confirmed by testing of the prototype and through the simulations.

From these results, the optimal values for the various parameters investigated were determined (Table 3.5). These values are based on simulation results and on the geometric restrictions of the lunar mini-SEM mechanical design and the requirement that the current at the sample be no less than 1 nA (more than sufficient for imaging and x-ray analysis) [3].

Table 5.2 Settings for optimal cathode tip diameter, Wehnelt cylinder to cathode distance, and Wehnelt cylinder to anode distance and the predicted emission current and current through the grounded anode for the thermionic electron gun (TEG). These values were chosen to achieve at least 1 nA of current at the sample.

	TEG
Cathode tip Diameter (μm)	0.1-0.15
Bias Voltage (V)	5-8
Temperature (K)	3000
Cathode to Wehnelt Cylinder Distance (μm)	75
Wehnelt Cylinder to Grounded Anode Distance (mm)	10
Minimum Emission Current (nA)	100
Minimum Current through Grounded Anode (nA)	30

To maximize the current at the sample and the filament's lifetime, the temperature just after the saturation should be used, and the Wehnelt cylinder voltage should be only a few volts more negative than the cathode. The extractor to grounded anode distance has been chosen to minimize the dispersion angle, which results in minimal spherical aberration while maintaining reasonable current through the grounded anode.

CHAPTER VI

ELECTRON FOCUSING COLUMN

6.1 Introduction

Simulations were performed to determine the effectiveness of the lunar mini-SEM's electron focusing column, to examine the geometric configuration and to optimize it.

The purpose of an electron focusing column is to focus the electron beam, generated by the electron gun, to a spot on the sample surface in such a way as to achieve high resolution while maintaining adequate current at the sample for analysis. The electron focusing column used in this research is a proprietary design and consists of several beam-limiting apertures and an electrostatic lens, which is analogous (as its name implies) to an optic lens. The electrostatic lens used in this research was an Einzel lens. Einzel lenses contain three apertures typically referred to as: first Einzel, second Einzel, and third Einzel. All of the apertures in the electron focusing column are grounded except the second Einzel, which is set to a focusing voltage, V_f [1].

Figure 6.1 depicts the thermionic electron gun (TEG) with the electron focusing column. In this gun, the cathode, Wehnelt cylinder and anode produce a somewhat collimated beam of electrons (as discussed in Chapter 5). The apertures in the electron

focusing column further limit the size of the spot, and the Einzel lens focuses the electron beam onto the focal plane. A scanning system is attached to the end of this electron focusing column, which rasters the electron beam in a controlled fashion for subsequent imaging and x-ray analysis.

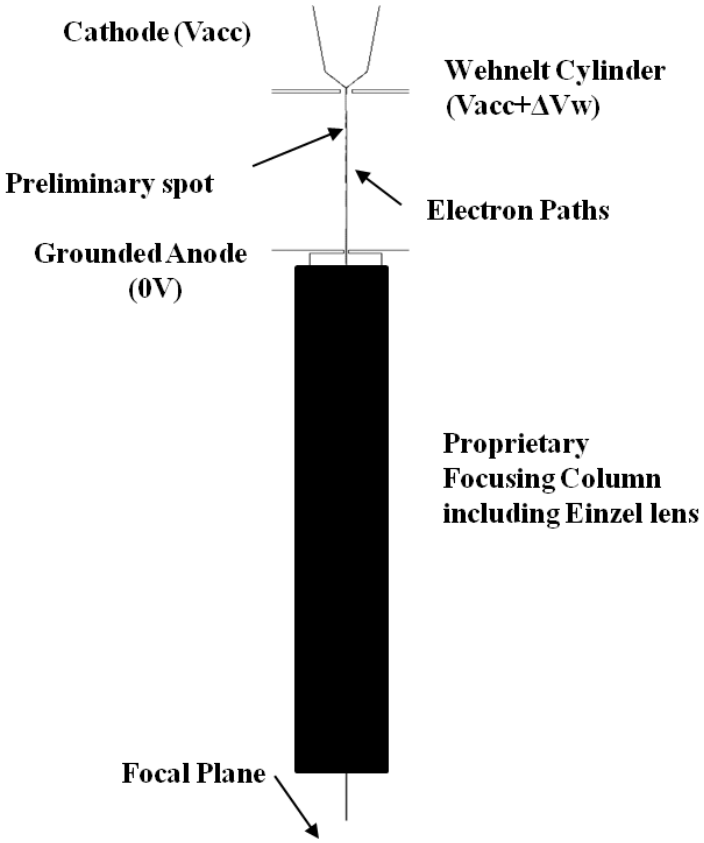

Figure 6.1 An image of the simulation of the TEG with column is shown [2]. The cathode, Wehnelt cylinder and grounded anode are the primary components of the electron gun, which produces an electron beam. The apertures in the electron focusing column limits the electron beam which the Einzel lens focuses. The scanning system follows the electron focusing column and scans the focused electron beam across the sample.

In Figure 6.1, the spread of the electron beam is limited by carefully placed apertures in the electron focusing column and by the grounded anode in the gun. In this

research, simulations were carried out for each, previously discussed, electron gun configuration (the ET CFEG, discussed in Chapter 3, the BT CFEG, Chapter 4, or the TEG, Chapter 5) attached to the lunar mini-electron focusing column. The simulation conditions for each electron gun are summarized in Table 3.1.

Table 6.1 Values used to simulate the CFEG with the shaped etched tip (ET) and the blunted tip (BT) and the thermionic electron gun (TEG) and the resulting emission current and current through the grounded anode [2].

	ET	**BT**	**TEG**
Cathode tip diameter (μm)	0.9	40	0.1
Distance from cathode to extractor (or Wehnelt cylinder) (μm)	50	50	100
Emission region diameter (μm)	0.45	20	0.1
Extractor (or Wehnelt cylinder) aperture diameter (μm)	200	200	300
Grounded anode aperture diameter (μm)	500	500	500
Distance from extractor (or Wehnelt cylinder) to grounded anode (mm)	10	10	10

To date, the electron focusing column has only been tested with the TEG. The advantage of testing the electron focusing column with an off-the-shelf thermionic electron gun, rather than with the custom CFEG that is being developed, is that the filaments are inexpensive, have a short lead-time when ordering replacements, are robust (i.e., are difficult to damage), their operation is well understood, and their less stringent vacuum requirements allows for prototype modification to be made in a fairly short amount of time. Table 6.2 gives the simulated emission current for each of the electron guns, current through the grounded anode (the current that makes it into the electron

focusing column), and the current at the focal plane. These simulations assume perfect alignment of apertures and perfect alignment of the electron gun to the focusing column.

Table 6.2 Emission current (I_c), current through the grounded anode (I_a) and current measured at the focal plane (I_f) for the etched tip electron gun (ET CFEG), the blunted tip electron gun (BT CFEG) and the thermionic electron gun (TEG) with the column attached under the conditions discussed in previous chapters for each of the electron guns (Table 6.1).

	I_c (μA)	I_a(nA)	I_f(nA)
ET CFEG	1.27	14.2	1.43
BT CFEG	1.02	6.73	0.06
TEG	0.073	73.2	62.7

Table 6.2 shows that most of the electrons generated in the electron guns are stopped by the grounded anode (in the gun) and by the apertures in the electron focusing column. The BT CFEG is the only electron gun with the electron focusing column that does not meet the criteria for imaging (1 pA for imaging and 1 nA for x-ray analysis); however, the BT was used solely to test the capabilities and components of the system used to control and monitor the CFEG rather than as a possible cathode for use in the lunar mini-SEM [3].

6.2 Electrostatic Lens

There are two major types of electron lenses: magnetic and electrostatic. Electron lenses use the Lorentzian force to focus a beam of electrons shown in the following equation [1, 3]:

$$\mathbf{F} = \mathbf{e}(\mathbf{E} + \mathbf{v} \times \mathbf{B}), \tag{6.1}$$

where F is the Lorentzian force on an electron of charge, e, and velocity, v, and E and B are the electric and magnetic fields produced by the electron lens. Magnetic lenses focus an electron beam with a magnetic field which is generated as current is passed through wire coils. Electrostatic lenses focus an electron beam through a strong electric field, generated by applying a particular voltage to a carefully designed lens (in our case, cylindrical in nature). This electric field causes the electrons' paths to bend much like a change in the index of refraction causes the path of light to bend. The electric field inside the electron lens, E, is given by [1, 3]

$$\mathbf{E} = -\nabla \mathbf{V}. \tag{6.2}$$

The magnetic field is zero for electrostatic lenses; therefore, the force (F) on the electrons is [1, 3]

$$\mathbf{F} = -\mathbf{e} * \nabla \mathbf{V}. \tag{6.3}$$

A simulation of an electrostatic focusing lens is shown in Figure 6.2. The electron beam is focused by the electric field that is produced by applying a voltage to the cylindrical lens.

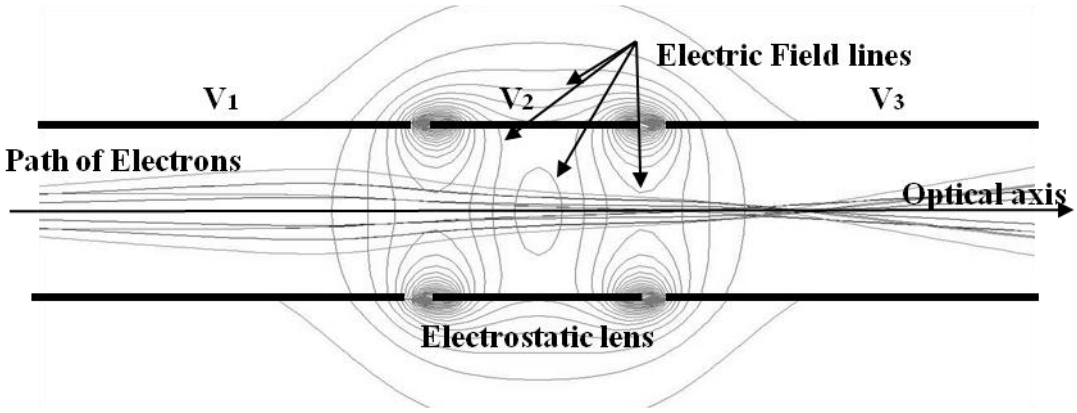

Figure 6.2 Path of electrons through a cylindrical electrostatic lens with the voltages labeled on the electrodes. For an Einzel lens, V_1 and V_3 are at ground and V_2 is at V_f, the focusing voltage [1, 3].

The different types of electrostatic lenses include aperture (or immersion) lenses and cylinder lenses [1]. Aperture lenses are so called because the lens effect is caused by the electron beam traveling through a cylinder of one voltage to a cylinder of another voltage with an aperture in between. Cylinder lenses have an applied potential that is constant along the optical axis [1]. Figure 6.2 provides an example of a cylinder lens where the potential is on the second Einzel.

The electrostatic lens used in this research was an Einzel lens. Einzel lenses are a special type of cylinder lens and contain three apertures or cylinders (Figure 6.3). The purpose of these three apertures is to focus the electron beam without changing the energy of the electrons propagating through it. This is achieved by grounding the first and third Einzels and applying a focusing voltage to the second Einzel [1]. This produces no net acceleration on the beam of electrons passing through.

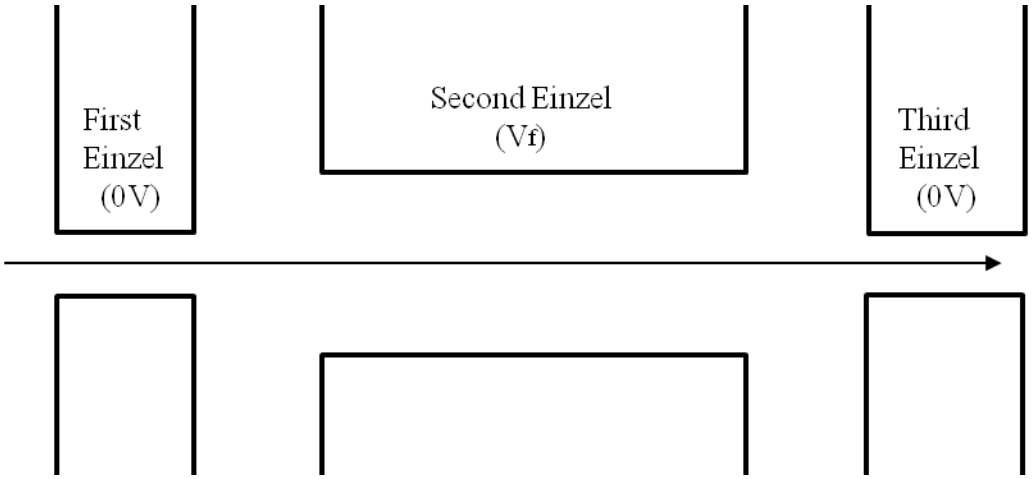

Figure 6.3 Schematic of an Einzel lens with the applied potentials. The first and third Einzel are at ground and the second Einzel is at the focusing voltage (V_f). This produces no net acceleration on the beam of electrons passing through the lens. (This figure is modified from Hawkes and Kasper [1].)

6.3 Focusing Voltage Dependence: Distance to the Focal Plane

A focusing voltage is applied to the second aperture in the Einzel lens. The focusing voltage controls the optical power of the electron lens; and therefore, sets the distance between the last component in the column and the focal plane (i.e. the working distance).

The working distance was determined for different simulated focusing voltages, positive and negative (Figure 6.4). The lunar mini-SEM electron focusing column was designed for a negative focusing voltage, which allows for a lower voltage to be used; however, both the positive and negative focusing voltages were simulated and used during testing of the mini-electron focusing column. For lenses with greater optical power, the working distance should be shorter than for lenses with a lower optical power. A more detailed examination of the working distance can be found in Section 7.2.

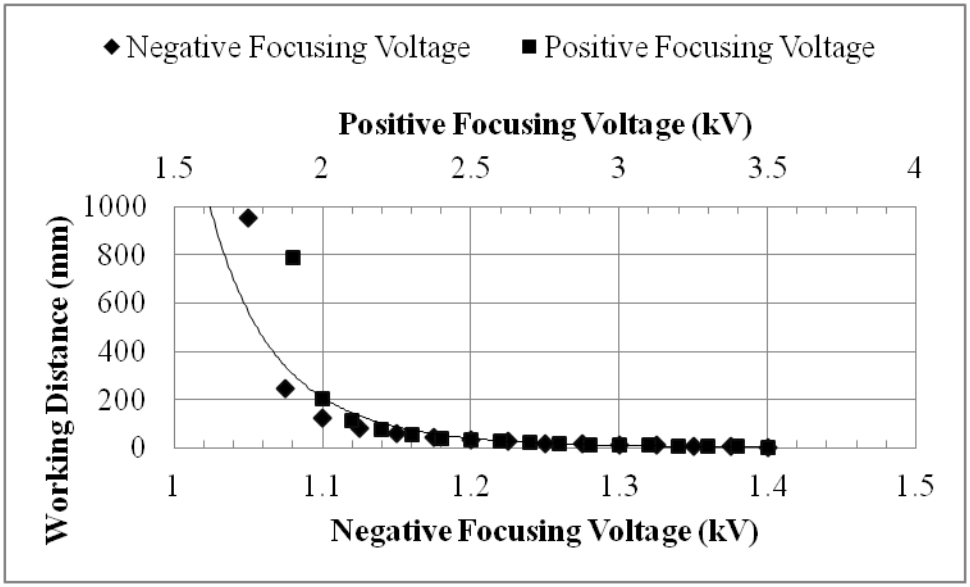

Figure 6.4 The working distance (distance to the focal plane) as a function of the positive and negative focusing voltage, for the thermionic electron gun (TEG) with electron focusing column, with accelerating voltage -2 kV. The decay is predicted from the understanding that stronger lenses have shorter focal lengths. The cold field emission gun both with the BT and with the ET showed a similar trend.

With an increasing focusing voltage, the working distance becomes shorter (Figure 6.4). Similar to optical lenses, stronger lenses have shorter focal lengths, and increasing the focusing voltage results in a shorter working distance. In general, reasonable working distances should be between 10 and 30 mm for practical operation (Figure 6.5).

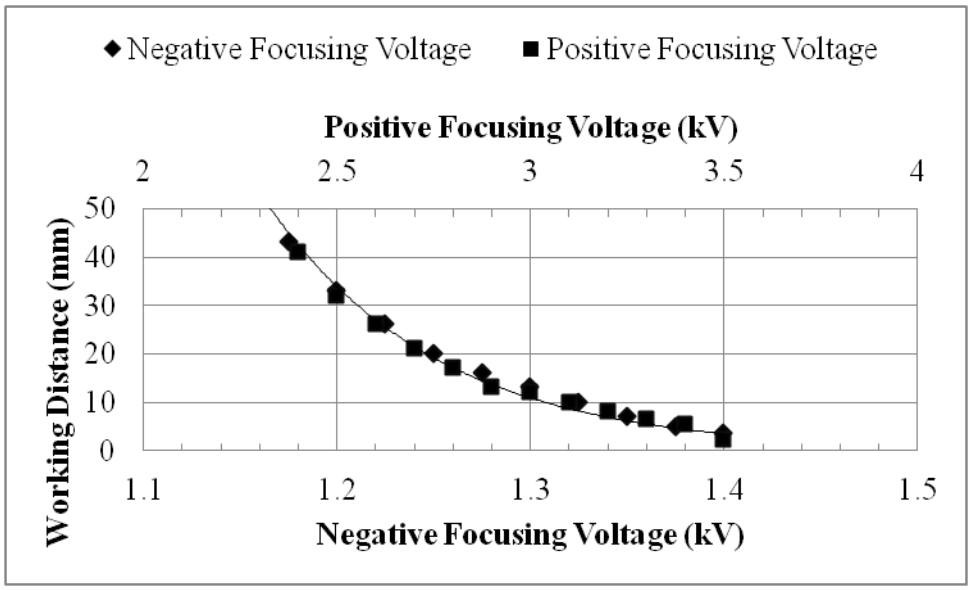

Figure 6.5 The working distance as a function of positive and negative focusing voltage (with exponential trend) for the thermionic electron gun (TEG) with electron focusing column with accelerating voltage, -2 kV. The decay is predicted from the understanding that stronger lenses have shorter focal lengths. The cold field emission gun both with the BT and with the ET showed a similar trend.

These results (Figure 6.4 and Figure 6.5) were further simulated for a variety of accelerating voltages. It was observed that the working distance as a function of focusing voltage is dependent on the accelerating voltage used. These results were combined to form an approximation for a focusing voltage given a desired working distance and accelerating voltage for each of the electron guns. Equations (6.4), (6.5) and (6.5) estimate the focusing voltage, V_f, with a given working distance, WD, and accelerating voltage, Vacc, for the TEG, the BT CFEG, or the ET CFEG, respectively. These equations were calculated from the trend of working distance as a function of focusing voltages, as seen in Figure 6.5.

$$V_f = V_{acc}(1 - {}^{1}/_{34} * \ln(WD * 10^6)) \quad (6.4)$$

$$V_f = V_{acc}(1 - {}^{1}/_{19} * \ln(WD * 400)) \quad (6.5)$$

$$V_f = V_{acc}(1 - {}^{1}/_{33} * \ln(WD * 10^6)) \quad (6.6)$$

As an example for the TEG, if the desired working distance is 30 mm and an accelerating voltage of -5 kV is used, the approximate focusing voltage needed is -2.5 kV. Similar equations can be derived for the positive focusing voltages as well.

6.4 Focusing Voltage Dependence: Current at the Sample Plane

During prototype testing, it was observed that the current at the sample plane depends on the focusing voltage (Figure 6.6). Simulations were done to model these results and identify the cause of this dependency. Figure 6.6 shows results from prototype testing of the electron column, attached to the TEG at the front end and also to a Faraday cup positioned just after the final aperture of the column. The simulated current at the focal plane for an accelerating voltage of -2 kV, is shown as well.

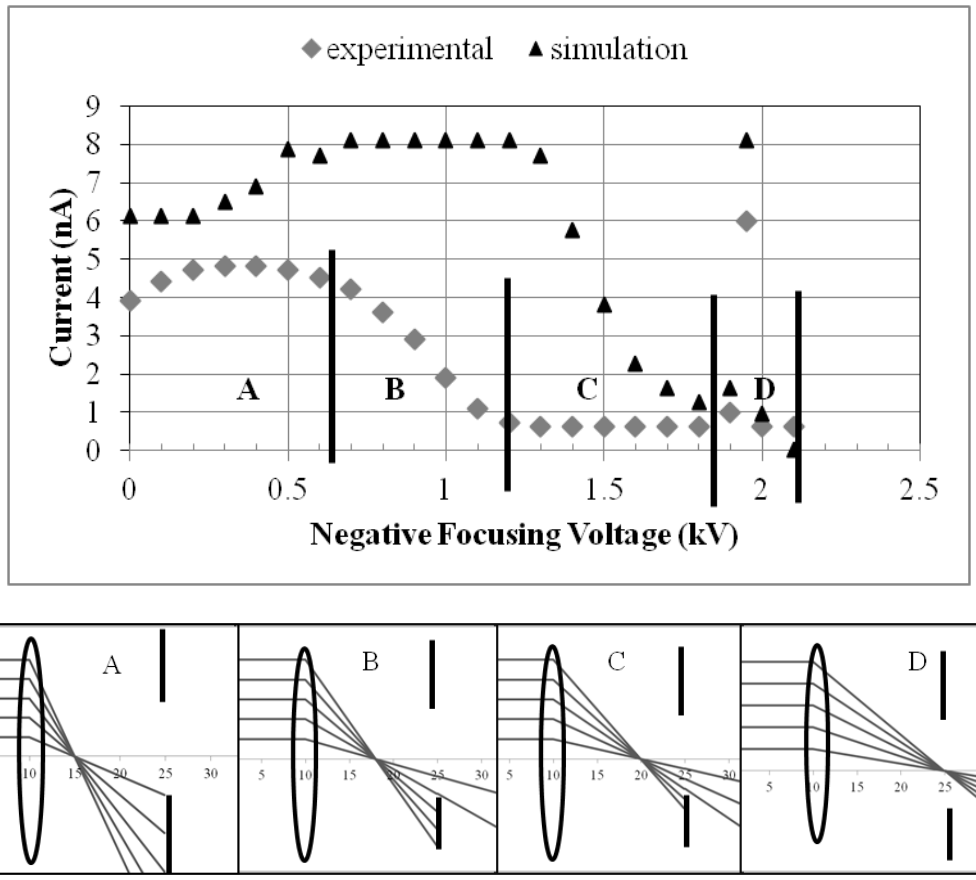

Figure 6.6 Experimental and simulated current in the Faraday cup for an accelerating voltage of -2 kV is shown in the upper plot. The peak at -1.98 kV and the dip in the current was a result of vignetting. The trends are similar in that there is a small peak followed by a rapid drop and a single large peak when the focusing voltage is close in value to the accelerating voltage. Vignetting for different focusing voltage regions designated A through D is shown in the lower diagram, using a lens followed by an aperture.

The current detected in the Faraday cup decreases as the focusing voltage increases and peaks close to the accelerating voltage (Figure 6.6). These effects were seen in both the experimental and simulated results. To understand why the current at the sample plane changed with focal length, the paths of electrons through a lens followed by a given aperture were calculated using optical paraxial ray trace equations for different focal lengths (Figure 6.6) [4]. These trends were not observed for the positive focusing

voltages because of the large difference in the dependencies between the positive and negative focusing voltages (Section 6.3).

The ray traces shown in the lower portion of Figure 6.6 show that the dependence of current on focusing voltage is a result of the position of the focus and therefore, a result of vignetting. If the focus is near or past the aperture, the current will be transmitted through the aperture. However, if the focus is significantly behind the aperture, the aperture will stop the electrons (vignetting); therefore, less current will be available at the sample plane.

It was observed that as the focusing voltage approached that of the accelerating voltage, the current measured in the Faraday cup significantly increased. When the focusing voltage continued to approach the accelerating voltage, the current dropped to zero (Figure 6.6). The peak in the current detected in the Faraday cup was observed for several different accelerating voltages. The experimental values were not accurate enough to identify the focusing voltage that corresponded to the peak in the current; however, the peak was consistently observed in the simulations to be at a focusing voltage 25 V more positive than the accelerating voltage (for instance if the accelerating voltage was at -5 kV, the current detected in the Faraday cup would peak at a focusing voltage of -4975 V).

6.5 Effect of Changing Physical Dimensions of the Electron Focusing Column

Changing the physical dimensions of the components of the electron focusing column, such as aperture diameters and thicknesses, affects the imaging resolution of the lunar mini-SEM. These affects were determined by calculating the depth of focus and

working distance (discussed in Sections 6.2 and 6.3) as a function of the physical dimension under investigation. Depth of focus was defined as twice the distance between the focal plane and the plane containing the largest spot capable of achieving the desired resolution. This indicates that any portion of the sample that is contained by the depth of focus will also be in focus [1, 2].

The first two physical dimensions investigated involved the second Einzel. The Einzel lens can be modeled using two identical thin lenses, so changing the thickness can be likened to moving these lenses with respect to one another. Changing the aperture diameter is analogous to changing the f-number of the lenses. Figure 6.7 shows the working distance as a function of the thickness of the second Einzel. Figure 6.8 shows the working distance as a function of the aperture diameter of the second Einzel.

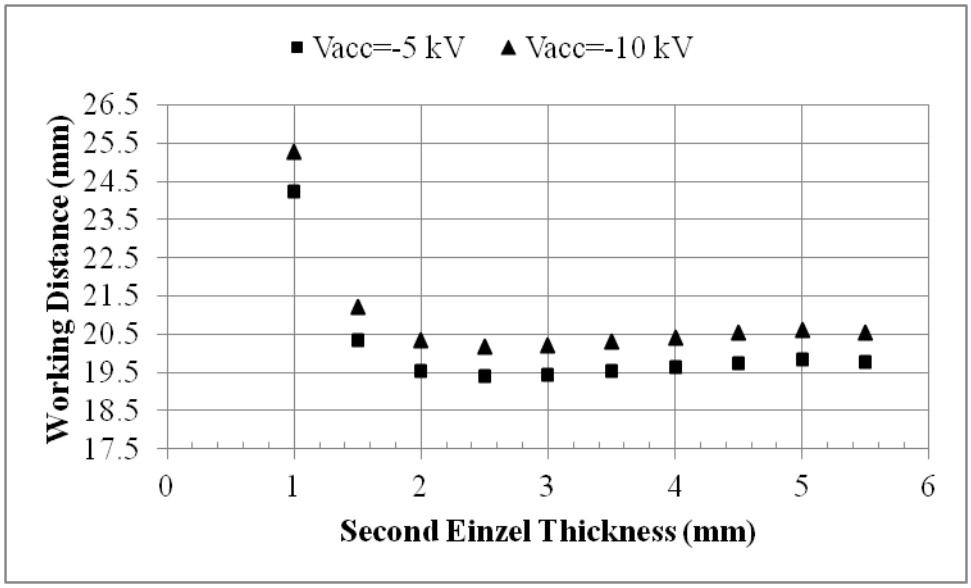

Figure 6.7 Working distance as a function of the thickness of the second Einzel for accelerating voltage, Vacc, of -5 kV and -10 kV and focusing voltage (V_f) of +5.7 kV and +11.5 kV, respectively. The second Einzel is the aperture in the Einzel lens with the focusing voltage applied.

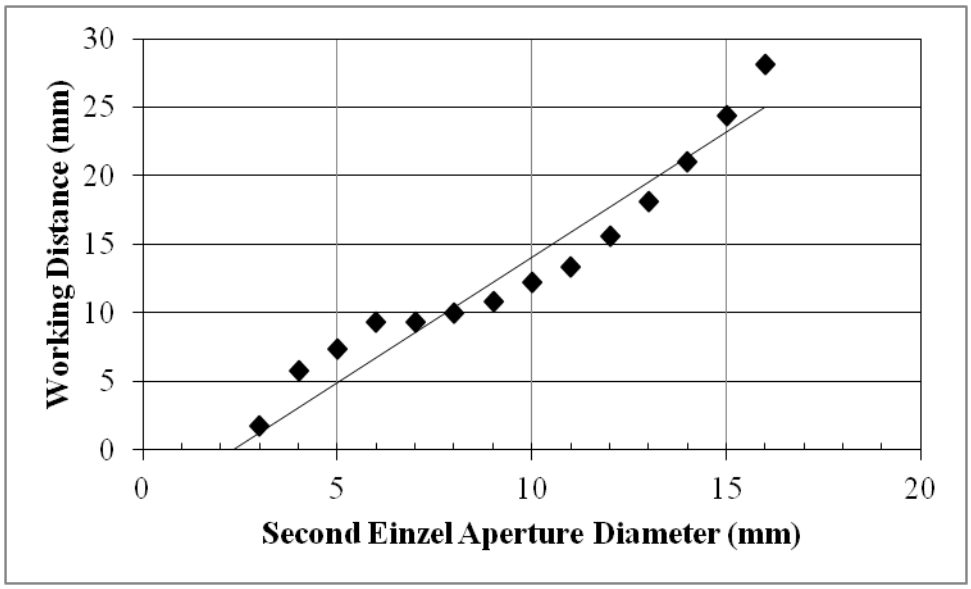

Figure 6.8 Working distance as a function of the aperture diameter of the second Einzel for an accelerating voltage of -5 kV and focusing voltage of +5.7 kV. The second Einzel is the aperture in the Einzel lens with the focusing voltage applied.

A thin second Einzel (1-2 mm) resulted in the maximum working distance. However, as the thickness of the second Einzel is increased, the working distance remains fairly constant (Figure 6.7). A desired working distance is one that would position the sample in the sample chamber such that its position relative to the detector is optimized (10-30 mm). If the working distance is too short, the possibility of obscuring detectable signal exists (especially since the samples of interest are not geometrically flat, but are rough rocks covered in dust). The maximum working distance must be constrained by the physical dimensions of the sample chamber. If it is too large (i.e., larger than the length of the sample chamber), the sample will never be in focus. As predicted, the working distance is linearly proportional to the aperture diameter of the second Einzel (Figure 6.8). This is because the aperture diameter of the second Einzel is

proportional to the magnitude of electric field inside the lens. The smaller the aperture diameter, the stronger the electric field is.

The other physical dimensions under investigation were those of the grounded apertures of the electron focusing column. The figures below (Figure 6.9, Figure 6.10 and Figure 6.11) show the effect of changing the following aperture diameters on the working distance and depth of focus (the amount of translation along the optical axis the sample can travel and still have a spot size less than or equal to the desired spot size): one of the apertures in the electron focusing column (Figure 6.9) and the first and third Einzel (Figure 6.10 and Figure 6.11, respectively). The grounded anode aperture diameter does not affect the depth of focus or the working distance since the aperture diameters in the electron focusing column were much smaller. Also, the thicknesses of these grounded apertures did not appreciably affect the resulting depth of focus and working distance.

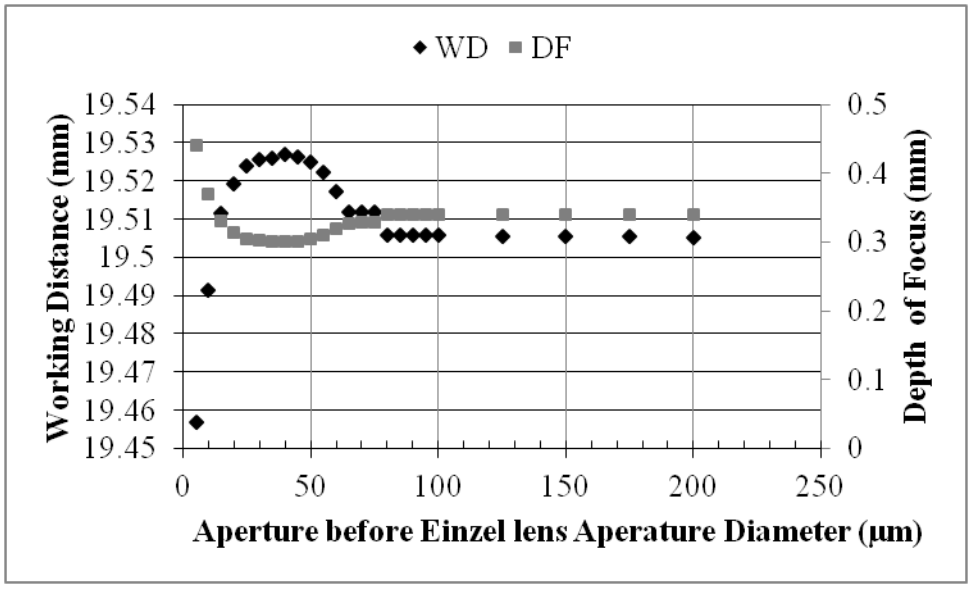

Figure 6.9 Working distance (WD) and depth of focus (DF) as a function of the aperture diameter of aperture located before the Einzel lens in the electron focusing column for an accelerating voltage of -5 kV and focusing voltage of +5.7 kV.

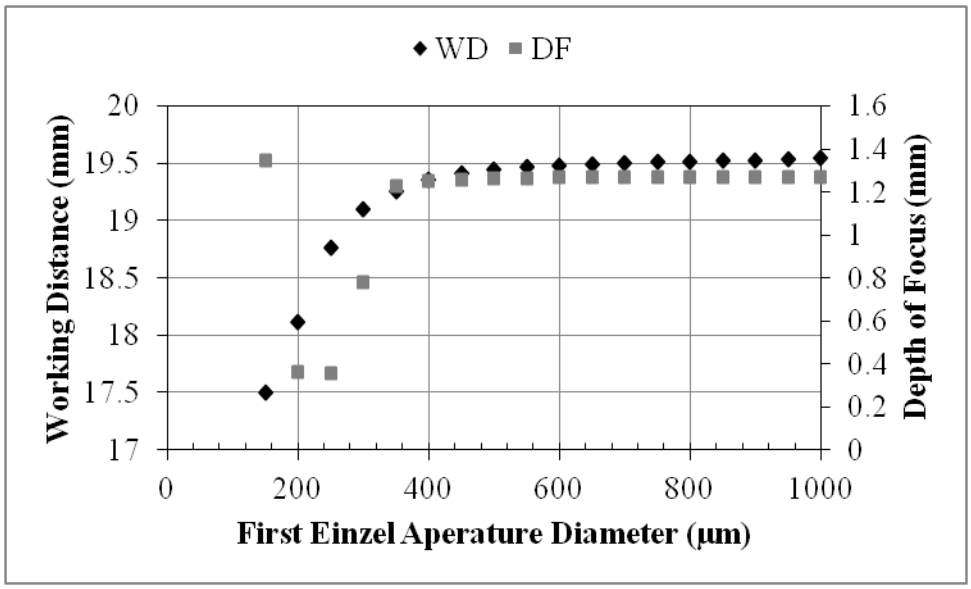

Figure 6.10 Working distance (WD) and depth of focus (DF) as a function of the aperture diameter of the first Einzel in the electron focusing column for an accelerating voltage of -5 kV and focusing voltage of +5.7 kV.

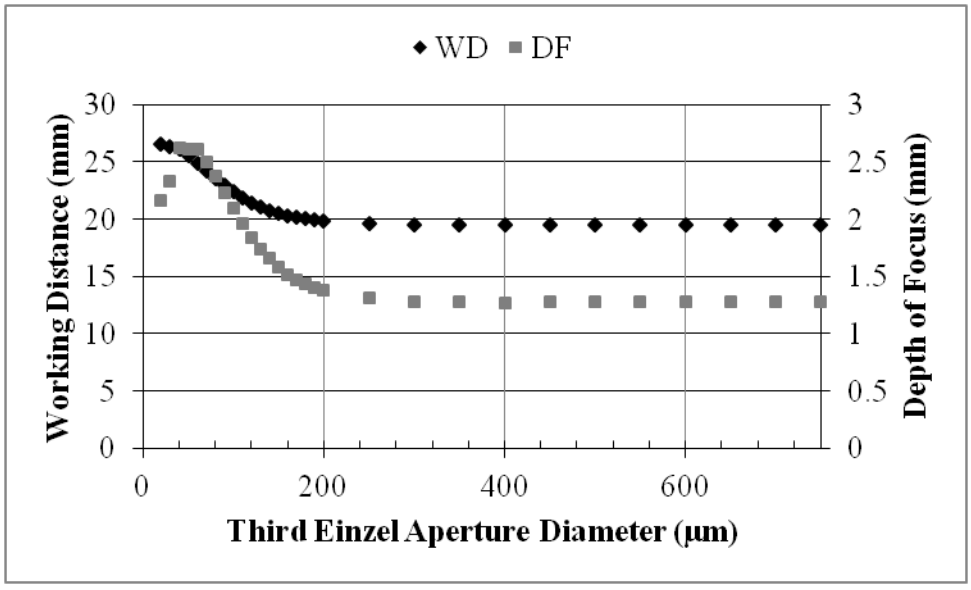

Figure 6.11 Working distance (WD) and depth of focus (DF) as a function of the aperture diameter of the third Einzel in the electron focusing column for an accelerating voltage of -5 kV and focusing voltage of +5.7 kV.

All of the working distances and depth- of-focus values showed a strong dependence on the aperture diameters of the grounded apertures when the apertures were small (Figure 6.9, Figure 6.10 and Figure 6.11). For larger aperture diameters, the working distance and depth of focus were constant with aperture diameter. The optimum aperture diameter would be where the depth of focus is at a maximum and the working distance is at a minimum while maintaining sufficient current for analysis. The depth of focus will be discussed in greater detail in the following chapter.

6.6 Conclusions

Simulations were performed to determine the effectiveness of an idealized lunar mini-SEM electron focusing column, to examine the electron focusing column's configuration and to optimize working conditions. The purpose of an electron focusing column is to focus the electron beam onto a sample while maintaining sufficient current for imaging and analysis, at a high resolution (small spot size).

Through this research the following was determined:

- The effects from changes in negative focusing voltage on the working distance were greater than the effect from changes in the positive focusing voltage. This is predicted in the simulations and was confirmed by the experimental results.
- The working distance as a function of focusing voltage depended linearly on the accelerating voltage. Equations for each of the electron guns estimating this dependence are given.

- The current at the sample plane is dependent on the working distance. The dependency was shown to be a result of vignetting. It was more readily seen in the negative focusing voltage because the optical power of the electron lens changes more rapidly with negative focusing voltage.
- The working distance was shown to be dependent on the thickness of the second Einzel, the aperture in the Einzel lens with the focusing voltage applied. Therefore, the second Einzel thickness needs to be at the thickness that produces an optimal working distance.
- The working distance was shown to have a linear dependence on the aperture diameter of the second Einzel. Therefore, the second Einzel aperture diameter needs to be determined, such that an optimal working distance is defined while maximizing current at the sample.
- It was also shown that the depth of focus and working distance were dependent on the aperture diameters of the grounded apertures of the electron focusing column when the apertures were small. (The depth of focus will be discussed in greater detail in the following chapter.)

From these results, the optimal values for the various parameters investigated were determined (Table 3.5). These values are based on simulation results and on the geometric restrictions of the lunar mini-SEM mechanical design and the requirement that the current at the sample be no less than 1 nA (sufficient for imaging and x-ray analysis) and the working distance be between 10 mm and 30 mm [3].

Table 6.3 Settings for optimal imaging parameters The resulting values are for the ET CFEG with an accelerating voltage of -5 kV with a focusing voltage of -2.5 kV(+6 kV), but can also be achieved with an accelerating voltage of -10 kV with focusing voltage of -5 kV(+12 kV).

Aperture Diameter of Entrance Pupil (μm)	75-100
Aperture Diameter of First Einzel (μm)	150-200
Thickness of Second Einzel (mm)	2-4
Aperture Diameter of Second Einzel (mm)	10-15
Aperture Diameter of Third Einzel (μm)	100-200
Optimal Working Distance (mm)	10-30
Minimum Current at Sample Plane (nA)	1.0

For optimal working conditions, the working distance needs to be between 10 mm and 30 mm. This allows for the sample to be far enough away to ensure that the secondary electrons are not geometrical hidden from the detector, but close enough to have easily achievable focus. (The depth of focus will be discussed in greater detail in the following chapter.) The necessary thicknesses and aperture diameters to achieve this optimum are as follows. The aperture diameter of a diameter before the Einzel lens (Entrance Pupil) needs to be between 75 μm and 100 μm. The aperture diameter of the first Einzel needs to be between 150 μm and 200 μm. The aperture diameter of the second Einzel needs to be between 2 mm and 4 mm. The aperture diameter of the second Einzel needs to be between 100 μm and 200 μm.

The benefit of using a positive focusing voltage is the working distance is less sensitive to changes in it than a negative focusing voltage, allowing for more accurate location of the sample plane. The benefit of using a negative focusing voltage, on the other hand, is that lower focusing voltages are required. Therefore, depending on the application and available power, a negative or positive focusing voltage could be used.

CHAPTER VII

IMAGING CRITERIA AND CONSIDERATIONS

7.1 Introduction

Several factors control the resolution of an electron microscope, such as the spot size and current contained in the electron probe (electron beam at the sample). The most significant of these are the working distance, depth of focus and aberrations. The working distance is the distance between the last component of the electron focusing column (the end of the scanning system) and the focal plane [1]. The depth of focus is the distance that the sample can vary and still have a spot diameter that is smaller than desired electron probe size (Figure 7.1) [1, 2]. This indicates that any portion of the sample that is contained by the depth of focus will also be in focus [1, 2]. Aberrations are caused by variations in the energy of the electron beam and by the difference in electric field strength that each electron experiences. These cause the focus to spread, such that the electrons in the beam do not always focus at the same location.

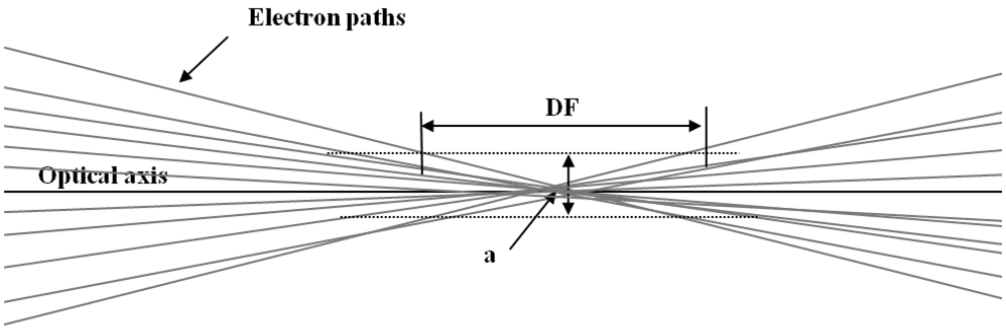

Figure 7.1 In this illustration DF is the depth of focus, and **a** represents the desired electron probe size which is directly proportional to the resolution [1, 2].

Simulations were performed using CPO2DS, a commercially available charged particle optics simulation program, to quantify the quality of the mini-SEM's imaging capabilities [3]. Discussion on the parameters of the simulated electron gun and focusing column occur in previous chapters (Chapter 3-6).

7.2 Working Distance

The working distance is the distance between the last component of the electron focusing column and the focal plane. Shorter working distances correspond to smaller electron probe sizes (higher resolutions); however, if the sample is too close to the last element of the electron focusing column, the resulting electron signal (electrons reflected/ejected from the surface of the sample) can be geometrically shielded from the detectors [1, 2]. The working distance was calculated from the simulation as a function of focusing voltage (the applied voltage on the second Einzel in the electron focusing column as discussed in Chapter 6) for the thermionic electron gun (TEG), and the etched tip cold field emission gun (ET CFEG) with the electron focusing column attached (Figure 7.2).

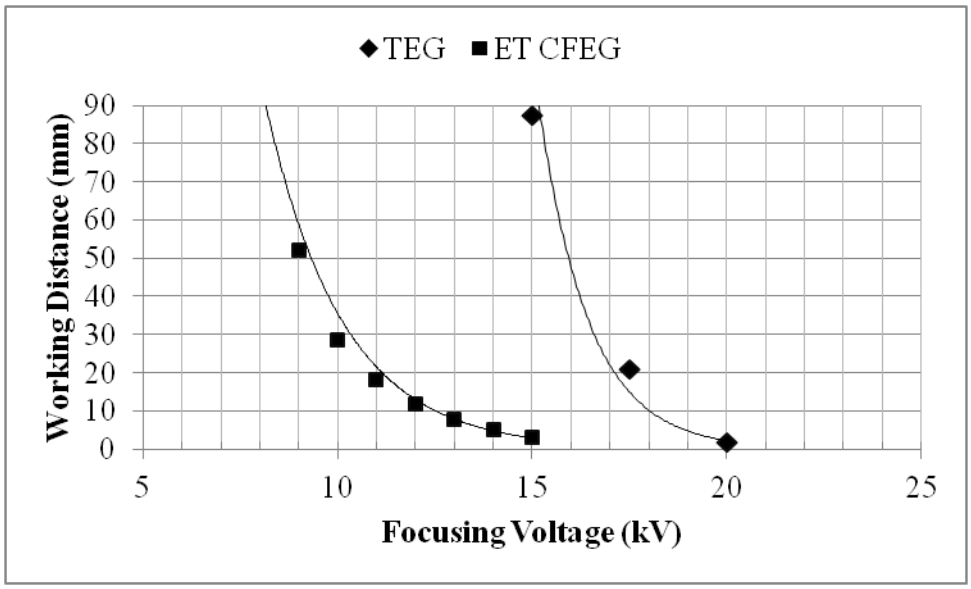

Figure 7.2 The working distance as a function of the focusing voltage (with exponential fit) for the thermionic electron gun (TEG) and the etched tip cold field emission gun (ET CFEG) for an accelerating voltage of -10 kV is plotted. An inverse decay is expected from the optical power of the lens being the reciprocal of the focal length of the lens.

The working distance decreases as the focusing voltage is increased for all of the electron gun types (Figure 7.2). As seen in this figure, the ET CFEG has a shorter working distance than the TEG for the same focusing voltages. This was caused by the differences in thermionic emission and cold field emission operation, namely the preliminary spot provided by the Wehnelt cylinder which decreases the beam divergence.

The working distance (using the TEG) was determined for different accelerating voltages as a function of modulated focusing voltage. The figures below show the working distance versus the accelerating voltage, using negative focusing voltages (Figure 7.3) and positive focusing voltages (Figure 7.4). The focusing voltage modulation, MV_f, is defined as:

$$MV_f = \frac{(|Vacc| - |Vf|)}{|Vacc|}. \quad (7.1)$$

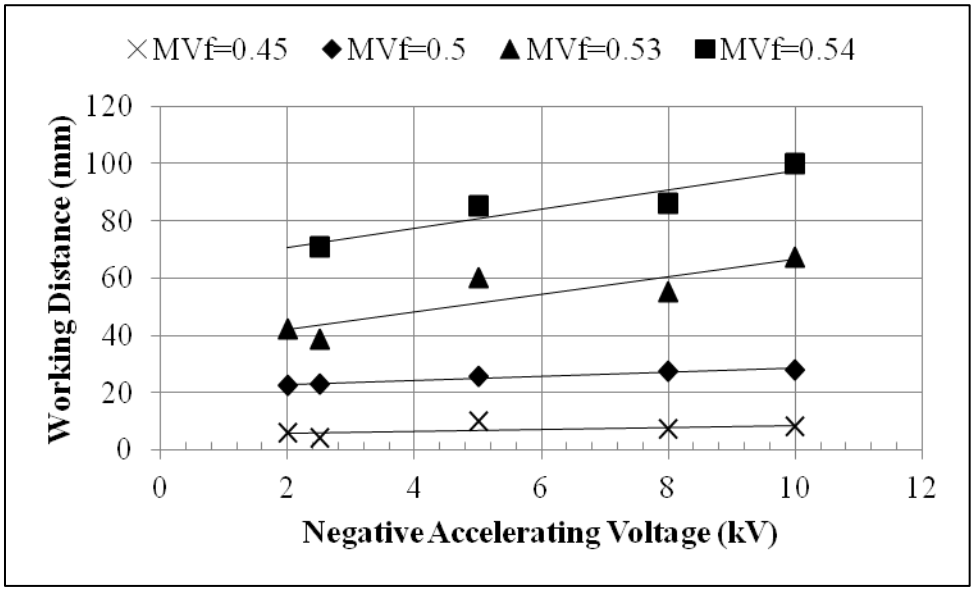

Figure 7.3 Working distance as a function of the negative accelerating voltage with linear trend for focusing voltage modulated, MV_f, of 0.45, 0.5, 0.53 and 0.54. This was for a negative focusing voltage.

As expected, the working distance only changes slowly with the accelerating voltage (Figure 7.3). For instance, the working distance for a focusing voltage modulation of 0.5 changed from 22.4 mm to 28 mm for an accelerating voltage that was varied from -2 kV to -10 kV.

As seen previously in Section 6.3, the focusing voltage has a significant effect on the working distance (Figure 7.3). For example, the working distance changed from -1 to 280 mm for focusing voltage modulations of 0.4 (V_f=-3.0 kV) to 0.56 (V_f= -2.2 V) with an accelerating voltage of -5 kV. Similar results were observed using a positive focusing voltage (Figure 7.4).

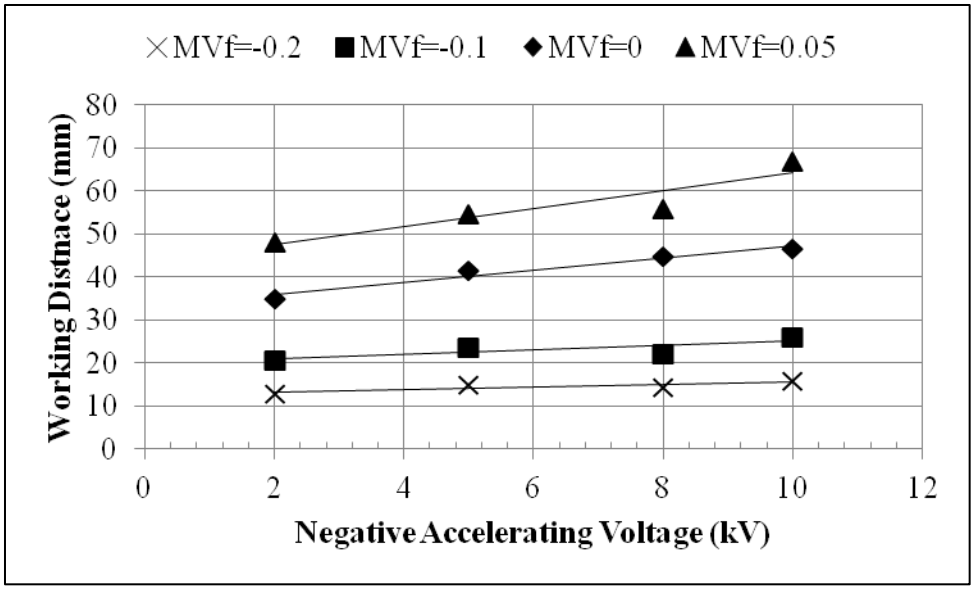

Figure 7.4 Working distance as a function of the accelerating voltage with linear trend for focusing voltage modulations, MV_f, of -0.2,-0.1, 0 and 0.05. This was for positive focusing voltages.

The working distance exhibited a linear dependence on the accelerating voltage (Figure 7.4 and Equation (6.4), (6.5) and (6.6)). For instance, the working distance for a focusing voltage modulation of 0 (the focusing voltage being equal to the absolute value of the accelerating voltage) changed from 35 mm to 46 mm for accelerating voltages from -2 kV to -10 kV.

As with negative focusing voltages, the positive focusing voltages had a significant effect on the working distance. For example, the working distance changed from approximately 15 mm to 65 mm, for focusing voltage modulations varied from -0.2 (V_f = 12 kV) to 0.05 (V_f = 9.5 kV) for an accelerating voltage of -10 kV.

The working distance was also simulated as a function of the focusing voltage modulation for different accelerating voltages (Figure 7.5 and 7.6). From Section 6.3, the working distance decreases exponentially with the focusing voltage. According to

Equations (7.1) and (6.4)-(6.6), the working distance should increase with the focusing voltage modulation.

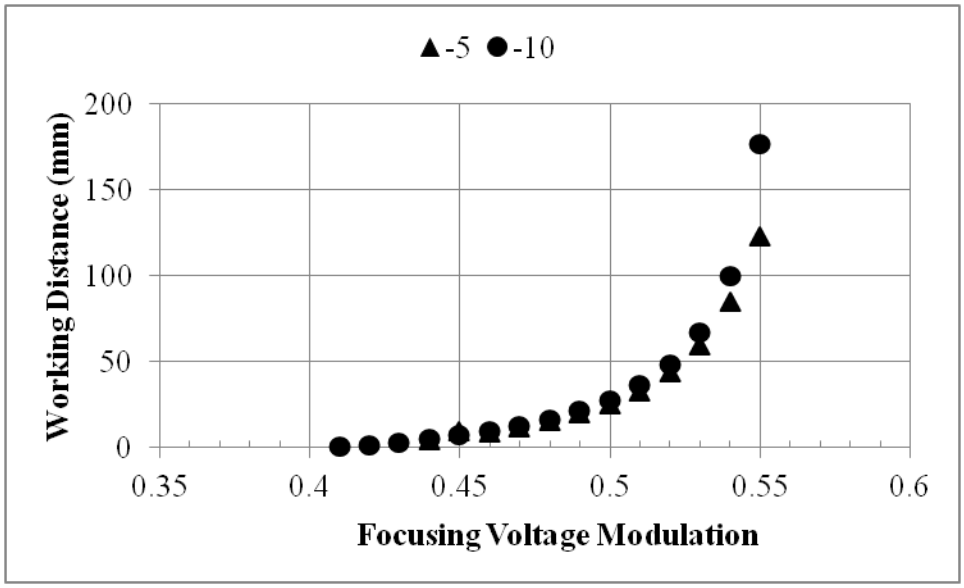

Figure 7.5 Working distance as a function of the negative focusing voltage modulation for accelerating voltages of -5 kV and -10 kV. The simulations for accelerating voltages of -2, -2.5, and -7.5 kV were also performed, and these resulted in the same trend.

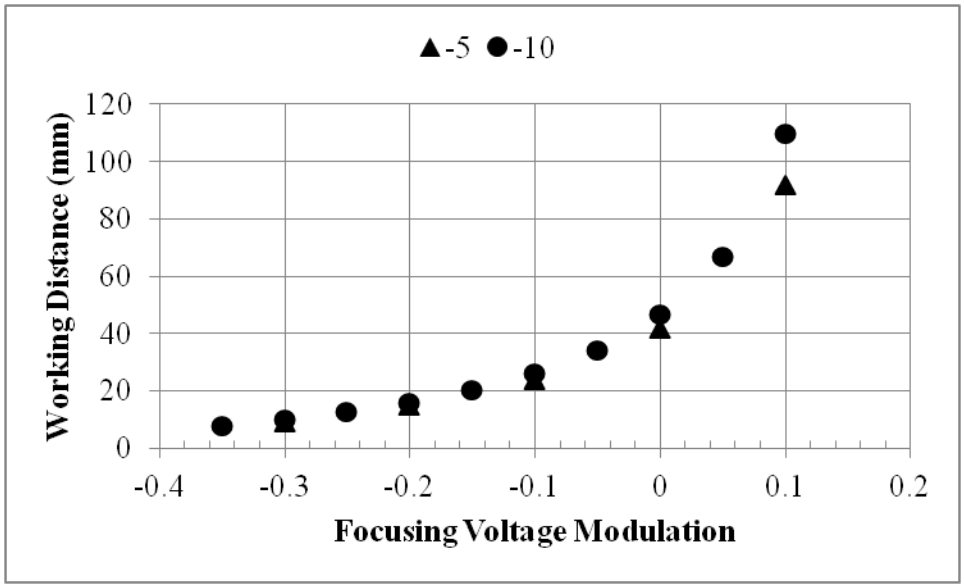

Figure 7.6 Working distance as a function of the positive focusing voltage modulation (with exponential trend) for accelerating voltages of -5 kV and -10 kV. The simulations

for accelerating voltages of -2, -2.5, and -7.5 kV were also performed, and these resulted in the same trend.

The working distance increases exponentially with the focusing voltage modulation (Figure 7.5 and Figure 7.6). The working distance, as has been previously observed, has a very weak dependence on the accelerating voltage (Figure 7.5 and Figure 7.6), confirming Equations (6.4)-(6.6).

Also, a comparison between Figure 7.5 and Figure 7.6 indicates a similar result as that found in Section 6.3 regarding the dependence of the working distance on the positive compared to the negative focusing voltages. The negative focusing voltage has a greater effect on the focal plane than the positive focusing voltage.

7.3 Depth of focus

Figure 7.1 illustrates (with description in Section 7.1) that the depth of focus (DF) is the depth in which the sample is in focus and is defined as the distance that a spot incident on the sample maintains a diameter that is smaller than or equal to the desired electron probe size [1, 2]. The depth of focus was calculated from the simulations by determining the distance between the location of the plane in which the electron path farthest from the optical axis came within the desired electron spot diameter and the focal plane.

The depth of focus as a function of the focusing voltage was calculated (Figure 7.7 and Figure 7.8). The focusing voltages were chosen so that the working distance was between 100 mm and 5 mm. These are the extreme outside working distances; working distances of smaller than 5 mm could not be easily measured using the prototype, and

working distances of greater than 100 mm are impractical operationally and can require a more complex detector to sample geometry. Typical operating working distance range is 10-30 mm. Figure 7.7 and Figure 7.8 show the depth of focus as a function of the focusing voltage for different electron probe diameters at an accelerating voltage of -10 kV and an extraction voltage of -3.5 kV for the ET CFEG and TEG, respectively.

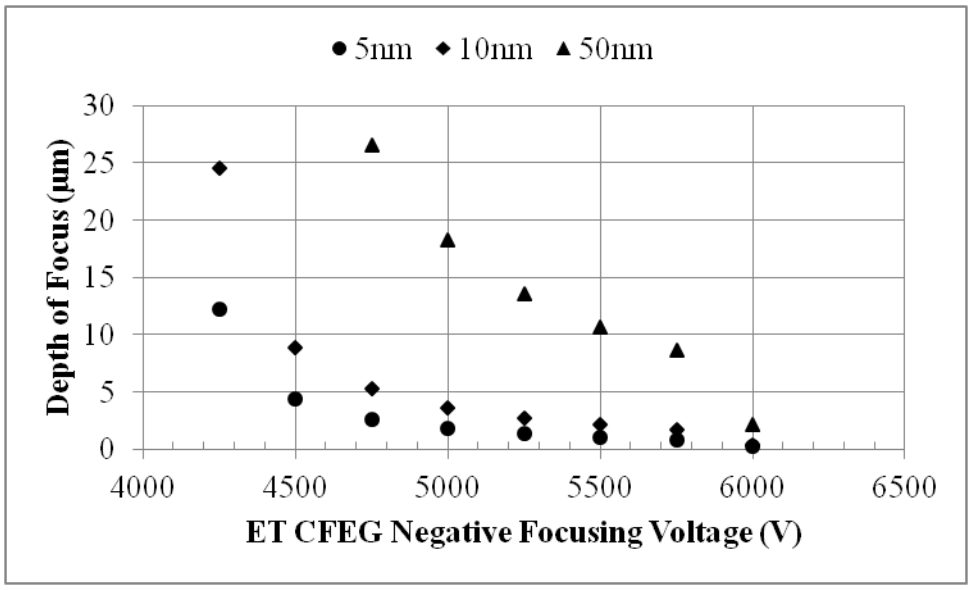

Figure 7.7 Depth of focus as a function of the focusing voltage for electron probe diameters of 5, 10 and 50 nm for the ET CFEG

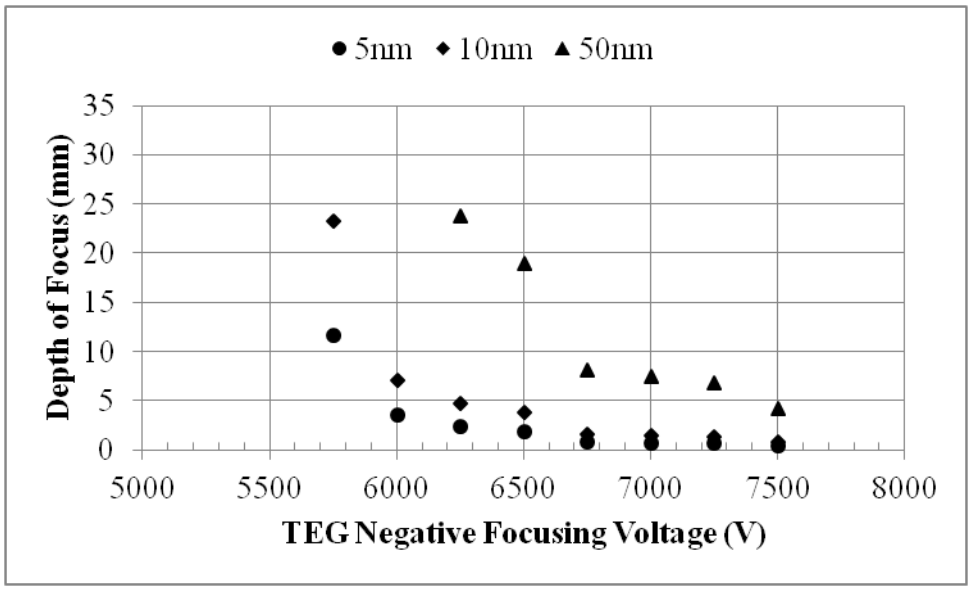

Figure 7.8 Depth of focus as a function of the focusing voltage for electron probe diameters of 5, 10 and 50 nm for the TEG. Note the depth of focus is in the millimeters where for the CFEG, depth of focus was in the microns.

The depth of focus decreases as the optical power on the lenses increases for all electron guns (Figure 7.7 and Figure 7.8). A comparison of Figure 7.7 with Figure 7.8 shows that, for these electron probe sizes, the CFEG had a 1000x smaller depth of focus than the TEG. The reason that the TEG had a much longer depth of focus for the same electron probe size can be attributed to the Wehnelt cylinder. The Wehnelt cylinder decreases the spread of the electrons which decreases the beam divergence (observed in the different working distances, Figure 7.2), thereby increasing the depth of focus [2].

7.4 Depth of Focus as a Function of Working Distance

Both the depth of focus and the working distance are strongly dependent on the focusing voltage. Therefore, the depth of focus and working distance were calculated for several different spot diameters with the TEG. Figure 7.9 and Figure 7.10 show the depth of focus as a function of the working distance for different accelerating voltages and for

negative focusing voltages at specific electron probe sizes. Figure 7.11 and Figure 7.12 give the depth of focus as a function of the working distance for these same accelerating voltages but for positive focusing voltages.

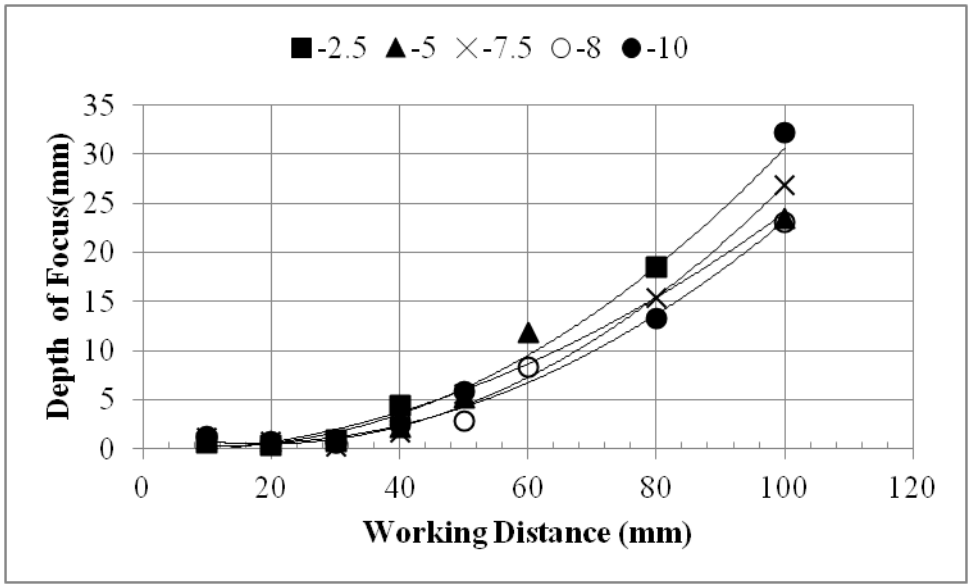

Figure 7.9 Depth of focus as a function of the working distance for accelerating voltages of -2.5 kV, -5 kV, -7.5 kV,-8 kV and -10 kV at an electron probe size of 10 nm for negative focusing voltages (with quadratic fit).

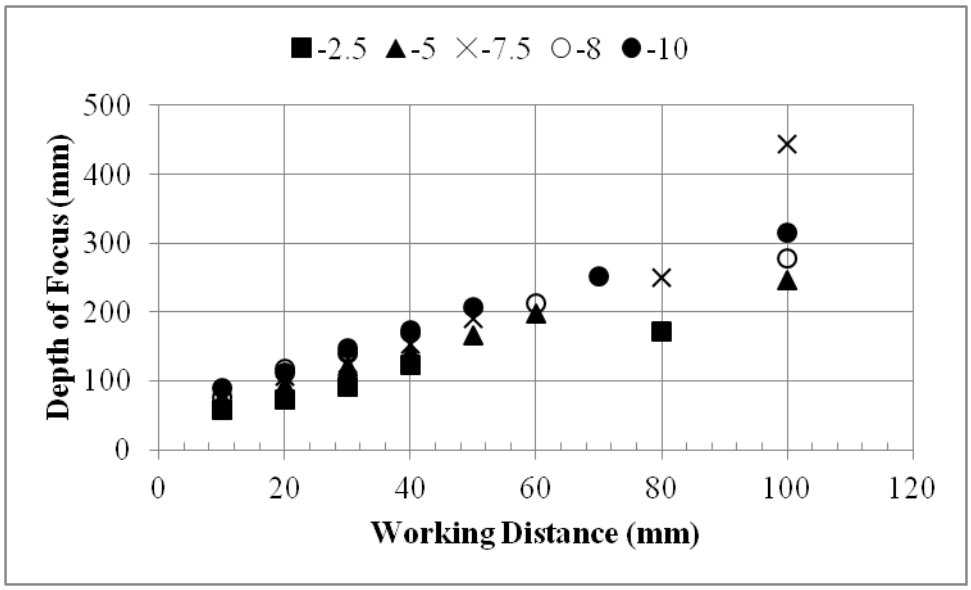

Figure 7.10 Depth of focus as a function of the working distance for accelerating voltages of -2.5 kV, -5 kV, -7.5 kV,-8 kV and -10 kV at an electron probe size of 1 µm for negative focusing voltages. The trend is initially linear, deviating only at working distances greater than 60 mm.

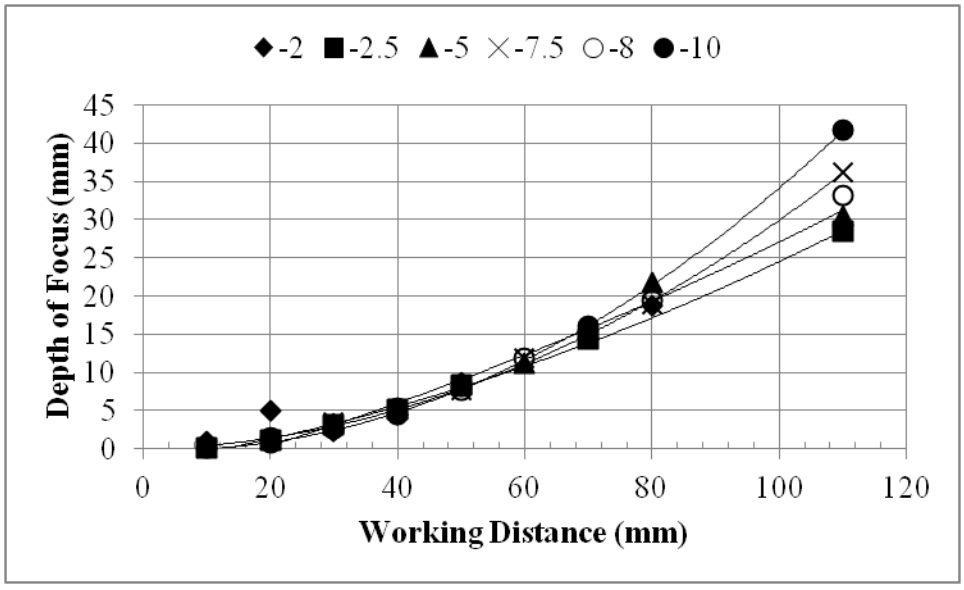

Figure 7.11 Depth of focus as a function of the working distance for accelerating voltages of -2 kV, -2.5 kV, -5 kV, -7.5 kV,-8 kV and -10 kV at a resolution of 10 nm for positive focusing voltages (with quadratic fit)

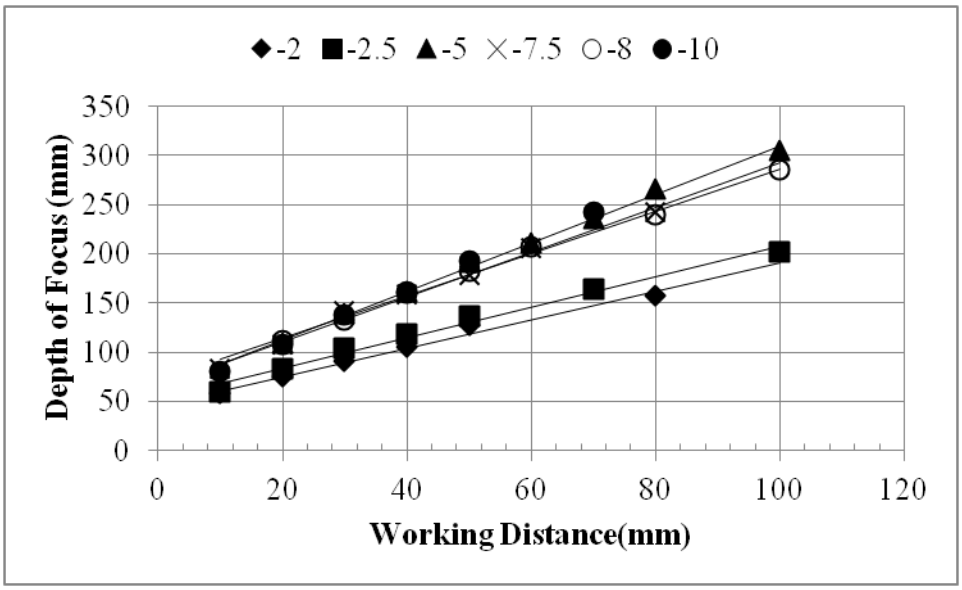

Figure 7.12 Depth of focus as a function of the working distance for accelerating voltages of -2 kV, -2.5 kV, -5 kV, -7.5 kV,-8 kV and -10 kV at a electron probe size of 1 μm for positive focusing voltages (with linear fit).

The depth of focus for small electron probe sizes (~10 nm) has a quadratic dependency on the working distance (Figure 7.9 and Figure 7.11). The depth of focus for large electron probe sizes (~1 μm) is approximately linearly dependent on the working distance (Figure 7.10 and Figure 7.12). Such large probe sizes are not typical, nor are they desired for SEMs. However, during prototype testing of the lunar mini-SEM it is necessary to understand practical working conditions related to larger electron probe sizes. In these graphs, the dependency did not appreciably change for positive or negative focusing voltages or even different accelerating voltages.

The depth of focus as a function of working distance was calculated for different electron probe sizes (Figure 7.13 and Figure 7.14).

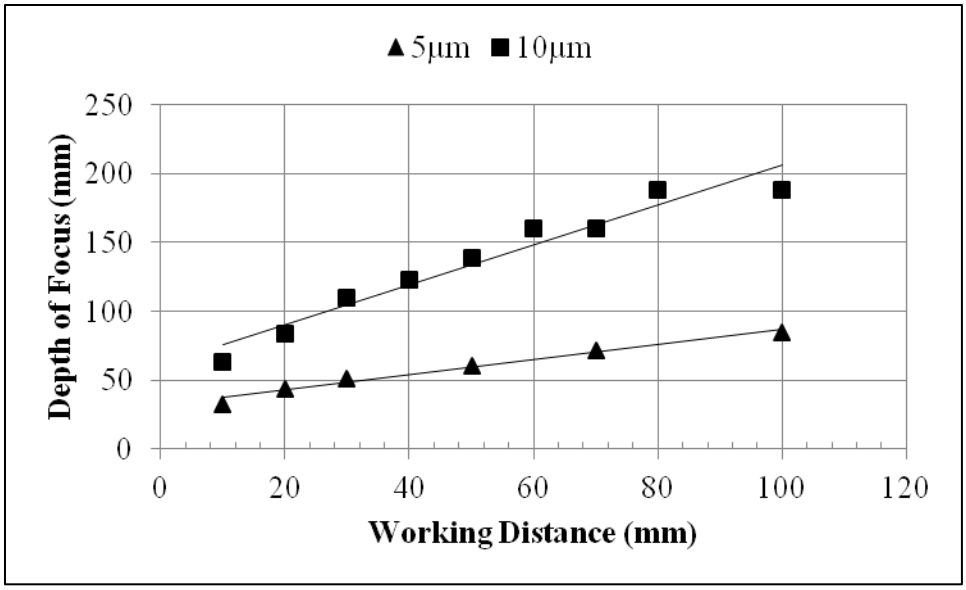

Figure 7.13 Depth of focus as a function of the working distance for an accelerating voltage of -7.5 kV and for different electron probe diameters: 5 µm and 10 µm. These values for electron probe sizes, while high for SEM, were chosen to get an outside estimation of the depth of focus.

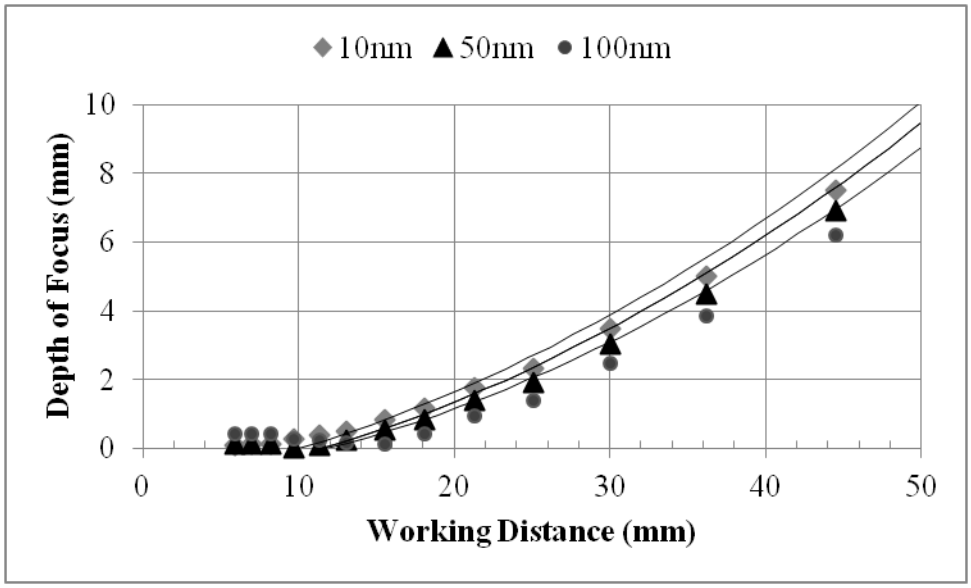

Figure 7.14 Depth of focus as a function of the working distance (with polynomial fit) for accelerating voltage of -7.5 kV and for different electron probe diameters: 10 nm, 50 nm and 100 nm.

For small electron probe sizes (on the order of a few nanometers), the change of depth of focus is small (Figure 7.13). For instance, for a working distance of 50 mm, the depth of focus for an acceptable electron probe diameter of 10 nm is 7.5 mm and for 50 nm is 6.9 mm. For large electron probe sizes (on the order of microns), the depth of focus changes rapidly with the electron probe size (Figure 7.13). A quadratic dependence on working distance for small electron probe size (Figure 7.13) was observed, as was a linear dependence on working distance for large electron probe size (Figure 7.13). These dependencies were observed previously in Figures 7.10-7.13.

7.5 Aberrations and Resulting Spot Size

The depth of focus estimates assumed that the electrons all focus at the same location on the optical axis. This however is incorrect. Aberrations, such as spherical and chromatic, spread the focus.

Spherical aberration results from electrons that are farther away from the optical axis being focused at a different location than those closer to the optical axis (Figure 7.15) [1, 2]. Chromatic aberration results from variations in lens strength for electrons of different energies [1].

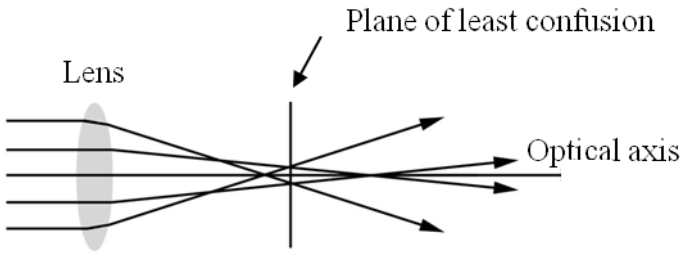

Figure 7.15 Spherical aberration is a result of electrons farther away from the optical axis focusing at different locations from those closer to the optical axis [1, 2].

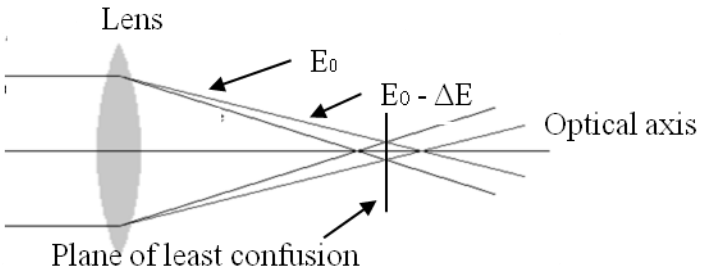

Figure 7.16 Chromatic aberration is a result of variations in lens strength for electrons of different energies [1, 2]

These aberrations further limit the minimum spot size, thereby limiting the achievable electron probe size. Using the following equations, the spot size (d_p) as a result of spherical aberration (d_s), the chromatic aberration (d_c), and the geometry of the electron gun (the geometric optics estimation of the spot size), (d_g) was calculated [1]:

$$\mathbf{d_s = M * Cs * \alpha^3} \tag{7.2}$$

$$\mathbf{d_c = M * Cc * \alpha \frac{\Delta E}{E_0}} \tag{7.3}$$

$$\mathbf{d_g = M * d_T} \tag{7.4}$$

$$\mathbf{d_p = \sqrt{{d_s}^2 + {d_c}^2 + {d_g}^2}} \tag{7.5}$$

In these equations, M is the linear magnification, Cs and Cc are the spherical and chromatic aberration coefficients with units of length (as does their optical counterparts), respectively, α is the beam divergence angle for an axial object point, ΔE is the energy spread, E_0 is the initial energy and d_T is the diameter of the tip of the cathode in the electron gun. The optical equivalent for the spherical aberration spot size, d_s, is transverse

spherical aberration and depends on the angle in the same manner (3^{rd} power). The optical equivalent for the chromatic aberration spot size, d_c, is lateral chromatic aberration (or lateral color). The spot size resulting from the geometry of the electron, d_g, is essentially the geometric image of the tip of the cathode in the electron gun at the sample plane.

The ranges for the energy spread are typically 1-2 eV for the TEG and <0.2-0.4 eV for the CFEG [1]. It is apparent from these equations that the electron probe size depends on the energy spread, the energy of the electrons, the magnitude of the spread of electrons, and the size of the tip of the cathode for each of the electron guns. Attempts were made to calculate the chromatic and spherical aberrations for the different electron guns; however, the coefficients determined by the simulation in CPO2DS were nonrealistic [3].

Other aberrations can be ignored because they were negligible (diffraction) or incalculable with the symmetries used to create the electron gun and focusing column simulation (coma and astigmatism). For instance, diffraction is negligible since the wavelength of the electrons was on the order of tenths of picometers, whereas, the smallest aperture was micrometers in diameter. Astigmatism is a result of an error in the cylindrical symmetry of the system, which can be minimized when the assumption is that the system has cylindrical symmetry.

7.6 Conclusions

The electron focusing column is used to focus the electron beam, generated by the electron gun, to a spot on the sample surface in such a way as to achieve a small electron

probe size while maintaining adequate current at the sample for analysis (1 nA). As anticipated, the electron probe size achievable for the CFEG was smaller than that for the TEG. The working distance and depth of focus were both shown to strongly depend on the focusing voltage. In addition, the depth of focus for equal acceptable diameters was shown to be much greater for the TEG than for the CFEG which is expected because the Wehnelt cylinder in the TEG works as a weak primary lens before the electron column.

Through this research the following was determined:

- The aberrations were greater for the TEG than for the CFEG.
- The working distance was shown to decrease exponentially with focusing voltage, as the focal length is dependent on the optical power of the lens.
- The working distance was shown to be linearly dependent on accelerating voltage.
- The depth of focus was shown to be linear with working distance for large electron probe sizes (μm) and parabolic for small electron probe sizes (nm).
- For large electron probe sizes, the slope of the line of depth of focus as a function of working distance was shown to directly depend on the electron probe size.
- It was also shown that the depth of focus is exponential with focusing voltage.

From these results, the optimal values for the various parameters investigated were determined (Table 3.5). These values are based on simulation results and on the geometric restrictions of the lunar mini-SEM mechanical design and the requirement that the current at the sample be no less than 1 nA (sufficient for imaging and x-ray analysis) [3].

Table 7.1 Settings for optimal imaging parameters

Accelerating Voltage (kV)	-10
Focusing Voltage (kV)	-5 or +12
Desired Working Distance (mm)	10-30
Maximum Electron probe size (nm)	100
Minimum Current at the Sample (nA)	1
Depth of Focus (μm for CFEG, mm for TEG)	2-3

CHAPTER VIII

CONCLUSIONS

The objective of this investigation was to determine the necessary conditions for optimal performance of a miniaturized scanning electron microscope (mini-SEM). Therefore, the most significant results were those related to the electron probe current and diameter; where the electron probe refers to the electron beam at the sample. The optical components of a scanning electron microscope mainly consist of an electron gun, which produces a beam of electrons, an electron focusing column, which focuses and limits the electron beam, and a scanning system, which scans the electron beam across a sample. The focus of this investigation was on the electron gun and focusing column. Two distinct electron guns were investigated along with a proprietary electron focusing column. Through simulations and testing, optimized emission and electron probe currents, electron probe diameter, working distance and depth of focus produced by this mini-SEM were determined.

These values at optimum settings would maximize the electron probe current, minimizes the electron probe diameter (a small probe diameters corresponds to high resolution), while maintaining a reasonable working distance and the depth of focus.

All of the parameters under investigation are interrelated, resulting in a complex system. Optimizing one parameter can cause others to drift from their peak performance. For instance, probe current (the current incident on the sample plane) can be increased by increasing the size of the apertures in the mini-SEM; however, this decreases the depth of focus and increases the probe diameter. The working distance can be decreased by increasing the focusing voltage, but that decreases the depth of focus and can negatively affect the electron probe diameter. This inter-dependence of these values can cause the optimization of the mini-SEM to become difficult and requires careful consideration when carrying out the simulations.

The first electron gun type investigated was the cold field emission gun, which consists of a cathode, an extractor and a grounded anode. Cold field emission is solely dependent on the electric field at the emission region (Fowler-Nordheim equation). Specifically, the emission current is determined by the localized geometric field enhancement factor and the voltage difference across the cathode and the extractor. The electric field, through the enhancement factor, was shown to depend on several variables, including the diameter of the cathode at the tip, the distance between the cathode and extractor, and the size of the emission region (i.e., the virtual source size).

Two different cold field emission cathodes were investigated: a cathode with a blunted tip and one with a shaped-etched tip. The shaped-etched tip is smooth and spherical in nature while the blunted tip has multiple protrusions covering its surface.

The shaped-etched tip is what the mini-SEM was designed for and was shown to produce the most emission current. The shaped-etched diameter was set to be 1 μm (as a result of the shaping procedure) – even though the etched tip virtual source size is much

smaller (on the order of 100 nm or less). The electric field, as expected, was shown to be inversely dependent on the distance between the cathode and the extractor, and directly dependent on the extraction voltage. The electric field was also shown to be inversely dependent on the cathode tip diameter. The emission current increases with emission region diameter and decrease exponentially with cathode tip diameter and distance. The percentage of the emission current transmitted through the grounded anode decreases exponentially with emission region diameter, increases with cathode tip diameter, and is roughly independent of the distance between the cathode and the extractor for distances less than 200μm.

The blunted tip cathode does not produce stable emission and was used primarily to test the cold field emission gun housing and control system for its robustness. In the simulation, the electric field, emission current and current through the grounded anode was dependent on the distance and extraction voltage; similar to that of the shaped-etched tip. The instability is caused by the irregular surface geometry, in the form of many small protrusions located on the surface of the tip. Multiple protrusions can emit, due to their local electric field strength. To make matters worse, new protrusions are constantly being formed as others are ripped off, further producing fluctuations in the emission current. Typical protrusions are roughly cone-like. To approximate these, flat-topped cones were simulated on the surface of a rounded, large diameter tip. Though this is not a completely realistic depiction of a protrusion, it allowed for a relative comparison to be made between different protrusion geometries. The emission current was greater for both a taller and narrower protrusion, and the amount of current through the grounded anode compared to the emission current was lower, while for taller protrusions, it was higher.

The second electron gun type investigated was a thermionic electron gun. The thermionic electron gun consists of a pointed filament cathode, a Wehnelt cylinder and a grounded anode. Thermionic emission depends on the temperature of the cathode (Richard-Dushman equation) and the configuration of the Wehnelt cylinder (geometry and potential with respect to the cathode). As predicted, the emission current exponentially increases with temperature. In addition, the simulations showed that the emission current was linear with respect to the size of the emission region. The Wehnelt cylinder increases the current through the grounded anode by focusing the electron beam produced by the emitter.

The electron focusing column of the mini-SEM consists of several beam limiting apertures and an Einzel lens, followed by a scanning system. The investigation into the electron column included determining the effects on the electron beam probe (i.e., the electron beam spot at the sample), the working distance and the depth of focus by varying the focusing voltage, and physical sizes of the apertures in the electron column. The effects of spherical and chromatic aberration on the resulting electron beam probe were also determined. An interesting observation noted during the investigation of the electron focusing column prototype was that the electron probe current depended on the focusing voltage. Through simulations, it was determined that this effect was a result of vignetting occurring inside the electron focusing column.

The working distance and depth of focus are factors that determine the optimal location of the sample to be analyzed. The working distance (determined by the electric field produced the Einzel lens) is the distance between the last component of the electron column and the focal plane. The depth of focus is the depth of the sample that will be in

focus. The working distance was shown to be roughly linearly dependent on the diameter of the second Einzel. The thickness (length) of the second Einzel was also shown to affect the working distance, though for thicknesses greater than 2 mm, the working distance remained fairly constant. Both the depth of focus and working distance were shown to be dependent on the aperture diameters of the grounded apertures of the electron focusing column (the first and third Einzel and the limiting aperture) when the diameters were small (less than 100μm or less than 200μm depending on the location of the aperture). The depth of focus also increased with working distance (parabolically or linearly depending on the electron probe size). In addition, the depth of focus for equal desired probe diameters was shown to be greater for the thermionic electron gun than for the cold field emission, for this particular mini-SEM geometry.

Two primary characteristics which illustrate the mini-SEM performance are the electron beam probe current and diameter (i.e., the resolution at the sample). The electron probe current (current incident at the sample plane) is the emission current minus losses as the electron beam travels through the various apertures in the mini-SEM. For imaging and x-ray analysis, the probe current was set to be 1 nA. The electron gun that resulted in the most current at the sample plane was the thermionic electron gun, which resulted in approximately 50 nA for an accelerating voltage of -10 kV and focusing voltage of -5 kV. The cold field emission gun with the etched tip produced 9 nA at the sample plane for the same settings. The cold field emission gun with the blunted tip did not produce the minimum current standard. This was considered inconsequential since the blunted tip was merely used to test the cold field emission gun configuration and control system, and was not intended to be used for imaging.

Besides the electron probe current, the other significant result was the electron probe diameter (size of the spot of electron incident on the surface of the sample). This spot size depends on working distance, depth of focus, and aberrations of the electron gun and focusing column. The working distance and depth of focus depends on the electron beam divergence, the amount of optical power by the electron lens (focusing voltage) and the diameters of the apertures inside the electron focusing column. The achievable electron probe diameter for the cold field emission gun was, as expected, much smaller than for the thermionic electron gun; despite the much lower beam divergence because the thermionic emission gun has more aberrations contained in it.

The optimal values for the various parameters of the mini-SEM were determined (Table 3.5). These values are based on simulation results and on the geometric restrictions of the lunar mini-SEM mechanical design and the requirement that the current at the sample be no less than 1 nA (sufficient for imaging and x-ray analysis).

Table 8.1 Parameters for optimal imaging and analysis settings. These values are based on simulation results and on the geometric restrictions of the lunar mini-SEM mechanical design and the requirement that the current at the sample be no less than 1 nA (sufficient for imaging and x-ray analysis).

	ET CFEG	**TEG**
Accelerating Voltage (kV)	-10	-10
Cathode tip Diameter (μm)	0.7-0.9	0.1-0.15
Virtual Source Diameter (μm)	< 0.005	30-40
Temperature of Cathode (K)	300	3000
Minimum Emission Current (μA)	30-10	100
Typical Extraction or Bias Voltage (V)	3000-4000	5-8
Cathode to Extractor (ET CFEG) or to Wehnelt Cylinder (TEG) Distance (μm)	75-100	
Maximum Grounded Anode to Extractor or to Wehnelt Cylinder Distance (mm)	8-10	
Minimum Current through Grounded Anode (nA)	2-5	30
Aperture Diameter of Entrance Pupil (μm)	75-100	
Aperture Diameter of First Einzel (μm)	150-200	
Thickness of Second Einzel (mm)	2-4	
Diameter of Second Einzel (mm)	10-15	
Focusing Voltage (kV)	-5 or +12	-5 or +12
Aperture Diameter of Third Einzel (μm)	100-200	
Desired Working Distance (mm)	10-30	
Achievable Depth of Focus for 50 nm electron probe size (μm for CFEG, mm for TEG)	2-3	2-3
Predicted Current at Sample Plane (nA) (Electron probe current)	9	50
Maximum Electron probe size (nm)	50	

Future work in this area should include investigating the effects of misalignment and astigmatism in the mini-SEM, and determining potential trade-offs to adding a second lens to the focusing column to help reduce aberrations.

APPENDIX A

CHARGED PARTICLE OPTICS SOFTWARE

The software used in this thesis was Charged Particle Optics in Two Dimensions with Sources (CPO2DS) [1]. CPO2DS is a commercially available software from SIS. CPO2DS was chosen for a variety of reasons: CPO uses boundary element method to calculate the electric field and therefore is more accurate with a combination of rectangular and curvilinear boundaries. The lunar mini-SEM ideally has cylindrical symmetry which CPO2DS can handle exceptionally. CPO is one of a very few charged particle optics simulation software that accurately calculates the expected emission. CPO2DS uses Boundary Element method (BEM) to calculate electric field. BEM is superior to other methods in that it can accurately calculate electric fields from rectangular and curvilinear boundaries. The BEM uses a two step process to determine the electric field at a given point (Figure A.1). First it calculates the surface charge on a given electrode from the electric potential of that electrode set by the user (Equation A.1)[1]. Second, it determines the electric field (or electric potential) at a given point from this calculated surface charge (Equation A.2).

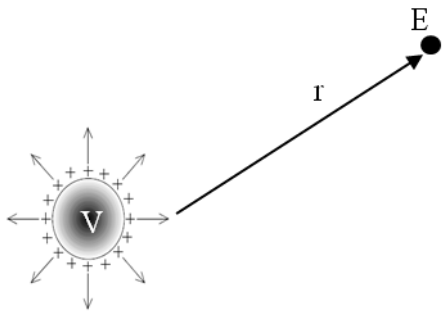

Figure A.1 The electric field at a given point distance, r, away from an electrode of potential V is calculated in CPO with the boundary element method [1, 2].

The surface charge, q, for a sphere of radius R and voltage V is given by (Figure A.1) [1, 2]

$$q = 4\pi\varepsilon_0 RV \qquad \text{Equation (A.1)}$$

The electric field, E, at a point r, distance away from charge, q, is given by [1, 2];

$$E(r) = \frac{q}{4\pi\varepsilon_0 r^2} \qquad \text{Equation (A.2)}$$

Finite Difference Method (FDM), a method used frequently in other charged particle optics simulation software, determines the electric field on a grid [1, 2]. A grid is placed on the system under investigation and the voltage is calculated from the voltages of the surrounding points. The FDM can become inaccurate if a curved boundary is placed on this rectangular grid [2]. The benefit of the BEM is that it is accurate for curved and rectangular boundaries because it does not calculate the electric field (or electric potential through the same method.

Another advantage of CPO over other charged particle optics simulation software is its accurate handling of sources [1]. CPO with sources uses the fundamental equations to determine the emission from a specific source. The different types of emission that the

CPO with sources handles are thermionic emission, cold field emission, and extended Schottky emission (more information in Section A.2.3, below).

For thermionic emission, the user defines either the temperature and the Richardson's constant of the cathode or defines a current density being emitted by the cathode. CPO uses the Richard-Dushman equation to calculate the emission current and Child's Law to calculate the path. For cold field emission the user defines the work function of the cathode. CPO uses the Fowler-Nordheim equation to calculate emission. Schottky emission uses a modified Richard-Dushman equation to calculate the emission current from the extended Schottky emitter. Also, there is an option for a user-defined cathode. It allows the user to define the emission properties of new and unconventional cathodes (such as a thermionic temperature that depends on position, or new forms of cold-field or Schottky emitters, such as insulators).

In CPO, a cathode can be defined with any shape or size. CPO breaks up the cathode into a user defined number of segments. These segments can be disturbed uniformly or with equal area, depending on the 'p' value indicated by user (more information in Section A.2.1, below). The emission current is emitted from the center of these cathode segments and is indicated by a ray (the path of the 'bundle' of electrons). These rays interact by space-charge effects, which can limit the current emitted from the cathode. The rays' paths are determined from the electric field at each point along its path.

In CPO2DS, the user can define a variety of symmetries (more information in Section A.2, below). The symmetries used in this thesis were those for cylindrical symmetry. To vacillate speed, for cylindrical symmetry, the software will calculate the

rays (paths of current) in one quadrant and rotate about the z-axis to determine the current in the other quadrants.

A.1 Quick Running of a .dat file in CPO2DS

1.) When CPO2DS is first opened, two windows are open the graphics window and the Information window (Figure A.2).

Figure A.2 Image of Graphics Window and Information Window in CPO 2DS [1].

Graphics window will show an image of the simulation during and after run. Information window will give output information of last run.

2.) File> ‘Open for running and databuilding’ (Figure A.3)

Figure A.3 Image of File drop down menu

3.) Choose .dat file for running (**Error! Reference source not found.**) (C:\cpo\2d)

4.) Choose to RUN or change configurations of Databuilder (Figure A.4).

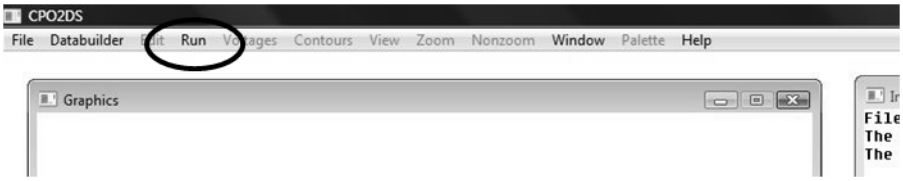

Figure A.4 Image of Menu Options after opening .dat file

To run push Run

To change configurations follow instructions below (Section A.2)

A.2 Changing configurations of Databuilder (i.e. the system)

1.) Select Databuilder on upper left (Figure A.5).

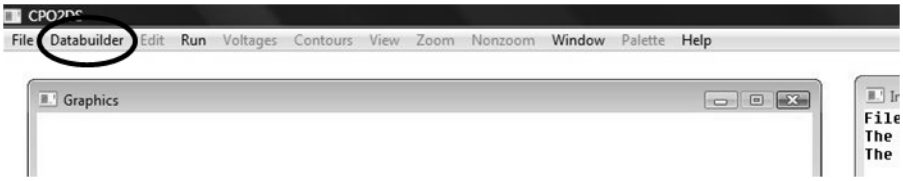

Figure A.5 Image of Menu Options after opening .dat file

2.) Choose item to be changed from drop down menu (Figure A.6 and Table A.1)

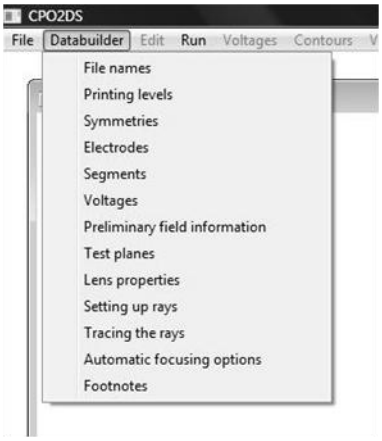

Figure A.6 Image of drop down menu for Databuilder.

Table A.1 List and description of Databuilder menu options.

Menu option	Description
File names	For changes in the name of the output file
Printing Levels	For choices in the amount of information listed
Symmetries	For changes in the symmetries of system
Electrodes	For changes in the size/ shape and location of electrodes in
Segments	For changes in the overall number of Segments
Voltages	For changes in the Voltages applied to the electrodes
Preliminary field information	For changes to the outputted potentials field information
Test planes	For changes in the location and placement of test planes
Lens properties	For choice to calculate lens properties of system. (For most applications and runs set to off.)
Setting up rays	For changes to emission and space charge options
Tracing the rays	For changes to ray limits, field view, and
Automatic focusing options	For choices of automatic focusing option
Footnotes	For information regarding the .dat file that is presently open

4.) Make adjustments where needed/desired.

Below are screen shots of the windows and more information when necessary for each of the Databuilder menu options.

Menu option ‘File names’ is used for changes in the name of the output file (Figure A.7).

Ray output file is copy of information in Information Window.

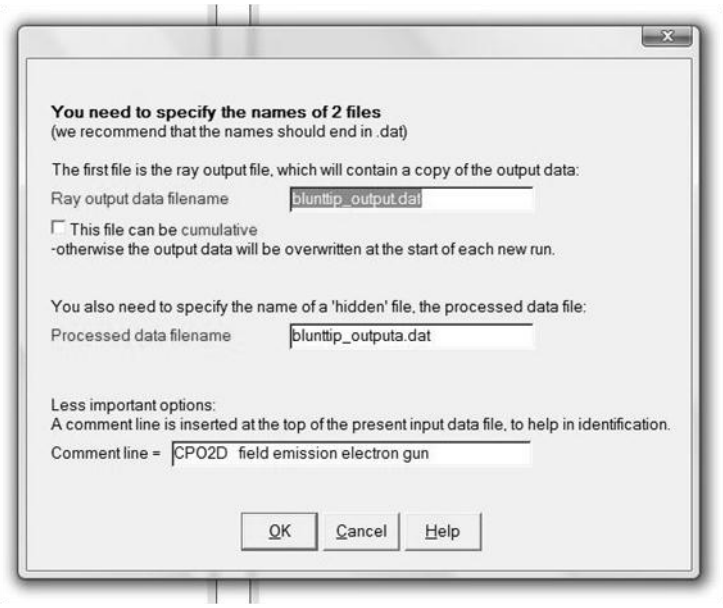

Figure A.7 Image of Filename window. Ray output file is the file with a copy of the Information Window.

Menu Option ‘Printing Levels’ is used to make choices in the amount of information listed (Figure A.8). Partial option is normally preferred.

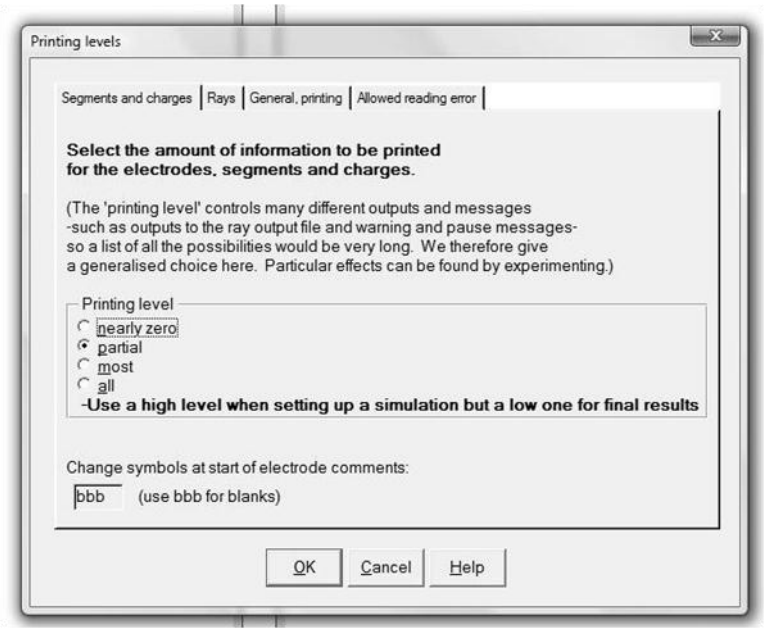

Figure A.8 Image of Printing Levels window

Menu Option Symmetries is used to make changes in the symmetries of system (Figure A.9). Cylindrical symmetry was chosen for lunar mini-SEM system.

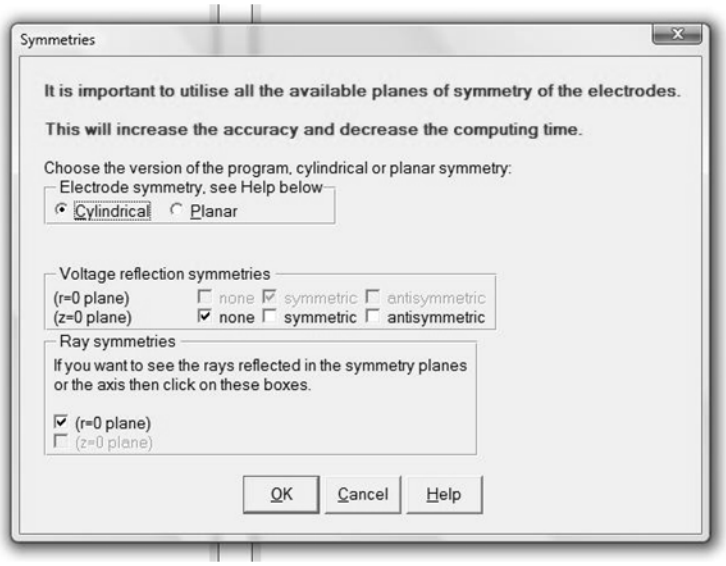

Figure A.9 Image of Symmetries Options window

Menu option ‘Electrodes’ is used to make changes in the size/ shape and location of electrodes in the system (Figure A.10). Adjustments to the overall electrodes and which electrode is being displayed are listed in Table A.2. The electrode is defined through the options listed in Table A.3. Figure A.11 shows the ‘Advanced options’ window. It controls the spacing of the subdivisions (segments).

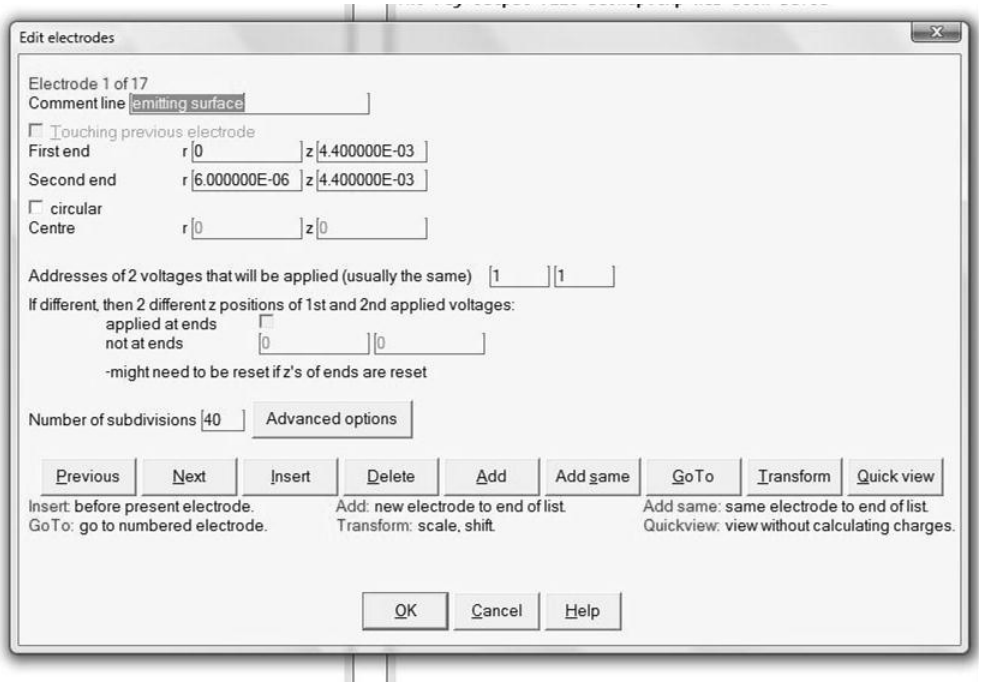

Figure A.10 Image of Edit Electrodes window. The electrode is defined by the two points (First/Second End). The Voltage Address chooses the voltage address (which has a voltage associated with it) defined previously.

Table A.2 Adjustments for the electrodes overall and changes to the electrode displayed

Adjustment	Description
Previous/Next	Changes the electrode whose information is being displayed
Transform	Changes the scale/location of the electrodes selected
Quick View	Displays the electrodes defined in the Graphics window
Go To	Changes the display to information of electrode selected

Table A.3 Definition of electrode is made through the following options.

Definition Option	Description
Comment line	Information on the electrode
First/Second End (r,z)	The electrode is defined through the definition of the two ends
Touching Previous	Allows the first end of the electrode to be defined by the second end of the previous electrode
Circular Centre	Allows the electrode to be circular in shape
Addresses of Voltages	Picks the voltage address the electrode is at (normally both ends at same address).
Number of Subdivisions	Identifies the number of segments of the electrode (Large segments cannot be close to very small segments)
Advance option	adjusts the 'p' value which adjusts the spacing of the segments in the electrode (p=1 => evenly spaced, p=0.5 => equal area of the segments)

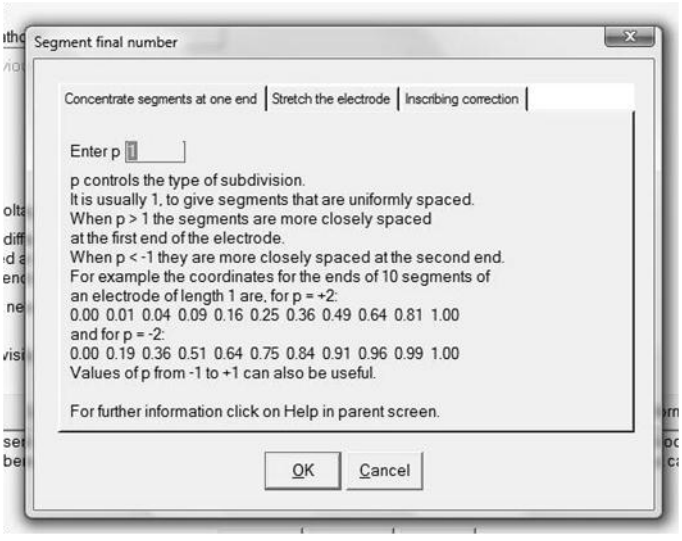

Figure A.11 Advance options window. 'p' adjusts the spacing of the segments that make up the electrode.

Menu option ‘Segments’ is used to make changes in the overall segments of the system (Figure A.12). Input zero to get automatic number of segments.

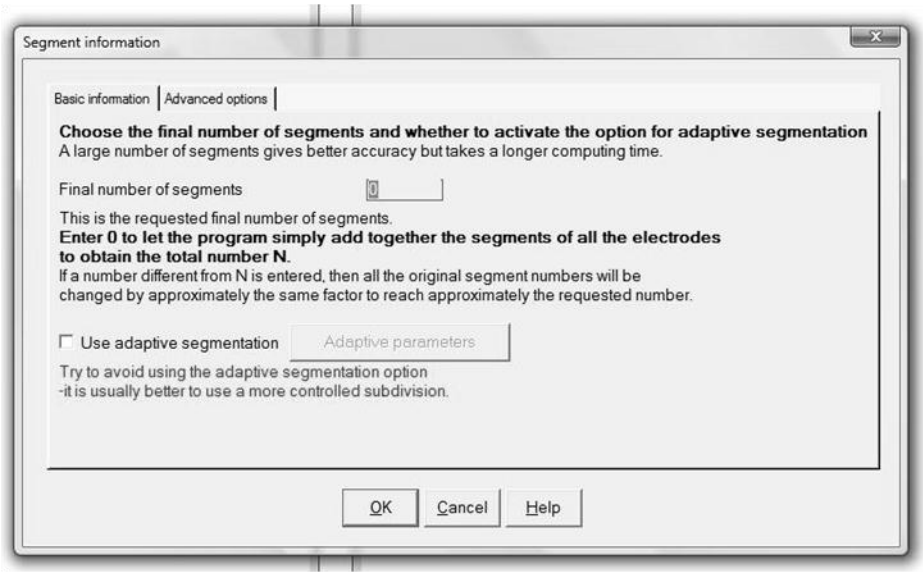

Figure A.12 Image of Segments window

Menu option ‘Voltages’ is used to make changes in the Voltages applied to the electrodes (Figure A.13). Voltage addresses (1-3 for the electron guns) are referenced by the electrode.

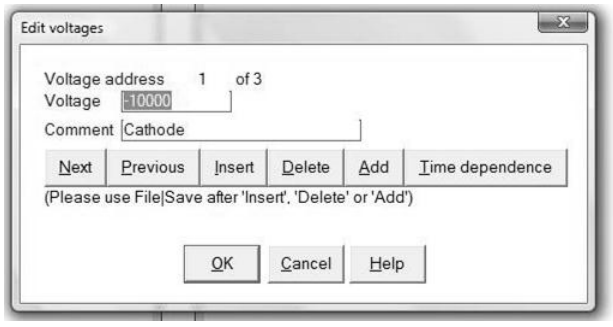

Figure A.13 Image of Edit Voltages window

Menu option ‘Preliminary field information’ is used to make changes to the outputted potentials and field information (Figure A.14).

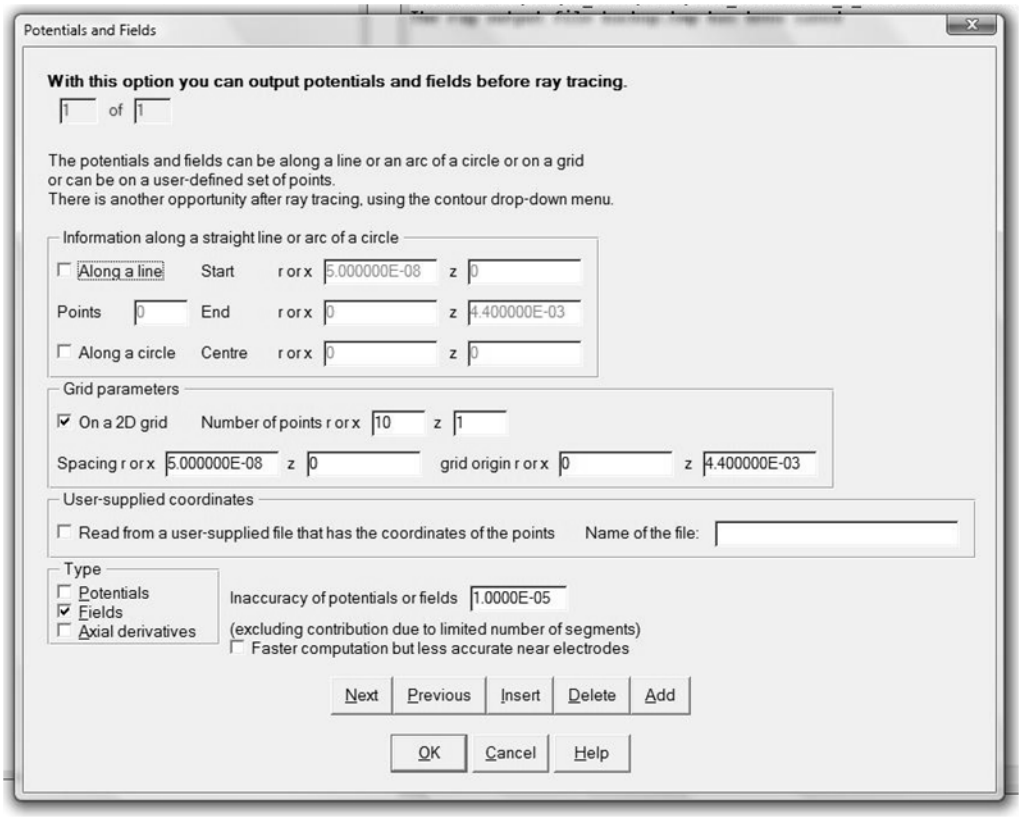

Figure A.14 Image of Preliminary Potentials and Fields

Menu option ‘Test planes’ is used to make changes in the location and placement of test planes (Figure A.15). Two test planes are required when using cathodes.

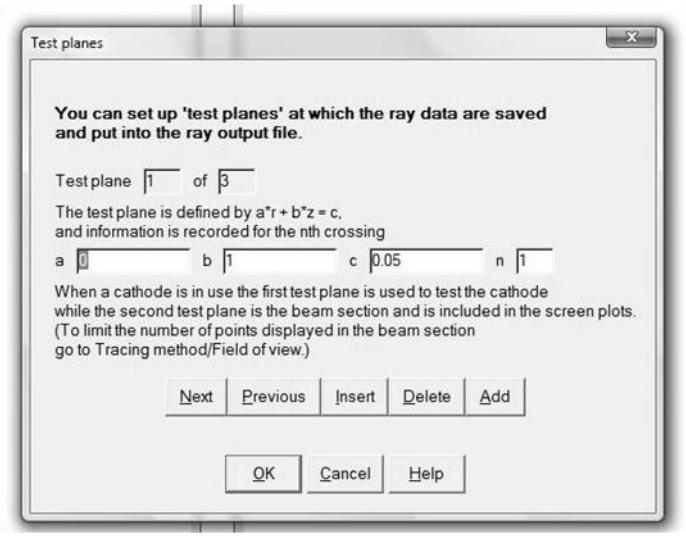

Figure A.15 Image of edit test planes window

Menu option ‘Setting up rays’ is used for changes to emission and space charge options (Figure A.16). Choose type of particle and type of emission. This will be discussed in further detail in the setting up emission section (Section A.2.1).

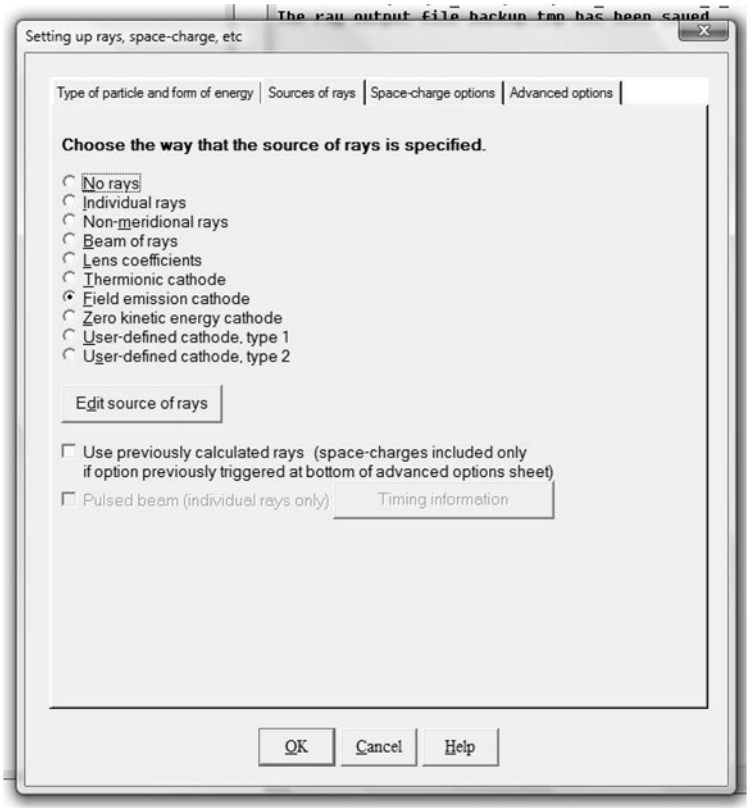

Figure A.16 Image of Sources window. Choose type of particle and type of emission and define the parameters of that emission.

Menu option ‘Tracing the rays’ is used for changes to method of tracing, ray limits and field of view (Figure A.17 and Figure A.18). Ray limits describe when the program will stop tracing the ray. Field of view limits describe the limits on the displayed system in the Graphics Window.

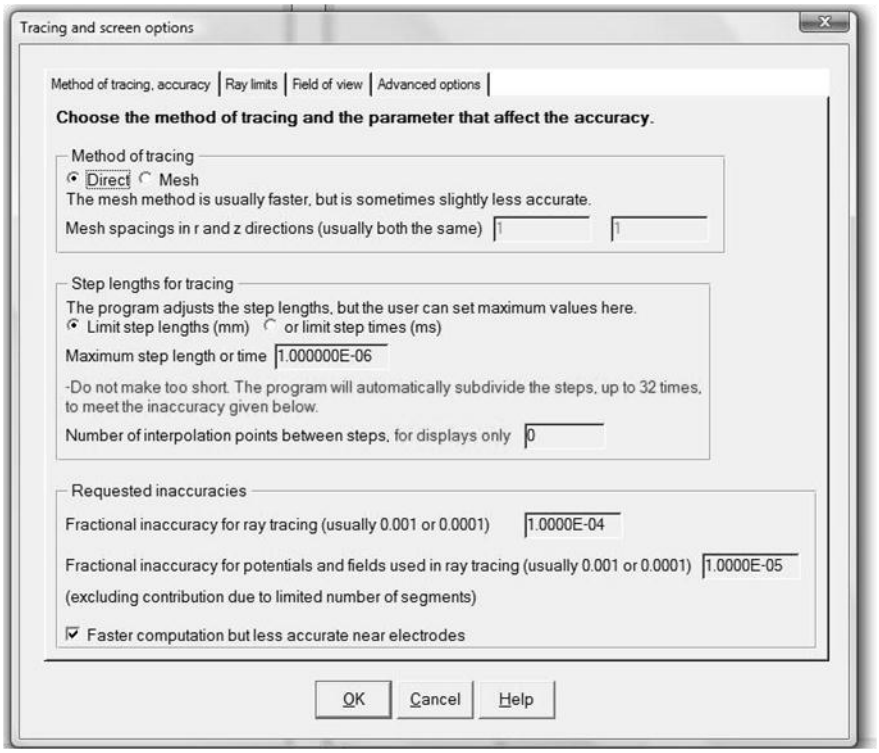

Figure A.17 Image of Ray Tracing options. Mesh ray tracing is faster, but less accurate. Step lengths determine the distance the ray trace will travel before recalculating.

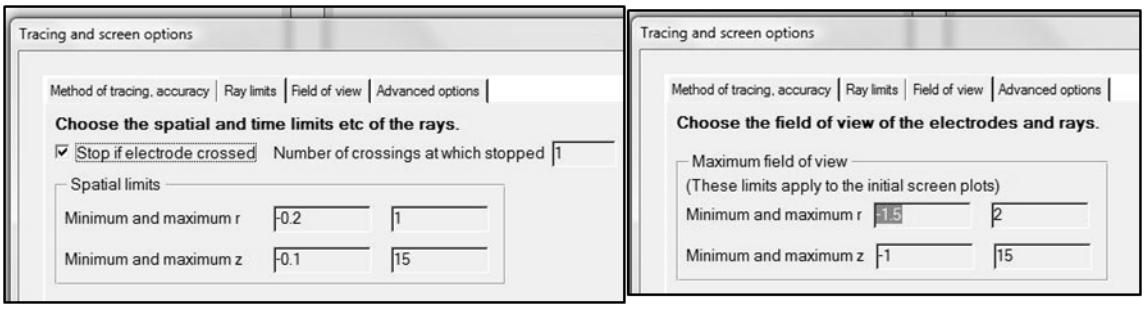

Figure A.18 Image of More Ray tracing options. Ray limits define when the ray (beam of electrons is stopped. Field of view defines the area that is seen in the Graphics Window.

Menu option 'Automatic focusing options' is used to make changes in the choices of automatic focusing option (Figure A.19).

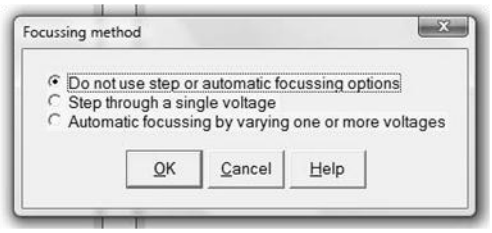

Figure A.19 Image of Lens properties window.

A.2.1 Defining a source in CPO 2DS

1.) Select 'Setting up Rays' in drop down DataBuilder Menu (Figure A.20)

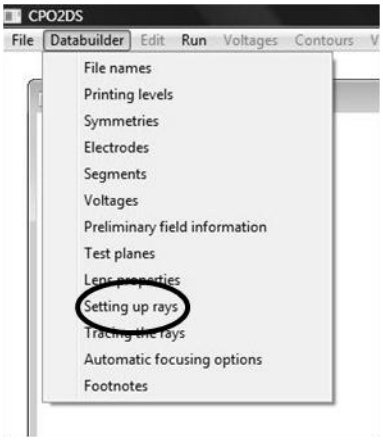

Figure A.20 'Setting up Rays' in Databuilder menu.

2.) Select type of particle and form of initial energy (Figure A.21) (electrons and Kinetic for the lunar mini-SEM)

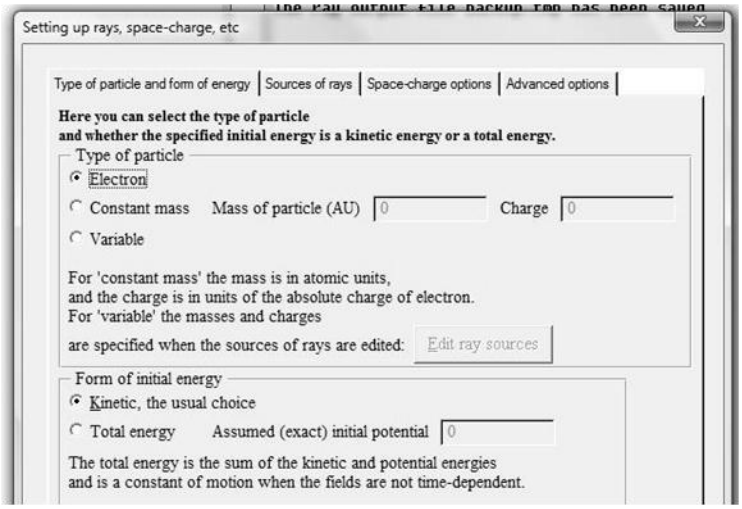

Figure A.21 Sources Options window. Select type of particle and form of initial energy.

3.) On 'Source of rays' tab (Figure A.22 and Table A.4), choose Source desired

Figure A.22 Image of 'Sources of Rays' Tab in setting sources Databuilder menu option.

Table A.4 Type of sources in CPO2DS with descriptions on each.

Type of Source	Description
No Rays	for no source, just the electrode diagram
Individual Rays	to define specific individual rays
Non-meridian Rays	
Beam of Rays	to define a bundle of rays to trace
Lens coefficient	for calculation of aberrations and lens characteristics
Thermionic cathode	for a thermionic electron gun
Field emission cathode	for a cold field emission electron gun
Zero kinetic energy cathode	
User-defined cathode type 1/ 2	for user defined special characteristic cathodes

5.) Press 'Edit source of rays' button to display options for emission

6.) Input desired options (Instructions for options for a few sources listed below)

7.) Press 'Okay' to return to Graphics and Information Windows.

Options window for thermionic emission (Figure A.23)

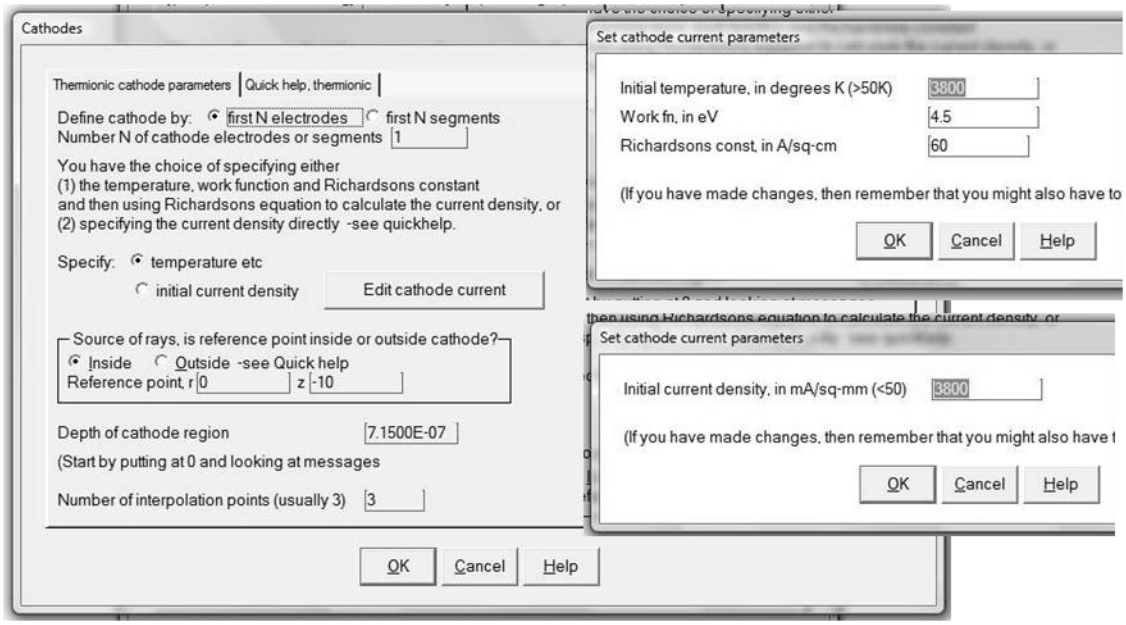

Figure A.23 Options for Thermionic emission Reference point is to determine the direction of the path of the rays. Specify ‘Temperature’ or ‘Initial current density’. Richardson’s constant units should be A/sq-cm/sq-K.

1.) Select which to define cathode by ‘First N electrodes’ or ‘First N segments’.

This allows user to define unique geometries for the emission region.

2.) Input N

3.) Specify ‘Temperature’ or ‘Initial current density’

4.) Select 'Edit cathode current'

5.) If Specify Temperature,

a.) Input Initial Temperature in Kelvin

b.) Input work function in eV (4.5eV for tungsten)

c.) Input Richardson's constant in A/sq-cm/sq-K (60 for tungsten)

Note: The display has 'A/sq-cm'. This is incorrect.

The program calculates it as if it is A/sq-cm/sq-K

6.) If Specify Initial current density

a.) Input initial current density

7.) Input Reference point inside/outside the cathode. This defines which direction the current is expected to travel.

Options window for cold field emission is shown in Figure A.24.

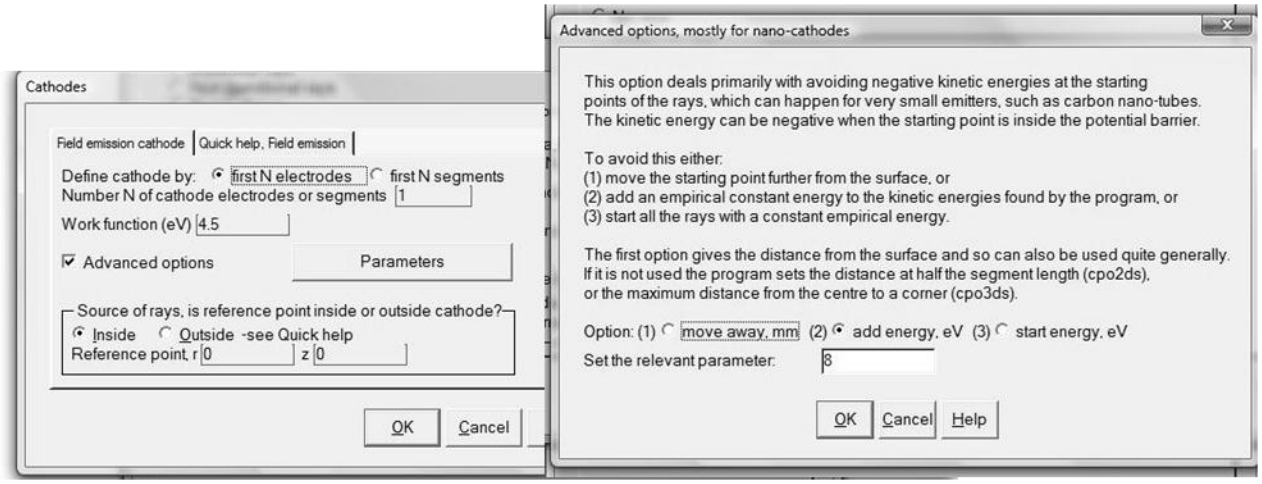

Figure A.24 Options for cold field emission N assists user in defining the emission region. Advanced options assist the electrons in being emitted.

1.) Select which to define cathode by ‘First N electrodes’ or ‘First N segments’.

This allows user to define unique geometries for the emission region)

2.) Input N (For shaped ET, N=1 and for a BT with m protrusions, N=2m-1)

3.) Input Work function (4.5eV for tungsten)

4.) Input Reference point inside/outside the cathode. This defines which direction the current is expected to travel.

5.) Advanced Options are used to assist the electrons in being emitted

Options window for 'Single Rays' is shown in Figure A.25.

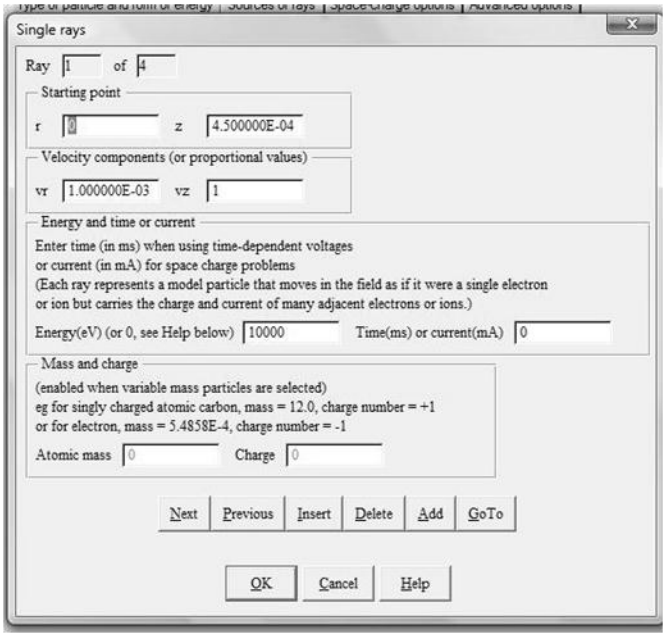

Figure A.25 Options window for Single Rays. Defining starting point (r,z), velocity components (vr, vz), energy, and time/current to establish initial conditions of ray.

1.) To define single ray, push Add

2.) Define starting point

3.) Define velocity components

4.) Define Energy and Time/current

5.) To define another ray, follow steps 1-4 again**.**

A.3 Post Run Analysis in CPO 2DS

Results from the run are listed in the Information Window and in File output file labeled (Figure A.7) (C:\cpo\file name). This file can be opened using excel. (Delimited by space). At end of run Menus increase in choices (Figure A.26 and Table A.5).

Figure A.26 Menu Selections after run.

Table A.5 Menu Selections and descriptions in CPO2DS after run.

Menu Selection	Description
Contours	form contours/colour/grid(/Vector for E-field only) for Electric Field, Potentials or Space Charge (more information below)
View	Select objects to be displayed in graphics window (more information below)
Zoom	Adjusts zoom of graphics display With aspect ratio 1 to 1 (Right click to zoom in; Left click to turn off) (With selected aspect ratio does not work)
Non-zoom	Sets the graphics window to see the whole system set up by electrodes
Window	Adjusts windows displayed
Palette	Adjusts colors of the rays/segments

A.3.1 Contour

Contours allows the user to form contours/color/grid(/vector) for electric field, electric potential, and space charge (Figure A.27).

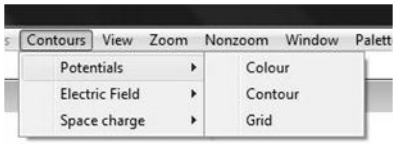

Figure A.27 Contour drop down menu. Contour allows the user to form contours/color/grid(/vector) for electric field, electric potential, and space charge

1.) Select contour/colour/grid (/vector) as desired

2.) Adjust Max and Min Values and contouring parameters as needed (Figure A.28). The displayed values are the software generated values. User can leave these values as is or change values. (For contours: Input number of contours as well.)

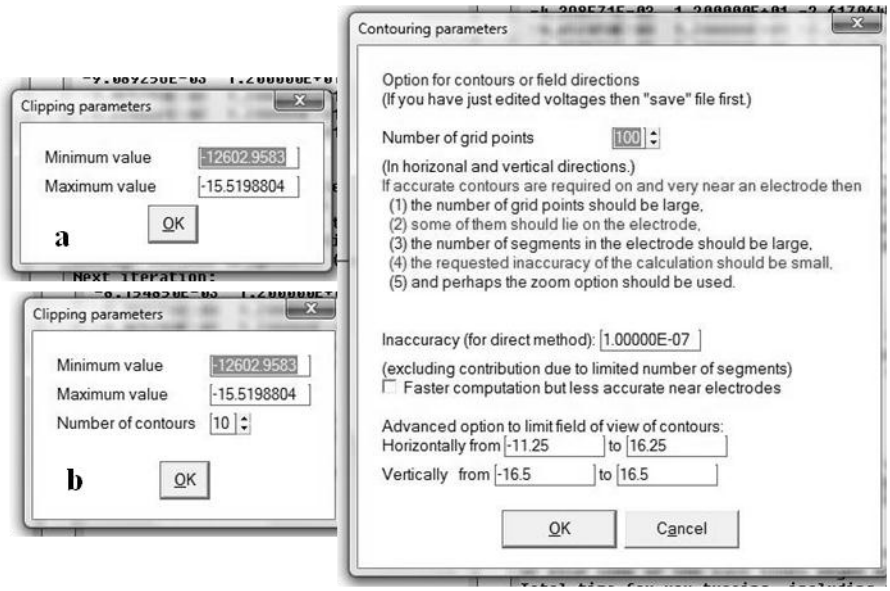

Figure A.28 Clipping and Contouring Parameters window. Adjust Max and Min Values and contouring parameters as needed. The displayed values are the software generated values. User can leave these values as is or change values. (For contours (b): Input number of contours as well.)

3.) Press okay and software will calculate and display results. (Shown in Figure A.29 are results from contour for the thermionic electron gun.)

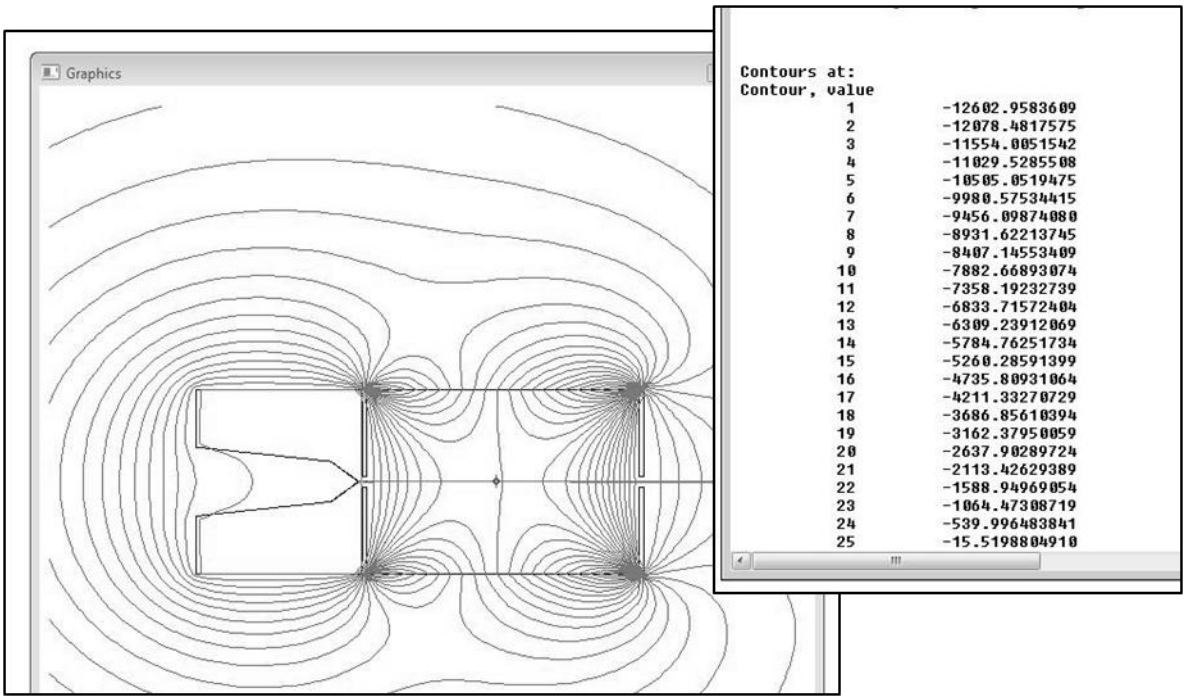

Figure A.29 Results of contour for Thermionic electron gun

A.3.2 View

The menu options in View adjust the displayed electron system in the Graphics Window (Figure A.30 and Figure A.31).

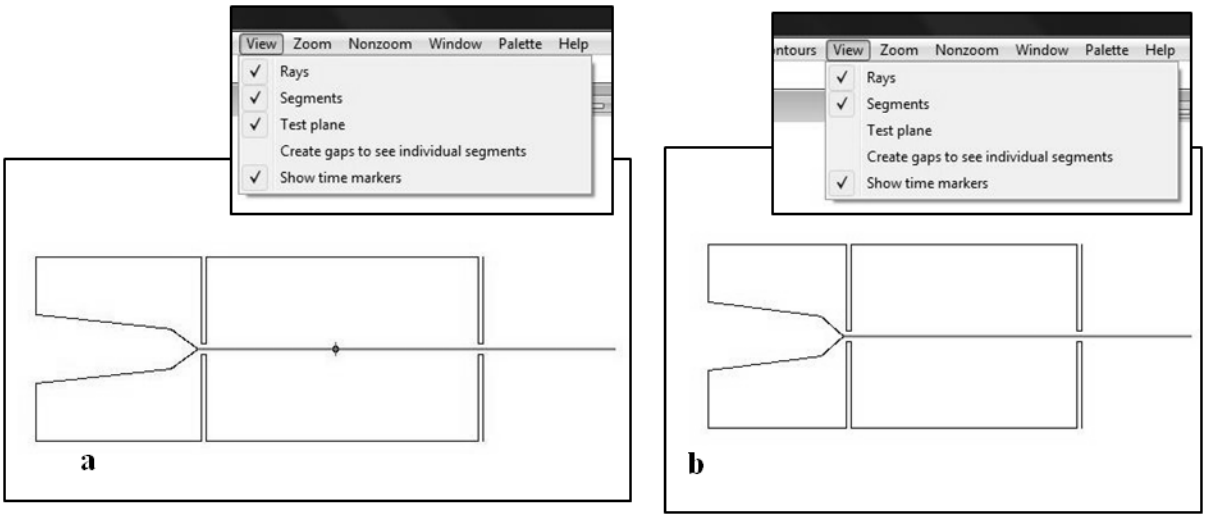

Figure A.30 View menu with resulting image in Graphics Window. (Thermionic electron gun). With (a) and without (b) test plane.

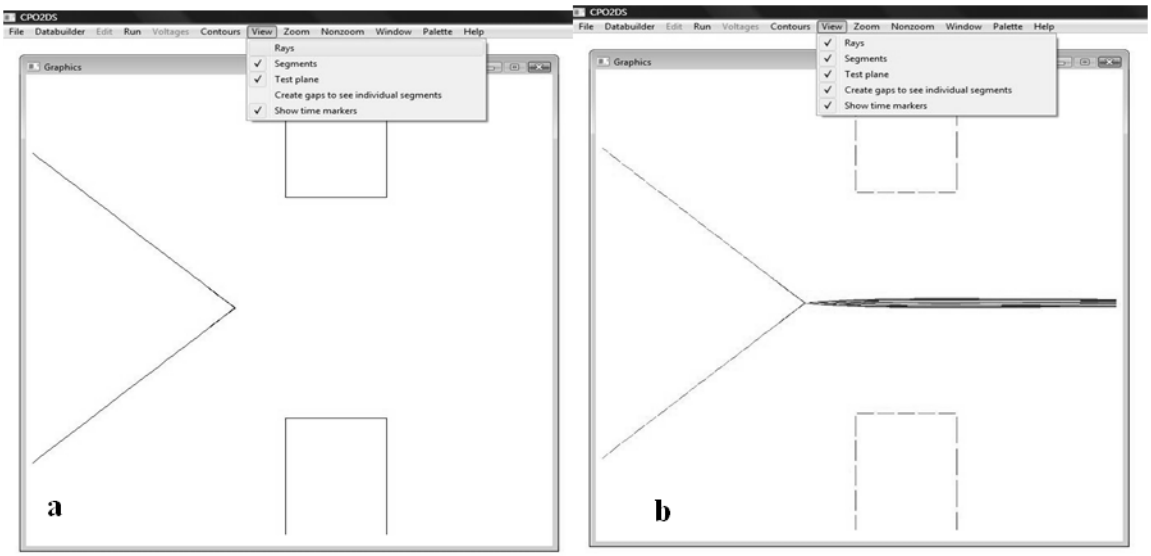

Figure A.31 Zoomed in View of the cathode (for thermionic electron guns) without rays (a) and with gaps to see individual segments.

A.4 Calculating Aberrations in CPO 2DS

1.) Identify the location of Gaussian image plane (z0)

a.) Place test plane at r=0 (using steps outlined in Section A.2)

b.) Trace series of rays at different vr (using steps outlined in Section A.2.1)

Table A.6 Initial conditions for use in individual ray to determine the image plane. 'zi ‘is the initial location (emission region if determing the aberrations for a electron gun.)

Initial condition	Ray 1	Ray 1	Ray 3
r	0	0	0
z	zi	zi	zi
vr	1	1	1
vz	0.001	0.002	0.003
Energy	KEi	KEi	KEi

c.) Locate where the rays cross the optical axis, zc. This will be in information window as well as in the output data file.

d.) plot zc vs vr^2

e.) extrapolate to z0 for vr=0 (z0 is the location of the Gaussian image plane.

2.) Calculate Coefficients

a.) Place test plane at z=z0 (using steps outlined in Section A.2)

b.) Calculate magnification, M,

i.) Set up rays using 'Lens Coefficient' source (using steps outlined in Section A.2.1)

ii.) Edit source of rays using settings listed in Table A.7

Table A.7 Settings in 'edit source of rays' to calculate magnification, M, in CPO2DS.

	Initial	Step length	Choice of coefficient
r	0	Δr	1
z	zi	0	0
vr	0	0	0
vz	0.001	0.001	0
KE	KEi	0.05*KEi	0

Output will be in the form shown in Figure A.32 and Table A.8.

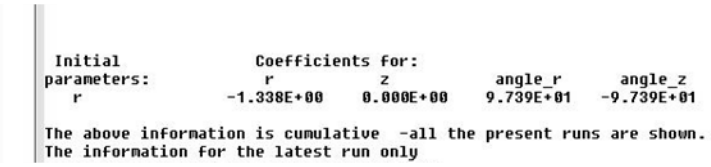

```
 Initial              Coefficients for:
parameters:            r           z          angle_r      angle_z
   r               -1.338E+00    0.000E+00    9.739E+01   -9.739E+01

The above information is cumulative  -all the present runs are shown.
The information for the latest run only
```

Figure A.32 Typical results for determining magnification, M.

Table A.8 Output information for determining magnification, M, in CPO2DS.

Initial parameters	Coefficients for:			
	r	z	angle_r	angle_z
r	M	0.00	#	#

Note: If output results in z not equal to zero, make minute adjustments to the location of test plane until z=0.

c.) Calculate spherical aberration coefficient, Cs,

i.) Set up rays using 'Lens Coefficient' source (using steps outlined in Section A.2.1)

ii.) Edit source of rays using settings listed in Table A.9.

Table A.9 Settings in 'edit source of rays' to calculate spherical aberration coefficient, Cs, in CPO2DS.

	Initial	Step length	Choice of coefficient
r	0	Δr	0
z	zi	0	0
vr	0	0	0
vz	0.001	0.001	3
KE	KEi	0.05*KEi	0

Output for calculating spherical aberration coefficient, Cs, will be in the form shown in Table A.10.

Table A.10 Output information for determining spherical aberration, Cs, in CPO2DS.

Initial parameters	Coefficients for:			
	r	z	angle_r	angle_z
a_z a_z a_z	Cs*M	#	#	#

iii.) From this calculate, spherical aberration using Equation (A.3). The resulting spherical aberration coefficient will be in units of millimeters.

$$Cs=Cs*M/M \qquad \text{Equation (A.3)}$$

d.) Calculate chromatic aberration, Cc,

i.) Set up rays using 'Lens Coefficient' source (using steps outlined in Section A.2.1)

ii.) Edit source of rays using settings listed in Table A.11.

Table A.11 Settings in 'edit source of rays' to calculate chromatic aberration coefficient, Cc, in CPO2DS.

	Initial	Step length	Choice of coefficient
r	0	Δr	0
z	zi	0	0
vr	0.001	0	0
vz	0.001	0.001	0
KE	KEi	0.05*KEi	1

Output for calculating chromatic aberration coefficient, Cc, will be in the form shown in Table A.12.

Table A.12 Output information for determining chromatic aberration, Cc, in CPO2DS.

Initial parameters	Coefficients for:			
	r	z	angle_r	angle_z
en	C(r,en)	#	#	#

iii.) From this calculate, chromatic aberration using Equation (A.4). The resulting chromatic aberration coefficient will be in units of millimeters.

$$Cc = \frac{C(r,en)*KEi}{M*vri}$$ Equation (A.4)

3.) Trouble shooting while calculating aberrations.

a.) If the rays do not make it through the system, the values chosen when setting up the rays were too *high*

Adjust the Δr or the vr

b.) If the output values give all zeroes, the values chosen when setting up the rays are too *small*

Adjust the Δr or the vr

REFERENCES

Chapter I

1. Gaskin J. (2010) *Earth and Space 2010 Conf. Proc,.* Symposium 4: Exploration and Utilization of Extraterrestrial Bodies, pg. 1246.

2. Gaskin J. et al., (2009) *LPSC XL Proc*., #2318.

3. Goldstein, J. et al., (2003) *Scanning Electron Microscopy and X-Ray Microanalysis*, New York: Springer Science and Business Media, LLC.

4. Orloff J., Ed., (1997) *Handbook of Charged Particle Optics,* CRC Press, New York.

5. Hawkes P. W. and Kasper E. (1989) *Principles of Electron Optics*. Vols. 1 & 2, Academic Press, London, England.

6. EBSciences Web site http://www.ebsstore.com

7. Manura D. (2008) *CPO, Charged Particle Optics program,* computer software, Manchester, UK, CPO Ltd.

8. Fujita, S. and Shimoyama, H. (2005) Journal of Electron Microscopy **54**(5), 413.

Chapter II

1. Butler, T. W. (1966) *6th Intern. Cong. Electron Microsc. (Kyoto)* 1, 193.

2. Goldstein, J. et al., (2003) *Scanning Electron Microscopy and X-Ray Microanalysis*, New York: Springer Science and Business Media, LLC.

3. Orloff J., Ed., (1997) *Handbook of Charged Particle Optics,* CRC Press, New York.

4. Hawkes P. W. and Kasper E. (1989) *Principles of Electron Optics*. Vols. 1 & 2, Academic Press, London, England

5. Fursey, G.N. (2003) *Applied Surface Science* **215**, 113.

6. Gaskin J. et al., (2009) *LPSC XL Proc*., #2318.

7. Tsunwaki, Y. et. al. (1999) *Nuclear Instruments and Methods in Physics Research A* **429**, 299.

8. Wiesner, J.C. and Everhart, T.E (1973) *J. Appl. Phys.* **44**(5), 2140.

9. Smith, R. et. al. (2005) *Applied Physics Letters* **87**, 013111.

10. Forbes, R. G. (1999) *J. Vac. Sci. Technol.* **B 17(2)**, 534.

11. Williams, D.B. and Carter, C. B. (2009) *Transmission Electron Microscopy: A Textbook for Materials Science*, Springer, New York, New York.

12. Yeong, K. S. and Thong, J. T. L. (2006) *J. of Appl. Phys.* **99,** 104903.

13. Tuggle, D. W. et. al. (1985) *J. of Micro.* **140**, 293.

14. Gaskin J. (2010) *Earth and Space 2010 Conf. Proc,.* Symposium 4: Exploration and Utilization of Extraterrestrial Bodies, 1246.

15. Manura D. (2008) *CPO, Charged Particle Optics program,* computer software, Manchester, UK, CPO Ltd.

16. Crewe, A. V., et al, (1968) *Review of Scientific Instruments* **39**, 576.

17. Murphy, E.L. and Good, R.H., Jr. (1956) *Physical Review* 102, 6.

18. EBSciences Web site http://www.ebsstore.com

Chapter III

1. Tuggle, D. W. et al. (1985) *J. of Micro.* **140**, 293.

2. Manura D. (2008) *CPO, Charged Particle Optics program,* computer software, Manchester, UK, CPO Ltd.

3. Chang, T. H. P. et al. (1991) *IEE Transaction on Electron Devices*. **38** (10), 2284.

4. Kim, H. S. et al. (2003) *J. of Korean Physical Society*. **43**(5), 831.

5. Goldstein, J. et al., (2003) *Scanning Electron Microscopy and X-Ray Microanalysis*, New York: Springer Science and Business Media, LLC.

6. Hawkes P. W. and Kasper E. (1989) *Principles of Electron Optics*. Vols. 1 & 2, Academic Press, London, England.

7. Orloff J., Ed., (1997) *Handbook of Charged Particle Optics,* CRC Press, New York

8. Knauer, W. (1981) *Optik* **59**, 335

9. Smith, R. et al. (2005) *Applied Physics Letters* **87**, 013111.

10. Forbes, R. G. (1999) *J. Vac. Sci. Technol.* **B 17(2)**, 534

11. Williams, D.B. and Carter, C. B. (2009) *Transmission Electron Microscopy: A Textbook for Materials Science*, Springer, New York, New York.

Chapter IV

1. Gaskin J. (2010) *Earth and Space 2010 Conf. Proc,*. Symposium 4: Exploration and Utilization of Extraterrestrial Bodies, 1246.

2. Manura D. (2008) *CPO, Charged Particle Optics program,* computer software, Manchester, UK, CPO Ltd.

3. Goldstein, J. et al., (2003) *Scanning Electron Microscopy and X-Ray Microanalysis*, New York: Springer Science and Business Media, LLC.

4. Hawkes P. W. and Kasper E. (1989) *Principles of Electron Optics*. Vols. 1 & 2, Academic Press, London, England.

5. Orloff J., Ed., (1997) *Handbook of Charged Particle Optics,* CRC Press, New York

6. Smith, R. et al. (2005) *Applied Physics Letters* **87**, 013111.

7. Forbes, R. G. (1999) *J. Vac. Sci. Technol.* **B 17(2)**, 534

Chapter V

1. Hawkes P. W. and Kasper E. (1989) *Principles of Electron Optics*. Vols. 1 & 2, Academic Press, London, England

2. EBSciences Web site http://www.ebsstore.com

3. D.B. Williams, and C.B. Carter (2009) *Transmission electron microscopy: a textbook for material science. Imaging Part 3*, Springer: New York.

4. Manura D. (2008) *CPO, Charged Particle Optics program,* computer software, Manchester, UK, CPO Ltd.

5. Read, F. H. and Bowring N. J. (2004) *Nuclear Instruments and Methods in Physics Research* A 531, 407.

6. Murphy, E.L. and Good, R.H., Jr. (1956) *Physical Review* 102, 6.

7. Egerton, R. (2005) *Physical Principles of Electron Microscopy*. Springer: New York.

Chapter VI

1. Hawkes P. W. and Kasper E. (1989) *Principles of Electron Optics*. Vols. 1 & 2, Academic Press, London, England.

2. Manura D. (2008) *CPO, Charged Particle Optics program,* computer software, Manchester, UK, CPO Ltd.

3. Goldstein, J. et al., (2003) *Scanning Electron Microscopy and X-Ray Microanalysis*, New York: Springer Science and Business Media, LLC.

4. Mourlis, P. and Macdonald, J. (1997) *Geometrical Optics and Optical Design*, New York: Oxford University Press, Inc.

Chapter VII

1. Hawkes P. W. and Kasper E. (1989) *Principles of Electron Optics*. Vols. 1 & 2, Academic Press, London, England.

2. Manura D. (2008) *CPO, Charged Particle Optics program,* computer software, Manchester, UK, CPO Ltd.

3. Gaskin J. (2010) *Earth and Space 2010 Conf. Proc,*. Symposium 4: Exploration and Utilization of Extraterrestrial Bodies, pg. 1246.

4. Gaskin J. et al., (2009) *LPSC XL Proc*., #2318.

Appendix A

1. Manura D. (2008) *CPO, Charged Particle Optics program,* computer software, Manchester, UK, CPO Ltd.

2. Hawkes P. W. and Kasper E. (1989) *Principles of Electron Optics*. Vols. 1 & 2, Academic Press, London, England